UNIVERSIDAD DE CHILE
FACULTAD DE CIENCIAS FÍSICAS Y MATEMÁTICAS
DEPARTAMENTO DE GEOLOGÍA

GEOQUÍMICA DE ELEMENTOS TRAZA EN MAGNETITA DEL DEPÓSITO DE HIERRO-APATITO CERRO NEGRO NORTE, CHILE

TESIS PARA OPTAR AL GRADO DE MAGÍSTER EN CIENCIAS, MENCIÓN GEOLOGÍA

EDUARDO ANDRÉS SALAZAR ARIAS

PROFESOR GUÍA
FERNANDO BARRA PANTOJA

MIEMBROS DE LA COMISIÓN
MARTIN REICH MORALES
GLORIA ARANCIBIA HERNÁNDEZ

Este trabajo ha sido financiado por el proyecto FONDECYT 1140780 y Núcleo Milenio Trazadores de Metales NC130065

SANTIAGO DE CHILE
2018

RESUMEN DE LA TESIS PARA OPTAR AL GRADO
DE: Magíster en Ciencias Mención Geología
POR: Eduardo Andrés Salazar Arias
FECHA: Agosto de 2018
PROFESOR GUÍA: Fernando Barra Pantoja
PROFESOR CO-GUÍA: Martin Reich Morales

GEOQUÍMICA DE ELEMENTOS TRAZA EN MAGNETITA DEL DEPÓSITO DE HIERRO-APATITO CERRO NEGRO NORTE, CHILE

Los depósitos de hierro-apatito, o tipo Kiruna, constituyen la principal fuente de hierro del país; sin embargo, aún no existe concenso en relación a su génesis. Diferentes modelos han sido propuestos para explicar el origen de estos depósitos con hipótesis que van desde un origen netamente mágmatico por inmiscibilidad líquida, o una génesis por reemplazo hidrotermal de rocas pre-existentes. Recientemente, se ha planteado un nuevo modelo (modelo de flotación) que considera la formación inicial de cristales de magnetita en un magma de composición intermedia que luego ascienden y crecen debido a la interacción con fluidos exsueltos del magma. El presente trabajo se centra en el yacimiento de hierro-apatito Cerro Negro Norte, ubicado en la Región de Atacama, en el extremo norte de la Franja Ferrífera de la Cordillera de la Costa, y tiene por finalidad identificar los procesos involucrados en su formación y constreñir la temporalidad de ésta.

La mineralización de hierro está conformada por cuerpos subverticales de magnetita maciza con intercrecimiento de actinolita emplazados en rocas volcánicas de la Formación Bandurrias de edad Jurásico Superior-Cretácico Inferior. Estudios recientes muestran que la geoquímica de elementos traza contenidos en la mena de magnetita constituyen una herramienta importante para identificar los procesos geológicos responsables de la formación de la mineralización. En este trabajo se presentan los primeros resultados de concentración de elementos traza en magnetita realizados en Chile, los cuales fueron obtenidos mediante la técnica analítica de ablación por láser acoplado a un espectrómetro de masas de inducción de plasma (LA-ICP-MS).

En Cerro Negro Norte se reconocen cuatro tipos texturales de magnetita: Tipo I, representada por núcleos de magnetita de alta temperatura con inclusiones de anfíbol, piroxeno y, en menor medida, óxidos de Fe-Ti; Tipo II, una magnetita libre de inclusiones, generalmente rodeando núcleos de Tipo I; Tipo III, magnetita con una zonación química sin inclusiones; y, Tipo IV, magnetita en vetillas con arreglos de inclusiones sinuosas. Los cristales de magnetita presentan contenidos variables de elementos traza, en particular el V varía de 2269 (Tipo I) a 7.98 ppm (Tipo IV), mientras que el Ga fluctúa entre 59.7 (Tipo I) a 11.63 ppm (Tipo IV). Basado en la interpretación de los análisis químicos de magnetitas realizados, se propone un nuevo diagrama basado en las concentraciones de V y Ga para discriminar entre magnetita de origen magmático e hidrotermal.

Adicionalmente, y como complemento al estudio geoquímico de magnetitias se realizó la datación radiométrica del intrusivo dioritico responsable de la mineralización de hierro. Este fue datado mediante el método de U-Pb en circones, obteniéndose una edad de 130.05 ± 0.72 Ma, acotando la formación del depósito al Cretácico temprano.

Las variaciones texturales y químicas entre las magnetita Tipo I y II pueden explicarse por una transición desde condiciones netamente magmáticas a condiciones magmáticas-hidrotermales en donde predominan procesos de disolución-reprecipitación causadas por fluidos de alta temperatura. El ascenso de cristales de magnetita Tipo I y II se promovería mediante la nucleación y coalescencia de burbujas en la superficie de los microlitos de magnetita por parte de fluidos hidrotermales de origen magmático. Las magnetitas tipo III y IV apoyan la noción de una remobilización por dilución y posterior reprecipitación. Los datos obtenidos en esta tesis son consistentes con un modelo de flotación para la formación del depósito de Cerro Negro Norte.

De joven fuiste un capullo
que de viejo al fin se abrió
con ternura que brotó,
tu mirada, cuan arrullo.

AGRADECIMIENTOS

Agradezco en primer lugar a los miembros de la comisión del presente trabajo de tesis, Dr. Fernando Barra, Dr. Martin Reich y a la Dra. Gloria Arancibia. En especial quisiera agradecer al Dr. Fernando Barra por continuar guiándome por más de 7 años en el rudo camino de la ciencia y no deshacerse de mí; gracias por darme la confianza, apoyo y, además, la libertad de hacer, tanto en mi trabajo como en actividades afines. Mención especial también al Dr. Martin Reich por tener la infinita disposición a discutir y colaborar con cada problema y/o idea loca que cruzaba por mi cabeza. A ellos les sigo agradeciendo por enseñarme a no construir un gigante con pies de barro hasta el último minuto de mi formación.

También agradezco a la empresa CAP Minería, especialmente a Mario Rojo y Patricio Yañez por apoyarnos logísticamente, facilitándonos información y acceso al área de estudio. De la misma manera, agradezco a Ernesto Clavijo y a Álvaro Aliaga, del Departamento de Química de la Universidad de Chile, por estar siempre dispuestos a colaborar con mis muestras en su laboratorio de espectrometría vibracional. También agradecer a Rurik Romero, al Dr. Mathieu Leisen y Christian Nievas por el apoyo técnico en los laboratorios de Microscopía Electrónica y de Espectrometría de Masas del Departamento de Geología de la Universidad de Chile. No puedo dejar de agradecer también al Dr. Víctor Valencia por su disposición, paciencia y cordialidad durante mi estadía en Tucson, Arizona.

De la misma manera, agradezco a mi familia y amigos, quienes ponen las condiciones de borde emocionales en cada uno de mis pasos. Gracias por su apoyo, en especial a aquellos que estuvieron en las discusiones de mis ideas y apoyándome cuándo lo necesité. Por último, agradezco al personal administrativo, cual siempre hizo más venidero mi paso por la Universidad. Agradezco en especial a William, Rosita y Blanca por siempre apoyar y brindarme una conversación cuando fue necesario.

Este trabajo fue financiado por los proyectos FONDECYT 1140780 (Metallogenesis of the Mesozoic magmatic arc of northern Chile: Testing the IOCG connection using multy-proxy geochemical approach) y por el Núcleo Milenio NC1300065 “Trazadores de Metales en Zonas de Subducción”.

TABLA DE CONTENIDO

ÍNDICE DE FIGURAS

CAPITULO I – INTRODUCCIÓN

1.1. Presentación

La Franja Ferrífera Chilena (FFC) se encuentra en la Cordillera de la Costa del norte de Chile, extendiéndose en dirección norte-sur entre las regiones de Atacama (26°S) y Coquimbo (31°S) (**Figura A1**). Esta franja longitudinal de más de 600 km de largo, incluye principalmente depósitos de cobre tipo pórfidos de Cu-Mo-Au e IOCGs y depósitos de hierro tipo Kiruna. La FCC coincide con una faja de intrusivos del Albiano (~110-100 Ma) y la porción sur del Sistema de Falla de Atacama (SFA), el cual corresponde a la estructura más importante del antearco de los Andes Centrales (Cembrano et al., 2005). Los depósitos denominados tipo Kiruna o IOA (*iron-oxide apatite* u óxido de hierro-apatito), corresponden a cuerpos irregulares de magnetita maciza, generalmente enriquecidos en vanadio y pobres en titanio, con proporciones variables de actinolita, apatito y escapolita. Sumado a ello, suelen estar emplazados en rocas volcánicas y volcanoclásticas de edad Cretácica (Segestrom, 1968; Vivallo et al., 1995) y son considerados como parte de un sistema de arco-cuenca de trasarco desarrollado en un contexto de subducción activo durante el Cretácico Inferior (Aguirre, 1985; Vivallo et al., 1995).

A pesar que los yacimientos IOA son la principal fuente de hierro del país su origen, en particular la fuente de fluidos y metales (Barra et al., 2017), y su la posible conexión genética con los depósitos tipo IOCG (*iron-oxide, copper, gold* u óxidos de hierro, con cobre y oro), es tema de discusión.

En particular, la génesis de los depósitos tipo Kiruna andinos ha sido motivo de debate desde mediados del siglo pasado. Algunos autores (e.g., Nyström and Henríquez, 1994, Henríquez et al., 2003) los interpretan como formados por un proceso de segregación magmática de un fundido rico en hierro formado por inmiscibilidad líquida. Este fundido inmiscible rico en hierro ascendería debido a su alto contenido de volátiles y se emplazaría en niveles someros de la corteza. En contraparte, otros autores indican que estos depósitos se habrían originado a través de un proceso de reemplazo metasomático de rocas volcánicas pre-existentes causado por fluidos ricos en hierro de origen magmático o no magmático (e.g., Ménard, 1995, Sillitoe y Burrows, 2002, 2003).

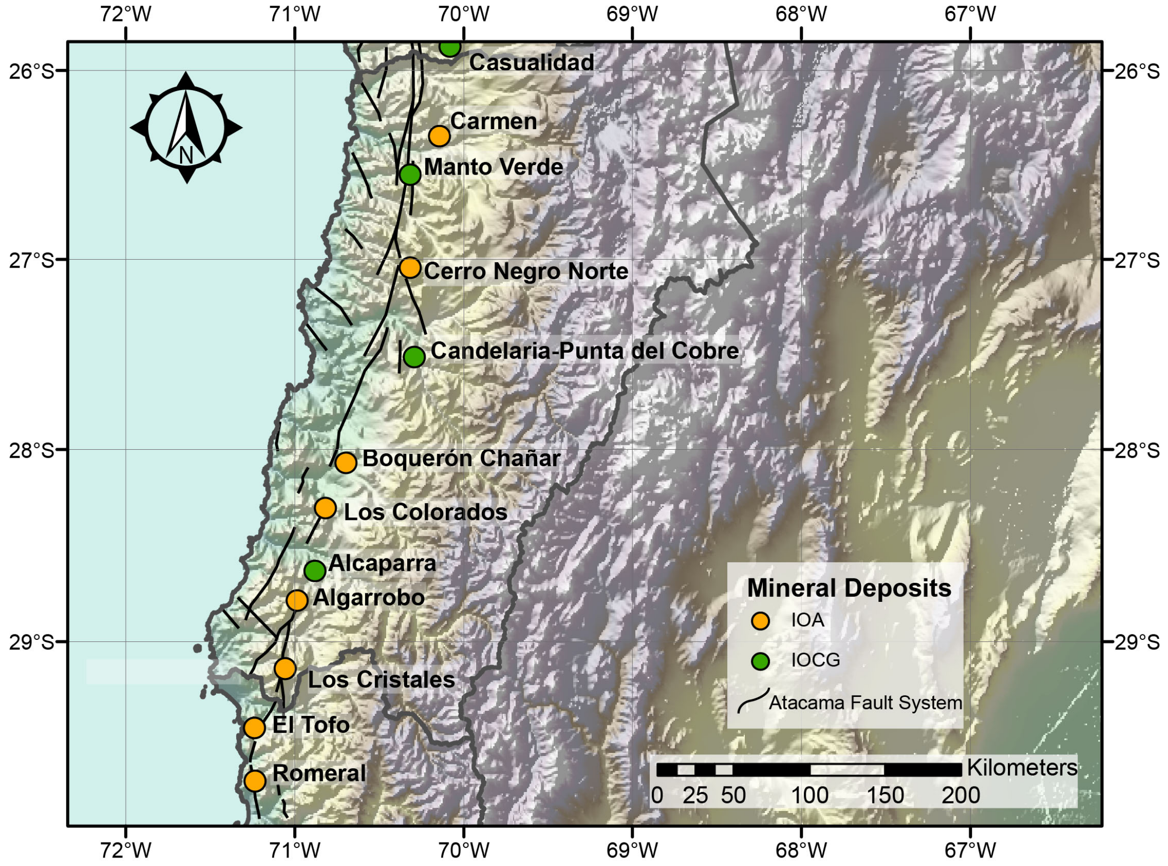

Figura A1: Mapa que ilustra la ubicación de los depósitos IOCG y magnetita-apatito de la III y IV región y su relación con el Sistema de Falla Atacama.

Recientemente, Knipping y colaboradores (2015a) propusieron un nuevo modelo de formación de yacimientos IOA basado en la cristalización inicial de microlitos de magnetita magmática en un magma silicatado en enfriamiento, favoreciendo la nucleación de burbujas a partir de fluidos exsueltos en el magma. Estos pares de magnetita-burbuja coalescen y migran hacia niveles más someros. A medida que ascienden los fluidos (burbujas) no solo extraerían Fe del magma, sino también otros metales como Cu y Au, lo que conllevaría a la precipitación de magnetita de carácter hidrotermal y sulfuros en niveles aún más fríos y someros. Este modelo es consistente con la presencia de depósitos tipo IOCG espacialmente asociados a IOAs, donde los depósitos de magnetita-apatito serían las raíces profundas de un sistema magnatico-hidrotermal que grada hacia un depósito IOCG (Sillitoe, 2003; Reich et al., 2016; Barra et al., 2017).

El modelo de flotación está respaldado por variaciones en la química mineral observada en diferentes tipos de texturas de magnetita en Los Colorados (Knipping et al., 2015a, b) y El Romeral (Rojas et al., 2017b), sumado a datos de isótopos Fe y O determinados en magnetita de Los Colorados (Bilenker et al., 2016). Por otro lado, la transición IOA-IOCG se apoya en las siguientes evidencias: (1), la relación espacial entre ambos, en donde los depósitos tipo Kiruna se asocian directamente a un ambiente extensional o transtensional a lo largo de zonas estructurales mayores (SFA) mientras los depósitos tipo IOCG a estructuras secundarias; (2), presencia de magnetita maciza en etapas tempranas de los IOCGs; (3), semejanza en cuanto a la alteración hidrotermal, generalmente calco-sódica; y (4), estudios recientes en sulfuros, principalmente piritas, que correlacionarían ambos depósitos en un modelo evolutivo magmático-hidrotermal (Reich et al., 2016, Barra et al., 2017). Así, este "modelo de flotación" no solo reconcilia la hipótesis magmática con el modelo hidrotermal, sino que también proporciona una explicación consistente para la relación genética entre los depósitos IOA e IOCG de la Franja Ferrífera Chilena.

Estudios recientes se han centrado en la química de la magnetita (Fe_3O_4) para discriminar entre distintos tipos de yacimientos y determinar el origen (magmático vs hidrotermal) de ésta (Dupuis y Beaudoin, 2011; Nadoll et al., 2014). La magnetita es una fase mineral ubícua en diferentes contextos geológicos con condiciones de formación específicas que se reflejan en su composición de elementos traza (e.g., Dare et al., 2014, 2015; Knipping et al., 2015a, b; Rojas et al., 2017b). Avances recientes en técnicas analíticas (e.g., LA-ICP-MS) han permitido cuantificar concentraciones de elementos traza por debajo de los límites de detección de la microsonda electrónica, lo que resulta en una mejor discriminación entre magnetita de origen ígneo e hidrotermal (Nadoll et al., 2014, 2015; Knipping et al., 2015b). Variados elementos traza pueden ser incorporados dentro de la estructura de magnetita incluyendo Al, Mn, Ti, V, Ni, Cr, Zn, Co, Sn, Ga y Mg. De esta manera, la presencia y concentración de estos elementos puede ser utilizada para construir diagramas de discriminación (Nadoll y Koening, 2011; Nadoll et al., 2014; Dare et al., 2014), y además, para explicar la variación química de la magnetita en cualquier depósito en particular (Knipping et al., 2015a, b).

A fin de contribuir al desarrollo de un modelo genético de los depósitos tipo Kiruna de la franja ferrífera del norte de Chile, este trabajo de tesis se enfoca en la química mineral de la magnetita del yacimiento Cerro Negro Norte, ubicado aproximadamente a 32 km de la ciudad de Copiapó. El yacimiento está formado por 5 grandes cuerpos de magnetita los cuales son, de mayor a menor tamaño: Abanderada, Augusta, Beduino, Veta Central y Cata Alfaro (Vivallo et al., 1995; Raab, 2001) (**Figura A2**). En este depósito no se han realizado estudios recientes acerca del origen de la mineralización, por lo que en el presente se busca esclarecer su génesis utilizando variadas técnicas de microanálisis apoyados en la petrografía.

La presente tesis consta de tres capítulos principales: una Introducción, seguido de un artículo científico titulado *Trace-element geochemistry of magnetite from the Cerro Negro Norte iron oxide-apatite deposit, northern Chile,* en donde se integran todos los resultados obtenidos y en donde se establece la metodología empleada, la petrografía y paragénesis del yacimiento, la datación del intrusivo asociado a la mineralización de hierro, resultados de isótopos estables de azufre y análisis de elementos mayores y traza en fases en magnetita mediante microsonda electrónica y ablación laser-espectrómetro de masas. El último capítulo de esta tesis presenta las Conclusiones generales del trabajo realizado.

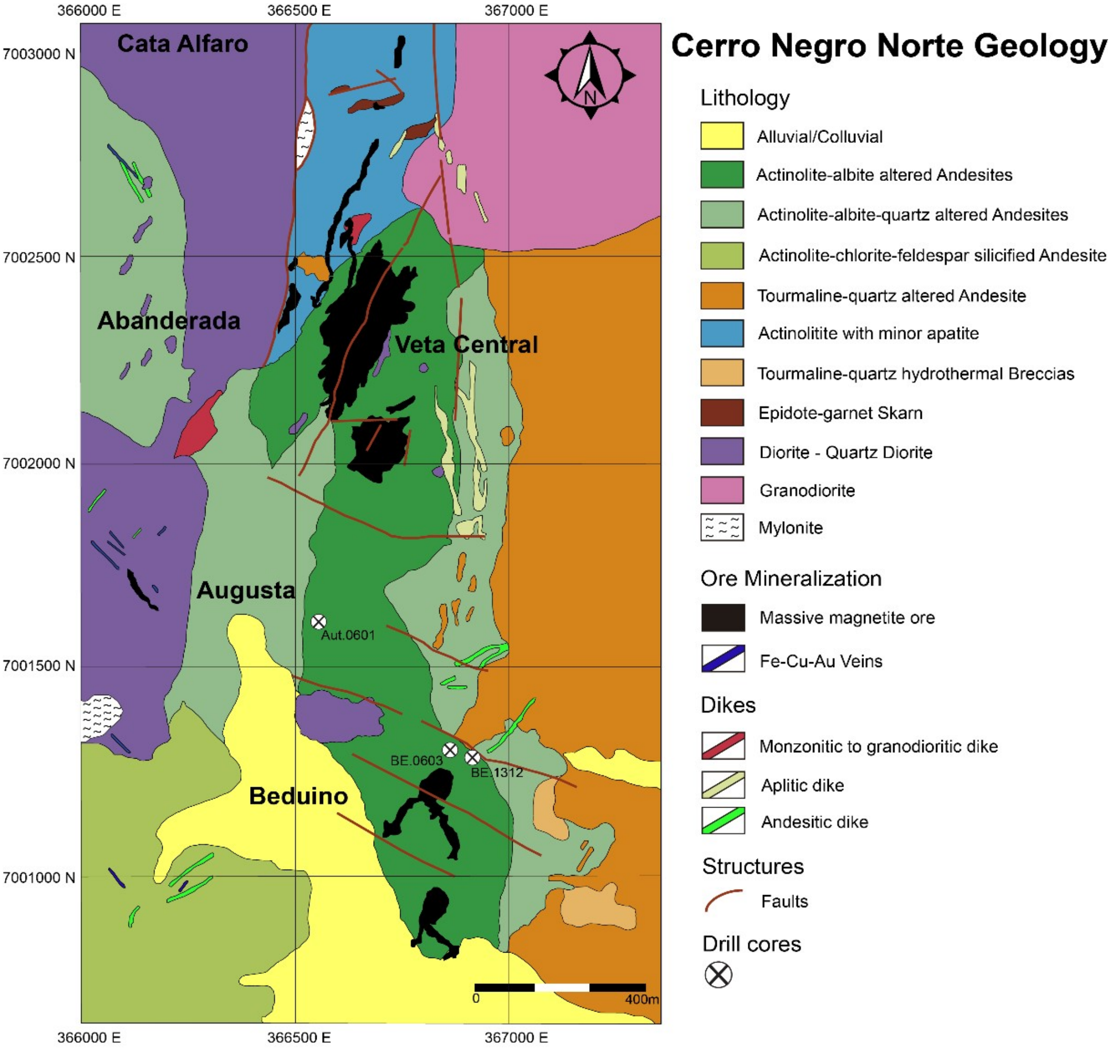

Figura A2: Mapa geológico del depósito Cerro Negro Norte con la ubicación de los sondajes utilizados. Modificado de CMP (2017).

Este trabajo fue financiado por el proyecto FONDECYT: *Metallogenesis of the Mesozoic magmatic arc of northern Chile: Testing the IOCG connection using a multy-proxy geochemical approach* con el Dr. Fernando Barra como investigador principal y profesor guía de este trabajo. Esta tesis se enmarca además dentro del Núcleo Milenio Trazadores de Metales en Zonas de Subducción (NMTM), proyecto financiado por la Iniciativa Científica Milenio (ICM) del Ministerio de Economía, Fomento y Turismo, y que tiene al Dr. Martin Reich como director y el Dr. Fernando Barra como director alterno.

1.2. Objetivos

1.2.1. Generales

Determinar la química mineral de magnetita en el yacimiento IOA Cerro Negro Norte a fin de comprender los procesos que dieron origen a la mineralización de hierro y aportar nuevos antecedentes para el modelo genético de los depósitos tipo Kiruna de la franja ferrífera chilena

1.2.2. Específicos

1. Estudiar la mineralogía de mena, ganga y la alteración hidrotermal asociada por medio de muestras obtenidas de sondajes y en superficie.

2. Establecer una caracterización química detallada de las distintas generaciones de magnetita.

3. Constreñir la edad de formación del depósito mediante la datación del cuerpo intrusivo diorítico asociado a la mineralización de hierro.

4. Establecer un modelo genético para el yacimiento Cerro Negro Norte y proporcionar nuevos antecedentes al modelo de flotación propuesto por Knipping et al. (2015a).

1.3. Hipótesis de trabajo

Las variaciones composicionales y texturales de los cristales de magnetita darían cuenta de una transición entre condiciones netamente magmáticas a condiciones hidrotermales, revelando un origen magmático-hidrotermal para el depósito Cerro Negro Norte. Esta transición estaría reflejada en la concentración de elementos traza, tales como el Ti, Al, Mn, Mg, V y Ga en la magnetita, cuya variación respondería principalmente a cambios en las condiciones de temperatura, en un proceso continuo desde niveles más profundos y calientes a otros más someros y fríos. En esta última etapa se depositarían los sulfuros de Cu y Fe, además de Au como la expresión más hidrotermal del sistema y que representaría una transición gradual a un sistema tipo IOCG.

1.4. Ubicación y Acceso

El distrito ferrífero Cerro Negro Norte se ubica en la Región de Atacama, aproximadamente a 37 km al noreste de la ciudad de Copiapó, entre las coordenadas UTM 7003000N-700100N and UTM 366000E-367500E, las que corresponden al punto central ubicado dentro del rajo del depósito. Se accede desde la ciudad de Copiapó por la Ruta 5 para luego desviar hacia el camino C-327 que conduce directamente a la faena (**Figura A3**).

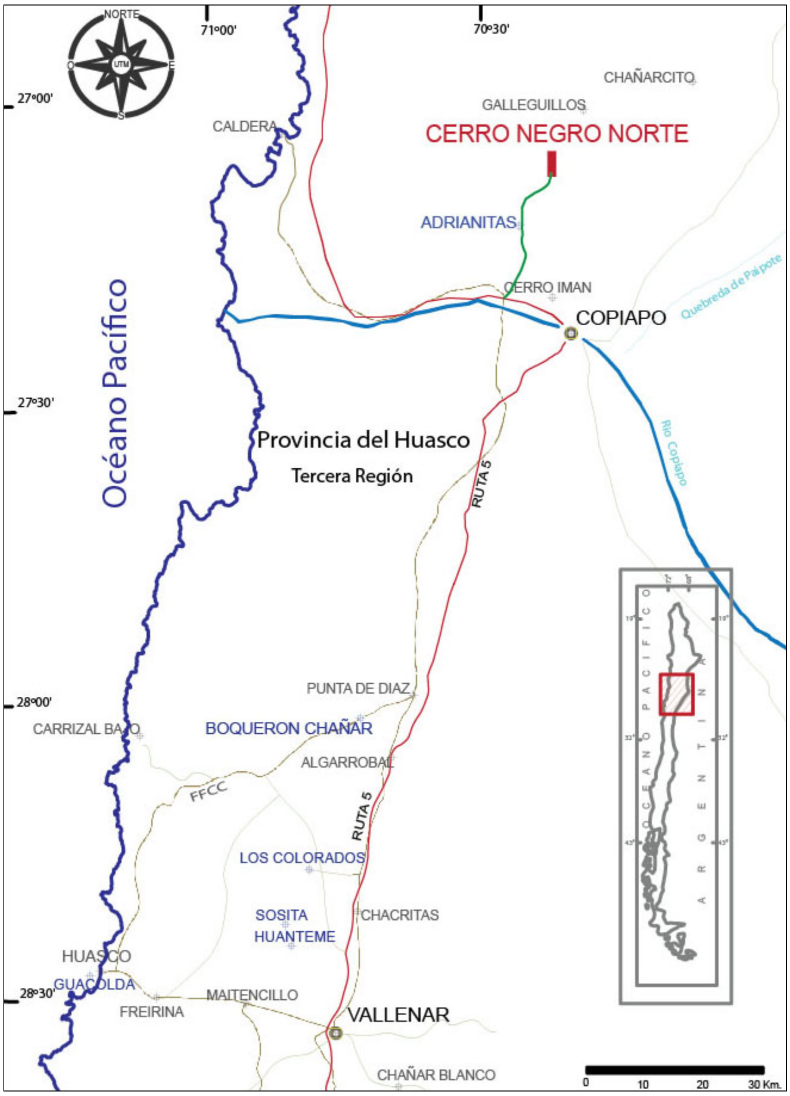

Figura A3: Ubicación y acceso a Cerro Negro Norte.

CAPÍTULO II

Trace-element geochemistry of magnetite from the Cerro Negro Norte iron oxide-apatite deposit, northern Chile

Eduardo Salazar[1], Fernando Barra[1], Martin Reich[1], Adam Simon[2], Mathieu Leisen[1], Gisella Palma[1], Rurik Romero[1], Mario Rojo[3]

[1] Department of Geology and Andean Geothermal Center of Excellence (CEGA), FCFM, Universidad de Chile, Plaza Ercilla 803, Santiago, Chile.

[2] Department of Earth and Environmental Sciences, University of Michigan, 1100 North University Ave, Ann Arbor, Michigan, USA.

[3] Compañía Minera del Pacífico (CMP), Pedro Pablo Muñoz 675, La Serena, Chile.

Submitted to

Mineralium Deposita

Corresponding author: Fernando Barra
Department of Geology and Andean Geothermal Center of Excellence (CEGA), FCFM,
Universidad de Chile, Plaza Ercilla 803, Santiago, Chile
fbarrapantoja@ing.uchile.cl

ABSTRACT

Kiruna-type iron oxide-apatite (IOA) deposits constitute an important source of iron and phosphorous, and potentially of rare earth elements (REE). However, the origin of IOA deposits is still a matter of debate with models that range from a purely magmatic origin by liquid immiscibility to replacement of host rocks by hydrothermal fluids from different sources. In order to better constrain the origin of Andean IOA deposits we focused on the Cretaceous Cerro Negro Norte deposit located in the Chilean Iron Belt, northern Chile. The Cerro Negro Norte magnetite ore is hosted in andesitic rocks and is spatially associated with a diorite intrusion. The deposit is characterized by two main mineralization/alteration episodes: an early Fe oxide event with magnetite and actinolite followed by four stages that comprise the main hydrothermal event (hydrothermal magnetite + actinolite; calcic-sodic alteration + sulfides; quartz-tourmaline and propylitic alteration). A late episode of supergene alteration is poorly developed. Based on textural and chemical characteristics, four different types of magnetite are recognized at Cerro Negro Norte: Type I, represented by high-temperature magnetite cores with amphibole, pyroxene and minor Ti-Fe oxide inclusions; Type II, an inclusion-free magnetite, usually surrounding Type I magnetite cores; Type III corresponds to an inclusion-free magnetite with chemical zoning formed under moderate temperatures; and Type IV magnetite contains abundant inclusions and is related to low temperature hydrothermal veinlets. EPMA and LA-ICP-MS analyses of the four magnetite types show that the incorporation of Al, Mn, Ti, and V within the magnetite structure is controlled by temperature. Vanadium and Ga contents are relatively consistent within each magnetite type, but are statistically different among magnetite types, suggesting that both elements could be used to discriminate between magmatic and hydrothermal magnetite. However, our results show that the use of elemental discrimination diagrams should be coupled with detailed textural studies in order to identify superimposed metasomatic events, and evaluate the impact of inclusions on the interpretation of microanalytical data. The presence of a distinct textural and chemical variation between cores and rims (Type I and II magnetite) is explained by a transition from purely magmatic to magmatic-hydrothermal conditions. The micro-analytical data of magnetite presented here, coupled with new δ^{34}S data for pyrite (-0.5 to +4.3‰) and U-Pb ages of the diorite (129.6 ± 1.0 Ma), are indicative of a genetic connection between diorite intrusion and magnetite mineralization, supporting a magmatic-hydrothermal flotation model to explain the origin of Kiruna-type deposits in the Coastal Cordillera of northern Chile.

Keywords: Magnetite; trace element geochemistry; Andean IOCG clan; iron oxide-apatite deposits; Chile

INTRODUCTION

The Cretaceous metallogenetic belt located in the Coastal Cordillera of northern Chile extends for more than 1000 km in a roughly north-south direction between 22° to 31°S (Fig. 1). This belt comprises intrusive bodies (~190-100 Ma) emplaced along the Atacama Fault System (AFS), volcanic and volcanoclastic rocks of Late Jurassic to Late Cretaceous age, and diverse types of mineral deposits, including stratabound Cu(-Ag), porphyry Cu-Mo(-Au), iron oxide-copper-gold (IOCG), and iron oxide-apatite (IOA) deposits (Ruíz et al. 1965; Espinoza 1990; Barra et al. 2017). Most IOCG and IOA deposits are located in the southern portion of this metallogenetic belt (26° to 31°S) in what is known as the Chilean Iron Belt (Fig. 1).

IOCG and IOA deposits constitute end-members of a diverse group of ore deposits which have been classified into the "IOCG clan" (Williams et al. 2005; Barton 2014). IOCG deposits *s.s.* are characterized by a high content of magnetite and/or hematite with variable concentrations of sulfides (pyrite and chalcopyrite) and where Cu and Au are the economically profitable metals (Williams et al. 2005). IOA or "Kiruna-type" deposits, on the other hand, are mostly magnetite-rich deposits with abundant actinolite, minor hematite (martite) and apatite, and are mined for their iron ore. In the Chilean Iron Belt, these deposits were mostly emplaced in volcanic rocks formed within a back-arc basin tectonic setting developed in an active subduction context during the Upper Jurassic-Lower Cretaceous (Aguirre 1985; Mpodozis and Ramos 1990).

The large variability of geological and mineralogical characteristics found in deposits of the IOCG clan has resulted in several disagreements regarding their origin. Recent Re-Os isotope data on IOCGs show that for Andean deposits the source of metals and fluids is of magmatic-hydrothermal origin, whereas for other IOCGs (e.g., Lala, China, Zhimin and Yali 2013; Olympic Dam, Australia, McInnes et al. 2008) their higher Re and Os concentrations and higher radiogenic Os initial ratios indicate a more crustal source for the metals, where basinal brines could have been involved (Barra et al. 2017). These findings support the idea that IOCG hydrothermal deposits can be formed by different sources and processes. In addition, the origin of IOA deposits is also subject of controversy. Some authors (e.g., Nyström and Henríquez 1994; Tornos et al. 2016) interpret them as formed by an immiscible magnetite-rich melt with a high oxygen fugacity and volatile content, which would reduce its density allowing its ascent to shallow crustal levels. In contrast, other authors indicate that these deposits formed by hydrothermal replacement of volcanic host rocks (e.g., Sillitoe and Burrows 2002) caused by Fe-rich fluids of magmatic or non-magmatic origin (Ménard 1995).

Several recent studies have focused on the chemistry of magnetite (Fe_3O_4) to provide some insights on the formation of the different magnetite bearing deposits (Dare et al. 2014; Nadoll et al. 2014). Magnetite is an ubiquitous mineral phase in different geological environments and the specific conditions at which magnetite crystallized are reflected in its trace element composition (e.g., Loberg and Horndahl 1983; Dare et al. 2014, 2015; Nadoll et al. 2014, 2015; Knipping et al. 2015a,b; Rojas et al. 2018a). Several trace elements can be incorporated within the magnetite structure, i.e., Al, Mn, Ti, V, Ni, Cr, Zn, Co, Sn, Ga, and Mg. Hence, the presence and concentration of these elements have been used to construct discrimination diagrams (Dupuis and Beaudoin 2011; Nadoll et al. 2014; Dare et al. 2014; Wen et al. 2017) and to explain the chemical variation of magnetite for any particular deposit. In addition, improvements in analytical techniques (e.g., LA-ICP-MS) have made it possible to precisely measure these trace elements resulting in a better discrimination between hydrothermal and magmatic magnetite (Nadoll and Koenig 2011; Dare et al. 2014; Nadoll et al. 2014).

Recently, Knipping et al. (2015a,b) used the trace element composition of different textural types of magnetite identified at the Los Colorados IOA deposit to propose a novel “flotation model” to explain the formation of IOA deposits. This model involves the crystallization of igneous magnetite microlites within a cooling silicate magma that will ascend by interaction with fluids exsolved from the magma. The ascending magnetite-fluid suspension will coalescence to form the massive magnetite ore bodies in regional-scale transcurrent faults. In addition, the high-salinity hydrothermal fluids that nucleate on magnetite grains will not only extract Fe from the magma but also other metals such as Cu and Au, which would lead to the precipitation of copper sulfides and hydrothermal magnetite at cooler and shallower levels forming in some cases an IOCG-type deposit (Knipping et al. 2015a,b; Reich et al. 2016; Barra et al. 2017; Rojas et al. 2018a,b). The flotation model is supported by variations in the mineral chemistry observed in different textural types of magnetite at the Los Colorados (Knipping et al. 2015a,b) and El Romeral (Rojas et al. 2018a) IOA deposits in the Chilean Iron Belt. The chemical composition of the magnetite grains reflects their formation conditions, from purely magmatic at deeper levels of the mineral system to low-T hydrothermal at shallow levels. Further evidence for a magmatic component is supported by Fe and O isotope data determined in magnetite from Los Colorados (Bilenker et al. 2016). Thus, the flotation model not only reconciles the magmatic with the hydrothermal model, but also provides a consistent explanation for the genetic relation between IOA and IOCG deposits in the Andean IOCG province.

The Cretaceous Chilean Iron Belt is an ideal site to study the formation of these deposits because their primary geologic features remain mostly undisturbed by later superimposed metamorphic or metasomatic events. The present work focuses on the Cerro Negro Norte IOA deposit located in the Coastal Cordillera of northern Chile, near the city of Copiapó (Fig. 1). The main purpose of this study is to provide new constraints on the formation of Andean IOA deposits using field observations, petrographic and textural studies, geochronology, mineral chemistry (EPMA and LA-ICP-MS) and sulfur isotope data for the Cerro Negro Norte deposit.

2.1. GEOLOGICAL BACKGROUND

The Coastal Cordillera of northern Chile comprises several dioritic to monzodioritic plutonic complexes with ages ranging from ca. 190 to 100 Ma (Groccott and Taylor 2002). These complexes intrude thick piles of volcanic and volcanoclastic rocks formed in an intra and/or back-arc environment, mainly represented by the Jurassic La Negra and the Early Cretaceous Punta del Cobre and Bandurrias formations (Lara and Godoy 1998; Arévalo 2005). The extensive early Middle Jurassic to Early Cretaceous igneous activity that characterizes the Coastal Cordillera occurred under extensional conditions in response to the slab roll-back and the Mariana-type high-angle subduction (Mpodozis and Ramos 1990; Grocott and Taylor 2002). Along the Coastal Cordillera of northern Chile and southern Perú, the western portion of the Mesozoic arc and its respective fore-arc appears to have been removed by subduction erosion or lateral displacement (Mpodozis and Ramos 1990).

The Atacama Fault System (AFS, Fig. 1), the most important structure of the Chilean Central Andes fore-arc, extends for approximately 1000 km between 21° and 30°S (Scheuber and Andriessen 1990; Brown et al. 1993; Cembrano et al. 2005). The AFS is a trench-parallel, strike-slip fault system, which comprises different subvertical segments of up to 10 km long and a general NNW-NNE orientation (Scheuber and González 1999). The large-scale geometry of the AFS was constructed during the Late Jurassic to Early Cretaceous, near the end of the Jurassic magmatic activity (Cembrano et al. 2005). Progressive cooling during the last magmatic stages of this arc resulted in a change in the deformation style from a shallow ductile regime (<10 km) represented by amphibolite facies (150-143 Ma) and greenschists (139-125 Ma) (Scheuber et al. 1995) to a fragile regime evidenced by chlorite and epidote-rich cataclasites (125-118 Ma) (Cembrano et al. 2005). The AFS kinematics of fragile structures is mainly sinistral with a minor extensional component (e.g., Scheuber and Andriessen 1990). This has been attributed to the high oblique convergence of the Aluk plate under the South American plate during the Mesozoic (Scheuber and González 1999). Late Cretaceous tectonic inversion was caused by transpressive kinematics, triggered by the final opening of the Atlantic Ocean basin (Mpodozis and Ramos 1990). A mild deformation in the Coastal Cordillera of northernmost Chile and southern Perú took place in a fore-arc environment from the Middle Cretaceous (Amilibia et al. 2008).

The Cretaceous Chilean Iron Belt located in the Coastal Cordillera between 26° to 31°S corresponds to a longitudinal belt of iron-rich deposits that extends for over 600 km and is coincident with the position of an Albian intrusive belt (~130-100 Ma) and the southern portion of the AFS. The IOA deposits (e.g., Los Colorados, El Algarrobo, El Romeral, Cerro Negro

Norte) are mostly hosted in volcanic rocks assigned to the La Negra, Bandurrias or Punta del Cobre formations (Segerstrom 1968; Vivallo et al. 1995a,b) formed in an arc/back-arc basin system developed during the Late Jurassic-Early Cretaceous.

2.2. GEOLOGY OF THE CERRO NEGRO NORTE DEPOSIT

The Cerro Negro Norte IOA deposit is at ca. 27º05´S and 70º21´W (Fig. 1), approximately 37 km northwest from the city of Copiapó, and is hosted in volcanic and volcanoclastic rocks of the Bandurrias Formation (Fig. 2). The deposit is currently mined by Compañía Minera del Pacífico (CMP), and estimated resources are at 657.3 Mt with 29.7% Fe (CAP Minería Annual Report 2016). The Cerro Negro Norte host rocks are breccias and andesitic lavas that represent a roof pendant of volcanic rocks interspersed with granitoids. To the east, the Cerro Negro Norte deposit is limited by the Portezuelo Cucharas aplites and the La Borracha Pluton (Fig. 2), a relatively homogeneous monzonite to monzodiorite intrusion. To the west, the deposit is limited by the La Brea Diorite (123-117 Ma, Arévalo 1995) and the Sierras Pajas Blancas granodiorite (K-Ar age 103 ± 5 Ma; Arévalo 1995; Fig. 2).

Small monzodiorite to granodiorite intrusions and dikes are present in the district. These dikes have a general NNE orientation and intrude the diorite (and/or quartz-diorite) stocks as well as the andesite rocks and magnetite bodies (Vivallo et al. 1995a; Raab 2001) (Fig. 3). Post-mineral andesite dikes striking NNE and EW have been reported in the Abanderada, Veta Central and NE of the Beduino area (Raab 2001; Fig. 3). West of the Abanderada area, these dikes appear to be related to sulfide (pyrite + chalcopyrite) mineralization (Raab 2001). In general, these rocks exhibit a propylitic ± sericite ± clay alteration having up to 2% of disseminated magnetite.

Minor mylonite zones up to 50 m thick have been described at the contact between the andesite and the diorite (Vivallo et al. 1995a; Raab 2001). These mylonites are dominated by actinolite, which occurs both in the groundmass and in bands up to 4 mm thick. Locally, veinlets of scapolite + actinolite + titanite are observed cross-cutting magnetite veins. These, in turn, cut banded mylonite with scapolite and moderately altered pyroxene (Raab 2001).

The Cerro Negro Norte deposit comprises five magnetite ore zones from north to south: Cata Alfaro, Abanderada, Veta Central, Augusta, and Beduino (Fig. 3). The massive magnetite bodies form vertical to subvertical elongate bodies, tabular to lobular in shape, with a general NS orientation and distributed in an area of about 0.5 x 5 km^2. The mineralization includes large amounts of magnetite locally altered to hematite (martitization), minor sulfides (pyrite-chalcopyrite) and occasional copper oxides. The iron ore bodies consist of massive and disseminated magnetite with actinolite and minor apatite, pyrite and chalcopyrite. According to their textural characteristics the magnetite ore can be classified into massive, brecciated, stockwork and disseminated. These bodies may exhibit abrupt contacts (e.g., eastern Abanderada) or gradational with respect to the host rock (e.g., western Abanderada, Veta Central), where magnetite is disseminated within the andesite. In addition, north of the Abanderada area, it is possible to observe tabular magnetite bodies with a NNE orientation that would indicate areas of weakness and fluid circulation (Raab 2001). Subhorizontal massive ore bodies a couple meters thick, with variable extension and shape, show clear contacts with the andesite rock in the Veta Central and Cata Alfaro areas (Vivallo et al. 1995a; Raab 2001).

These bodies are usually interstratified with volcanic rocks that have been interpreted as total replacement of andesitic lava flows by the magnetite (Raab 2001) or as intrusive and/or extrusive bodies of magnetite (Vivallo et al. 1995a). Disseminated magnetite mineralization occurs mainly in the andesite host rocks and, to a lesser extent, in diorite or monzodiorite-granodiorite dikes. Brecciated magnetite bodies are described to the east of Abanderada, north of Veta Central, and Cata Alfaro. In addition, it is possible to observe quartz-diorite igneous breccias with magnetite clasts spatially associated with monzodiorite-granodiorite dikes (Raab 2001).

The alteration is defined by a pervasive actinolitization of the andesitic host rocks around the Fe ore (Fig. 3), grading outward to an actinolite-albite ± quartz zone. To the east a tourmaline-quartz zone is dominant. In the tourmaline-quartz zone it is also possible to observe andesite clasts with a strong albitization and local presence of K-feldspar (Vivallo et al. 1995a; Raab 2001).

2.3. ANALYTICAL METHODS

Samples were collected from the Beduino (drill cores BE.1312: 248 m and BE.0603: 342 m) and Augusta (drill core Aut.0601: 215 m) ore bodies (Fig. 3). Additional samples were collected in the Veta Central pit. Drill hole Aut.0601 cuts the main ore body at depth, whereas the Beduino drill holes cut minor ore bodies located at the southern part of the deposit (Fig. 3). Thin and thick sections (100 µm) were made for petrography and for electron probe microanalysis (EPMA), and laser ablation inductively coupled plasma mass spectrometry (LA-ICP-MS) measurements, respectively. Samples were studied under a polarized light microscope and by using a FEI Quanta 250 scanning electron microscope (SEM) equipped with secondary electron (SE), backscattered electron (BSE) and cathodoluminescence (CL) detectors, and a solid state X-ray energy dispersive spectrometer (EDS) at the Andean Geothermal Centre of Excellence (CEGA), Universidad de Chile, to identify and characterize the ore and alteration mineralogy. Micro-analytical methods used in this study are detailed below.

Microanalysis and elemental mapping: The electron probe microanalyses were performed at the Michael J. Drake Electron Microprobe Laboratory, University of Arizona, Tucson, USA by using a Cameca SX-100 instrument. Aluminum, Si, Cr, Ti, V, Ca, Fe, Mn, Mg, Zn, Ni, Cu, Na, and K were analyzed in magnetite grains with a mean detection limit of ca. 500 ppm. A focused beam (2 μm) was used to avoid hitting any inclusions or exsolution lamellae within the grains. Analytical conditions were 40º take-off angle and a beam energy of 15 keV. A fully focused beam with a current of 20 nA was used. Additionally, wavelength-dispersive spectrometry (WDS) X-ray maps were acquired using an accelerating voltage of 15 kV, a beam current of 80 nA and a counting time of 12 ms/step.

Trace element analysis: Laser ablation-ICP-MS measurements were performed on magnetite grains from six samples collected at different depths by using a Photon Machines Analyte G2 193 nm ArF excimer laser coupled to a Thermo Fisher Scientific iCAP-Q cuadrupole mass spectrometer ablation at the CEGA Mass Spectrometry Laboratory, Department of Geology, Universidad de Chile. The mass spectrometer was tuned to a high sensitivity and a simultaneous low oxide formation rate (ThO/Th <0.5). Since helium was used as a carrier and argon as a plasma gas, interferences with these elements as well as with oxides of these elements and double charged ions were taken into account when choosing representative isotopes for each element. Thus, ^{57}Fe was measured for the iron content, instead of the more abundant ^{56}Fe that has an interference with ArO. Thirty seconds of background were measured for baseline correction prior to sample analysis, and a sample-standard bracketing method (2x standard, 2x secondary standard, 18x samples, and 2x standard) was used for instrumental drift correction.

The USGS GSE-1G reference material was used for magnetite analysis and the USGS GSD-1G as a secondary standard. The Fe content of magnetite determined by EPMA was used as the internal standard. The Al and V content determined by LA-ICP-MS are in good agreement with concentrations determined by EPMA, which supports the use of the GSE-1G reference material as suitable standard for magnetite laser ablation analysis. A 40 µm laser spot size was used for measurements, which was the best compromise between analyzing inclusion-free areas and measuring above the detection limit of most elements. In total, 37 elements were measured with dwell times of 10 ms to achieve measureable concentration of these elements. Analyses were performed by using a laser repetition pulse of 5 Hz for 60 s per each spot with fluence of 4.0 J/cm^2. Data reduction was carried out with the Iolite software (Paton et al. 2011), which calculates detection limits after Longerich et al. (1996). The influence of micro- to nano-meter sized inclusions within magnetite growth zones (Deditius et al. 2018) could not be totally avoided due to the laser beam size. Analyses affected by the presence of inclusions were filtered through integrating data processing and removed from the dataset.

U-Pb dating: Uranium-lead dating was carried out on zircons extracted from a diorite sample from the Veta Central pit (Fig. 3), which possibly corresponds to La Brea diorite. Zircon grains were separated at the Zirchron LLCC (Tucson, Arizona) using electro-pulse disaggregation. The disaggregated sample is sieved and collected into a water beaker. The fine, light fraction is removed from the water and the mineral concentrate is sieved through a 50’ mesh (300 µm). The dried sample is later passed through a LB-1 Frantz Magnetic Barrier Separator to remove the magnetic fraction. Finally, heavy liquid (methylene iodide) is used to collect the zircons by decantation.

Mounting and isotopic analysis were carried out at the CEGA Mass Spectrometry Laboratory, Universidad de Chile. Zircons were mounted in epoxy resin and later polished. Cathodoluminescence images were obtained by using a Centaurus CL detector coupled to an SEM. For U-Pb dating a laser ablation system (Analyte G2) coupled to an iCAP-Q mass spectrometer. A spot size of 50 µm, a repetition rate of 10Hz, and a fluence of 2.5 mJ/cm^2 was used for the U-Pb analyses. A sample bracketing method was performed with Plešovice (Sláma et al. 2008) and Temora2 (Black et al. 2004) reference materials. The data reduction was performed by using Iolite (Paton et al. 2011) and the statistical process was done with Isoplot 4.0 (Ludwig 2010).

Sulfur isotopes: Stable isotopes of sulfur were measured in pyrite from seven samples; two corresponding to the BE.1312 drill-core, three from the BE.0603 drill-core, and two from Aut.0601 drill-core. Pyrite concentrates were prepared by grinding the samples by using a stainless steel mortar, followed by hand-picking of pyrite grains by using titanium tweezers to avoid grains impurities. The mineral concentrates were sent to the Environmental Isotope Laboratory, Department of Geosciences, University of Arizona, Tucson, AZ. A continuous-flow gas-ratio mass spectrometer (CF-IRMS) ThermoQuest Finnigan Delta PlusXL model with coupled Costech elemental analyzer was used for $^{34}S/^{32}S$ ratio measurements. The sulfide grains were introduced into a combustion chamber with O_2 and V_2O_5 (Coleman and Moore 1978) obtaining a SO_2 gas at 1030 °C, which is the analyzed product. The system was calibrated by using two international standards corresponding to OGS-1, which is a $BaSO_4$ precipitated from seawater, and NBS123, a sphalerite sample with a $\delta^{34}S$ value of +17.09 ‰. A linear calibration between -10 and +30 ‰ was used and a precision of ±0.15 or 1σ was estimated by diverse internal standards measurements. Sulfur isotope data are reported in delta notation as per mil (‰) values, where $\delta^{34}S = [[(^{34}S/^{32}S)_{sample} - (^{34}S/^{32}S)_{standard}] / (^{34}S/^{32}S)_{standard}] \times 1000$.

2.4. RESULTS

2.4.1. Rock types

a) Andesite: the andesitic rocks are characterized by their gray to dark green color and a porphyritic texture with up to 25 % modal of subhedral to euhedral plagioclase phenocrysts ranging in size from 0.5 to 3 mm long (Fig. 4a). Phenocrysts of clinopyroxene (up to 0.5 mm) and hornblende (up to 2.5 mm) are also observed and may reach up to 10 % modal of the sample. The fine-grained groundmass is dominated by plagioclase with minor quartz and clinopyroxene. Variable amounts of hydrothermal mineral phases such as scapolite, albite, epidote, titanite, quartz, calcite, chlorite, and sericite are also observed in the altered andesite rocks. At the eastern margin of the deposit, the andesite appears almost completely altered to tourmaline with quartz, minor sericite and chlorite. The contact between the andesite and the intrusive rocks on the eastern flank is not well defined due to the intense alteration. The magnetite ore is hosted mostly in the andesites.

b) Diorite and quartz diorite stocks: Diorite intrusions (Fig. 4b) are present at the western part of the deposit (Fig. 3). These rocks have an equigranular texture with 50-75 % modal of sub- to euhedral plagioclase with concentric oscillatory zoning. Quartz is usually less than 10 % modal but can reach up to 20 % modal. These rocks show a calcic and sodic alteration with actinolite and subordinate epidote replacing primary pyroxene and amphibole, and scapolite + albite ± sericite replacing plagioclase. Titanite is a common and ubiquitous alteration phase in these rocks in particular south of the Abanderada area, where it can reach up to 10 % modal (Raab 2001). The quartz diorite rocks shows up to 70 % modal of partially sericitized plagioclase, chlorite after actinolite, and up to 15 % modal anhedral quartz.

2.4.2. Hydrothermal alteration

Four main alteration types are observed in Cerro Negro Norte.

a) Actinolitization: Corresponds to the main alteration style and represents the first alteration event in the deposit. It preferably affects the andesite host rocks; however, it is also observed as an alteration phase of the diorite intrusions. Actinolite is usually dark-green, fine- to coarse-grained observed as large aggregates associated with massive magnetite (Fig. 4c), veinlets ranging from 1 mm to 10 cm in thickness (Fig. 4d) and as replacement of hornblende and/or pyroxene.

The actinolitized rocks are partially altered to chlorite, and sometimes include calcite and quartz. Actinolite veinlets can be associated with scapolite ± apatite ± plagioclase ± quartz ± sulfides (Fig. 4d). Large actinolite crystals, with or without preferred orientation are observable in thin section (Fig. 5a), where it is also evident that the actinolite-rich calcium alteration precedes the sodium alteration with scapolite and albite.

b) *Calcic-sodic alteration:* This alteration type is characterized by a scapolite-rich and an albite-rich alteration, both with variable amounts of actinolite. Scapolite alteration is more abundant near the magnetite ore bodies where it is observed as large granular aggregates and thick veinlets mostly associated with the quartz diorite stocks located SW of Beduino (Fig. 3). At a more distal position from the ore bodies, albite is more dominant with scapolite present as fine disseminations and veinlets with epidote and quartz.

In thin section, scapolite appears as anhedral to subhedral granular aggregates intergrown with actinolite, magnetite and minor apatite (Fig. 5b) or associated with titanite + epidote ± biotite ± magnetite ± calcite ± apatite (Fig. 5c) and with relict clinopyroxene in areas poorly affected by actinolitization. Locally, it is observed as a replacement of euhedral plagioclase in andesite.

Albite was observed as a pseudomorphic replacement of primary plagioclase in andesite and less frequently in veinlets with actinolite + epidote + magnetite ± calcite ± titanite. In some cases plagioclase is altered to sericite (Fig. 5d) or to an assemblage of chlorite, epidote and/or iron oxides.

c) Quartz-tourmaline alteration: Tourmaline + quartz + sericite hydrothermal breccias (Fig. 4e) and andesite/diorite pervasively altered to tourmaline + quartz + sericite + chlorite are observed at the eastern part of the deposit (Fig. 3). Tourmaline breccias have been interpreted as formed after the calco-sodic alteration (Vivallo et al. 1995a).

Petrographic studies show several crystal habits for tourmaline (Fig. 5e), which include sub-triangular euhedral grains with zonations, fine euhedral disseminations, anhedral to subhedral radial fibers, and veinlets. When it appears as interpenetrating tabular or acicular aggregates, the crystals can measure up to 2 mm in length.

c) Propylitic alteration: Corresponds to the chlorite + quartz + calcite ± sericite association (Fig. 5f). Chlorite is commonly found as a replacement of actinolite in andesite, intrusive rocks and ore bodies. It was also observed as sheeted aggregates and interstitial granular aggregates in the groundmass. Veinlets of chlorite + calcite with minor copper carbonates are also observed. In addition, primary plagioclase can be replaced by calcite and locally by titanite. Minor epidote and quartz were observed as anhedral granular aggregates and in fine veinlets. Raab (2001) interpreted this propylitic alteration as a distal and gradational assembly from albite-rich associations, overlapping with calco-sodic alteration.

2.4.3. Mineralization

The massive iron ore body comprises anhedral to cubic-euhedral granular aggregates of magnetite with medium to low integrity and abundant silicate inclusions (Fig. 6a). The magnetite granular aggregates are usually intergrown with actinolite, and can be in contact with pyrite and/or chalcopyrite (Figs. 4f, 6b-f), apatite and titanite. Hematite is observed as small patches within magnetite (Fig. 6a) and as a thin rim on magnetite and/or pyrite (Fig. 6b).

Sulfide mineralization is moderate to minor and comprises mainly pyrite, chalcopyrite and lesser amounts of bornite, pyrrhotite, covellite, and digenite. Pyrite and chalcopyrite are found as inclusions within magnetite grains (Figs. 4f, 6a) but more commonly as veinlets, and as sub- to anhedral disseminated grains in the silicate matrix and/or in simple contact with magnetite (Fig. 6b,c). Chalcopyrite is observed also as inclusions in pyrite (Fig. 6b,c,e) and filling spaces between magnetite grains (Fig. 6d,f). Pyrrhotite is present as small, droplet-shaped inclusions in pyrite, whereas digenite and covellite are found as replacement of bornite and chalcopyrite (Fig. 6e,f).

Sulfide veinlets with pyrite ± chalcopyrite are mostly related to the Ca-Na alteration stage, whereas scarce calcite + Cu carbonate veinlets are associated with the propylitic alteration. Near the surface, sulfides are almost completely oxidized, where jarosite + goethite and minor Cu oxides are observed.

In summary, three main mineralization/alteration events are recognized in the Cerro Negro Norte deposit (Fig. 7). The first stage corresponds to the main Fe oxide mineralization event represented by massive magnetite mineralization with actinolite and minor apatite, and scarce sulfide inclusions (Fig. 6a). This event is followed by the main hydrothermal event, which is divided into four stages. Stage I is characterized by hydrothermal magnetite and abundant actinolite (Fig. 5a); Stage II is represented by pyrite + chalcopyrite ± pyrrhotite ± bornite and corresponds to the main sulfide event associated with the Ca-Na alteration. The sulfide mineralization is present as disseminations within the silicate matrix (Fig. 6e), between magnetite grains (Fig. 6c,d), and mainly as veinlets dominantly controlled by shear zones or NNW faults (Vivallo et al. 1995a,b; Raab 2001). Stage III is the barren quartz-tourmaline breccia event described above (Fig. 4e), and Stage IV corresponds to the propylitic alteration (chlorite-calcite) with sulfide veinlets and minor Cu carbonates. The last event is the supergene stage with Fe-oxides and hydroxides, minor copper oxides and replacement of primary sulfides by digenite and/or covellite (Fig. 6e,f). Although no gold grains were observed in our samples, previous studies indicate that gold is associated with the pyrite ± chalcopyrite veins and the quartz-tourmaline alteration (Vivallo et al. 1995b; Raab 2001).

2.4.4. Magnetite textures and chemistry

Different magnetite types were identified based on textures (Fig. 8). The most relevant types are magnetite Type I, which contains abundant inclusions, and inclusion-free magnetite Type II (Fig. 8a,b). In magnetite Type I, inclusions vary in size from nano-meter size to a few tens of µm that are randomly distributed and/or are arranged following crystallographic planes in magnetite. In general, the inclusion-free magnetite (Type II) is observed as an overgrowth on inclusion-rich Type I magnetite grains. These two magnetite types account for more than 90 % modal of magnetite in the ore bodies. A third type of magnetite (Type III) is observed as large (up to 100 µm) sub- to idiomorphic octahedral grains with an inclusion-free core and displaying a cryptic zonation towards the rim of the crystal (Fig. 8c). Type IV corresponds to a late magnetite vein event that crosscuts all other magnetite grain types. Some of these magnetite grains display micron- to sub-micron-sized inclusions arranged in a sinuous oscillatory zoning (Fig. 8d).

Elements including Si, Al, Ca, Na, K, and V were analyzed by using EPMA. However, most of the measurements were below the detection limit (150-400 ppm) except for V, Si and Al (Table SM1). X-ray elemental maps for individual grains were also obtained by using WDS (Fig. 9). A general trend of depletion in Mg, Al, Ca, Mn, and Ti was identified from core to the rim in the analyzed magnetite grains. Nevertheless, in some cases magnetite rims show a slight enrichment in Ti and Al (Type I, Fig. 9a); Ti, Mg and Si (Type III, Fig. 9b); and Mg, Al and Si (Type IV, Fig. 9c).

LA-ICP-MS spot analysis was performed to determine the trace element concentration on roughly the same EPMA points avoiding when possible any visible inclusions. Although the position for each laser spot (40 µm diameter) was set manually, some micro- to nano-sized inclusions affected some analyses as determined by irregular, spiky element signals and thus, these analyses were excluded from the database. LA-ICP-MS data are summarized in Fig. 10 and all results are reported in Table SM2.

2.4.5. Polycrystalline inclusions in magnetite

Several types of inclusions were identified by using micro-Raman spectroscopy analysis, SEM and LA-ICP-MS data. The inclusions can be oriented or randomly distributed, single or polycrystalline. Actinolite is the most ubiquitous phase, and can be accompanied by quartz and an unspecified Mg-Al-Si-phase. The latter was also reported in Los Colorados (Knipping et al. 2016) and El Romeral (Rojas et al. 2018a) magnetite ores. Inclusions in Type I magnetite grains include Ti-oxides (rutile and ilmenite), clinopyroxene (augite), orthopyroxene (hypersthene-enstatite), amphibole (actinolite-ferroactinolite-pargasite), titanite and chlorite (clinochlore); the latter is related to amphibole/pyroxene alteration. Type IV magnetite grains display randomly distributed inclusions and/or organized in repetitive sinuous arrangements (Fig. 8d). Identified mineral inclusions include: actinolite, quartz, Na-clinopyroxene (aegirine) and Mg-orthopyroxene (hypersthene-enstatite), which correlate with Mg, Al and Si magnetite enrichments (Fig. 9).

2.4.6. Zircon U-Pb dating

Zircons extracted from the diorite intrusion (sample CNN-05) are clear light reddish-brown in color and range from 80 to 250 μm in size showing narrow concentric zoning in CL-imaging. They have U and Th concentrations that vary from 1320-3846 and 765-4750 ppm, respectively yielding U/Th ratios of ~1, characteristic of igneous zircons (Rubatto 2002). Analysis of 20 zircon grains yielded a weighted average age of 129.6 ± 1.0 Ma (MSWD=1.8, n = 21; Fig. 11). No older components were detected. Results for each spot are reported in Table

SM3.

2.4.7. Sulfur isotopic compositions

The $\delta^{34}S$ values of Cerro Negro Norte pyrites, mainly from veinlets corresponding to the hydrothermal mineralization event (Fig. 7), were measured in order to elucidate the source of sulfur. The $\delta^{34}S$ for seven pyrite samples range from -0.5 to +4.3 ‰ (Table SM4) with a mean of +1.1 ‰ and a median of +0.8 ‰. It is noteworthy that no correlation is observed between sample depth and $\delta^{34}S$ values.

2.5. DISCUSSION

2.5.1. Timing and sulfur source

The new U-Pb zircon age (~130 Ma) obtained here for La Brea diorite related to the magnetite mineralization in Cerro Negro Norte constrains the timing of mineralization to the Early Cretaceous. Furthermore, this age is the same within uncertainty as the age obtained for the Carmen (131.0 ± 1.0 Ma; Gelcich et al. 2005) and the El Romeral deposit (129.0 ± 0.9 Ma; Rojas et al. 2018b), where a genetic link between the magnetite ore and the diorite intrusion has been demonstrated. It is apparent from the limited geochronology for IOA deposits in northern Chile that the period around 130 Ma was very fertile for this type of deposit. Furthermore, the new age presented here supports the notion that Andean IOA deposits formed under extensional conditions during the first substage of the Andean I period, also known as the Early Pacific stage (135–120 Ma) (Chen et al. 2013).

The sulfur isotopic signature for pyrites from the Cerro Negro Norte deposit varies within a narrow range from -0.5 to +4.3 ‰ (Table SM4), indicating an exclusively magmatic origin without a sedimentary or bacterial contribution. Delta-34 sulfur values in this deposit are very similar to those reported for El Romeral and other Andean IOA deposits (Fig. 12), which display a restricted range between -5 and +5 ‰. Andean IOCG deposits (e.g., Candelaria, Diego de Almagro) also display narrow range of $\delta^{34}S$ values, except Mantoverde where a possible contribution from a non-magmatic source has been proposed (Benavides et al. 2007).

2.5.2. Discrimination diagrams as a fingerprint of deposit types

Several diagrams that use the trace element composition of magnetite have been proposed to discriminate between different deposit types; i.e., porphyry, BIF, Kiruna, IOCG and Fe-Ti-V deposits (Dupuis and Beaudoin 2011; Nadoll et al. 2014; Meng et al. 2017) or to differentiate between a hydrothermal or magmatic origin (Nadoll et al. 2015; Dare et al. 2014; Knipping et al. 2015a,b; Wen et al. 2017). Recent studies from Chilean IOA deposits, e.g., El Laco (Dupuis and Beaudoin 2011; Broughm et al. 2017), Los Colorados (Knipping et al. 2015a,b; Deditius et al., 2018), and El Romeral (Rojas et al. 2018a), show that analyzed magnetite grains plot over all deposit-type fields in an (Ti+V) vs. (Al+Mn) diagram. In Cerro Negro Norte, inclusion-rich magnetite cores (Type I) have the highest trace element content (Ti+V: 0.14-0.50 wt%; Al+Mn: 0.05-0.44 wt%), followed by inclusion-free magnetite rims (Type II). The latter shows a more widespread compositional distribution with occasional spots with a higher (Ti+V) and (Al+Mn) content than Type I magnetite (Fig. 13). Inclusion-free magnetite grains (Type III) have a variable concentration of Al, Mn, Ti and V, with a high Al+Mn (up to 0.35 wt%) and Ti content (up to 0.27 wt%) and moderately high V concentrations

(~0.1 wt%). Most analyses from Type III magnetite plot in the IOCG field, whereas Type IV magnetites plot in or near the BIF field, displaying the lowest trace element content (Fig. 13). In summary, most of the EPMA analyses of Cerro Negro Norte magnetite grains plot between the IOCG, Porphyry and Kiruna fields, and some plot even below the Kiruna field. Based on the work by Nadoll et al. (2014), Knipping et al. (2015a) showed that the chemical composition of the different magnetite types identified in Los Colorados reflect a cooling trend from high-T magmatic (the Fe-Ti, V field) to high-T hydrothermal conditions (the porphyry and Kiruna fields). No cooling trend is observed for Cerro Negro Norte magnetites in the (Ti+V) vs (Al+Mn) plot as seen for Los Colorados; however, the widespread distribution of Types I, II and III magnetite analyses (Fig. 13), could reflect a high-temperature formation (>500 ºC), whereas Type IV magnetite vein mineralization represents a lower temperature event (300-500 ºC). Thus, our data support the notion that the magnetite composition plotted in the (Al+Mn) vs. (Ti+V) diagram reflects the temperature of formation, as previously suggested by Nadoll et al. (2014). It follows that the magnetite ore in each Chilean IOA deposit (e.g., Los Colorados, El Romeral, El Laco, and Cerro Negro Norte) is the result of different events, and that the trace element incorporated or remobilized from the magnetite grains reflect a strong temperature control.

2.5.3. Magmatic vs hydrothermal magnetite

The trace element composition obtained by LA-ICP-MS was normalized to the bulk continental crust and then compared to magnetite data from different environments (Dare et al. 2014), in order to evaluate the magmatic and/or hydrothermal processes that may have occurred in the Cerro Negro Norte deposit (Fig. 14). The results of our study were compared to magmatic magnetite from Fe-Ti-P/V deposits, high- and low-T hydrothermal magnetite and to Kiruna-type deposit from the Los Colorados deposit in the Chilean Iron Belt (Knipping et al. 2015a,b). All magnetite grains show very similar patterns except for Type III magnetite with positive Hf, P, Ti, and Ni anomalies.

Another diagram used to discriminate igneous from hydrothermal magnetite in porphyry system was proposed by Nadoll et al. (2015) by comparing the V and Ti concentrations (Fig. 15), owing to the observation that igneous magnetite is ubiquitously enriched in these lithophile elements when compared to hydrothermal magnetite. The Cerro Negro Norte magnetite contains 8-2269 ppm V and 8.2-2850 ppm Ti (Fig. 10; Table SM2), both consistent with the global range of igneous and hydrothermal magnetite (15-6600 ppm V, <15-3560 ppm Ti; Nadoll et al. 2015). In general, Type I, II and III magnetite grains plot in the overlapping area between the magmatic and hydrothermal fields, whereas Type IV plot exclusively in the hydrothermal area, with four samples showing a V content consistent with hydrothermal magnetite, but with lower Ti concentrations (Fig. 15).

Recently, Wen et al. (2017) proposed a new discrimination diagram based on the Fe content and the V/Ti ratio (Fig. 16). This diagram is sustained on the fact that generally the V/Ti ratio in igneous magnetite is <1 and >1 in hydrothermal magnetite, whereas the Fe content tends to decrease in magmatic (<66 wt% Fe) relative to hydrothermal magnetite because of differential incorporation of trace elements in the magnetite structure. By plotting our results in this diagram with data from other Andean Kiruna-type deposits such as El Laco (Broughm et al. 2017), Los Colorados (Knipping et al. 2015b) and El Romeral (Rojas et al. 2018a), and analyses for igneous, high-T and low-T hydrothermal magnetite (Nadoll 2011; Nadoll et al. 2014, 2015) it is clear that all IOA data points plot within the hydrothermal field and that no reequilibration trend is observed, with the possible exception of Los Colorados (Fig. 16). In particular, Cerro Negro Norte magnetite grains have a relatively constant Fe content (70-72 wt% Fe) and a variable V/Ti ratio, which is lower in Type IV magnetite and higher in Type I and II magnetites. The Ti content among Cerro Negro Norte magnetite grains is variable and ranges between a few tens up to thousands of ppm in all types, except for Type IV, where it can be as low as 10 ppm. On the other hand, V is high in Type I and II magnetite, slightly lower in Type III and significantly lower in Type IV magnetite (Fig. 15). Vanadium is a highly compatible and is usually present in high concentrations and homogeneously distributed in IOA magnetite grains (Knipping et al. 2015a,b; Rojas et al. 2018a). It also appears to be more immobile under hydrothermal alteration and possibly more reliable as a tracer of magnetite origin.

In addition, some authors have hypothesized that the concentration of Sn and Ga can be used to discriminate different types of hydrothermal magnetite (Kamvong et al. 2007) and igneous magnetite (Nadoll et al. 2015). In particular, a high Ga content appears to be an indicator of high-temperature magnetite crystallization (Knipping et al. 2015b) and thus, a good proxy to trace the evolution of Cerro Negro Norte. Figure 17 shows a V vs Ga plot for Cerro Negro Norte, El Laco and Kiruna IOA deposits and magnetite from volcanic rocks in which a general trend from high-T (magmatic) to low-T hydrothermal magnetite is recognized. Here, the Cerro Negro Norte magnetite grains reflect a transition from magmatic-hydrothermal (Types I and II) to medium-T hydrothermal event (Type III) and a low-T hydrothermal magnetite (Type IV). Thus, the magnetite data for the Cerro Negro Norte deposit reflect different conditions and formation processes, leading to significant textural features which can be intimately related to chemical variations at both the macro- and micro-scale. Data from the Kiruna deposits in Sweden and from El Laco in northern Chile (Broughm et al. 2017) are also plotted in Fig. 17. Both El Laco and Kiruna magnetite grains have low Ga and a moderate V content, which is more consistent with a hydrothermal origin, as has been suggested by Dare et al. (2015). The low trace element content in Kiruna magnetite ore samples could also reflect a hydrothermal origin or most likely an overprint by metasomatic processes (Broughm et al. 2017).

2.5.4. Magnetite formation conditions

The data presented in this study reflect the evolution of the Cerro Negro Norte Fe-deposit. The deposit is characterized by several formation processes under different conditions that are expressed in significant textural and chemical variations. At least four events of magnetite mineralization are recognized: an early event with formation of the inclusion-rich magnetite (Type I) followed by precipitation of inclusion-free magnetite (Type II), generally observed as rims, growing over primary magnetite. The chemical differences between both types are mainly in the Al, Ti and Mn contents, which decrease in rims (Type II), while V and Ga tend to be relatively constant among these two types. This could be explained by precipitation of high-temperature hydrothermal magnetite over Type I magnetite as seen in Los Colorados and El Romeral (Knipping et al. 2015a,b; Rojas et al. 2018a).

Vanadium incorporation into magnetite is constrained at low oxygen fugacity and high temperature conditions (Toplis and Corgne 2002; Nadoll et al. 2014). In addition, both Ti and Al are also incorporated into magnetite at higher temperatures and considered immobile at submagmatic temperatures (Van Baalen 1993; Nadoll et al. 2014). It appears then that magnetite Types I and II were precipitated at high temperatures during transition from magmatic to hydrothermal conditions (>500 ºC) and at low oxygen fugacity conditions, whereas the low V content in Type IV magnetite could reflect precipitation by a lower temperature (i.e., 300-500 ºC) and more oxidized hydrothermal fluid.

Mineral inclusions present in Type I magnetite grains can provide further insights about formation temperature of primary magnetite if we assume that those phases crystallized simultaneously with Type I magnetite. As a result of differing nucleation and growth rates, these mineral phases would be randomly incorporated within the magnetite host crystals. Several inclusions were identified in Type I magnetite grains such as rutile, ilmenite, clino- and orthopyroxene, actinolite, pargasite, titanite, and clinochlore. At 200 MPa, pargasite stability is estimated between ~800 °C and ~1020 °C (Jenkins 1983), whereas clinochlore breaks down at ~780 °C (Staudigel and Schreyer 1977). Hence, the formation temperature for Type I magnetite can be constrained between ~800 to 1020 ºC, a range that was also defined for “magmatic” magnetites from El Romeral (Rojas et al. 2018a). The presence of abundant inclusions in magnetite grain cores has also been described for the Los Colorados (Knipping et al. 2015a,b) where the cited authors have interpreted these inclusion-rich magnetite cores as a common feature of primary magmatic magnetite.

On the other hand, Type III and IV magnetite grains seems to represent distinct hydrothermal pulses at different temperatures that are roughly evidenced by chemical and textural features as the V and Ga content as well as chemical zonation in magnetite (Type III) and sinuous oscillatory inclusion arrangements in Type IV magnetite.

In addition, sulfur isotopic compositions for two chalcopyrite-pyrite pairs, belonging to the latter mineralization event, were reported by Raab (2001), who calculated a depositional temperature of ~590 °C, being relatable with vein generation of Type IV magnetite.

2.5.5. Cerro Negro Norte: an IOCG link?

The Compañía Minera del Pacífico (CMP), through studies in the 1980s, recognized the economic potential for the copper and gold reserves at Cerro Negro Norte, allocating an estimated total reserves of 550,000 tons with 1.45 g/ton gold and 0.24 % Cu. In general, the areas of interest are usually found along late or reactivated fault zones with NNE orientation and/or contacts between the andesites and diorites (Vivallo et al. 1995b).

Three of these Cu-Au rich zones are located west of the Abanderada area, where abundant quartz + carbonates ± Cu sulfide veinlets are present (Raab 2001; Vivallo et al. 1995b). A fourth zone of interest, towards the north of the same area, is related to andesites altered to chlorite + calcite + quartz + tourmaline. In the Augusta area (Fig. 3) it is also possible to find Cu-Au mineralization, which is associated mainly with quartz + tourmaline + sericite altered breccias with sulfide mineralization.

Vivallo et al. (1995b) concluded that higher gold grades (up to 1 ppm) are associated with pyrite mineralization, whereas Au in magnetite is usually less than 100 ppb. These authors suggested a late hydrothermal remobilization of Au from the iron ore of magmatic origin, with the consequent redistribution of gold associated with increased sulfur fugacity in the system. On the other hand, Raab (2001) suggested that the Cu-Au mineralization is predominantly associated with late pyrite ± chalcopyrite veinlets and the tourmaline-quartz alteration. In addition, the abundance of Cu sulfides (mainly chalcopyrite) increases from Type III to Type IV magnetite-related events, reaching up to a 1:1 pyrite-chalcopyrite ratio in some samples, which could reflect an increase in the Cu content of the hydrothermal fluids.

Based on our observations, the increasing sulfide content from Stage I to Stage II is consistent with the IOA flotation model (Knipping et al. 2015a,b; Reich et al. 2016) where the magmatic-hydrothermal fluid can transport and later precipitate magnetite and other metals (i.e., Cu, Au). The sulfides and Au related to the quartz-tourmaline alteration (Stage III; Fig. 7) are possibly associated with a later magmatic event and not to the main IOA formation.

2.6. CONCLUSIONS

The Cerro Negro Norte deposit is hosted in Cretaceous volcanic rocks from the Bandurrias Formation and is spatially and genetically related to La Brea diorite intrusion. Uranium-Pb zircon dating of this intrusion yielded a 129.6 ± 1.0 Ma age, which is consistent with other IOAs in the Chilean Iron Belt (i.e., El Romeral, Carmen). The deposit was formed by an early magmatic episode with magnetite and actinolite followed by the main hydrothermal event, which includes precipitation of hydrothermal magnetite and sulfides. The $\delta^{34}S$ values obtained for pyrite from the Cerro Negro Norte deposit vary between -0.5 and +4.3 ‰, indicating an exclusively magmatic origin for the sulfur in this deposit. This finding is consistent with the sulfur isotopic signature for El Romeral and other Andean IOA and IOCG deposits.

Mineralogical observations combined with microanalytical techniques, i.e., LA-ICP-MS analysis, EPMA, and SEM data, reveal four main magnetite types in Cerro Negro Norte: (i) magnetite mineralization (Type I) represented by high-temperature, magnetite cores with mainly amphiboles, pyroxene and some oxide inclusions; (ii) inclusion-free magnetite (Type II), usually surrounding primary magnetite cores; (iii) Type III magnetite generally inclusion-free and sometimes with few inclusions, oscillatory and chemical zoning; and, (iv), magnetite veinlets (Type IV) with sinuous oscillatory inclusion arrangements. The magnetite grains show a variable concentration of trace elements that reflect their formation temperature. Based on the chemical characteristics of the magnetite types, a new discrimination diagram based on the V and Ga contents is proposed to identify magmatic and/or hydrothermal events.

The data presented here for the Cerro Negro Norte deposit are consistent with the flotation model as proposed for Los Colorados (Knipping et al. 2015a,b) and supported by further evidence from the El Romeral Fe-deposit (Rojas et al. 2018a,b). The use of discrimination diagrams (Dupuis and Beaduin 2011; Dare et al. 2014; Knipping et al. 2015a; Wen et al. 2017) should be coupled with detailed petrographic and textural studies in order to characterize superimposed metasomatic events that can modify the trace element signature of magnetite (Deditius et al. 2018). In our case study, it is the V vs Ga plot that better represents the four Fe mineralization events recognized in the Cerro Negro Norte deposit.

ACKNOWLEDGEMENTS

This work was funded by FONDECYT grant #1140780 to F. Barra and the Millennium Science Initiative (MSI) through Millennium Nucleus for Metal Tracing along Subduction grant NC130065. The LA-ICP-MS analytical work was supported by CONICYT-Fondequip instrumentation grant EQM120098. We are grateful to Carlos Garrido and Rudencindo Clavijo, from the Chemistry Department of the Universidad de Chile, for their help with the micro-Raman analyses, Victor Valencia for zircon mineral separation at Zirchron LLCC, and Dave Dettman for sulfur isotope analyses at the University of Arizona. We thank the Compañía Minera del Pacífico (CMP) and their geology team for their helpful logistical support, and for providing access to the mine and drill cores.

REFERENCES

Aguirre L (1985) The Southern Andes. In: Nairn AEM, Stehli FG, Uyeda S (eds) The Ocean Basins and Margins. Springer, Boston, MA, pp. 265-376

Arevalo C (2005) Mapa Geológico Hoja Copiapó, Región de Atacama, escala 100,000. Servicio Nacional de Geología y Minería

Amilibia A, Sabat F, McClay KR, Muñoz J, Chong G (2008) The role of inherited tectono-sedimentary architecture in the development of the central Andean mountain belt: Insights from the Cordillera de Domeyko. J Struct Geol 30:1520-1539

Barra F, Reich M, Selby D, Rojas P, Simon A, Salazar E, Palma G (2017) Unraveling the origin of the Andean IOCG clan: A Re-Os isotope approach. Ore Geol Rev 81:62-78

Barton MD (2014) Iron Oxide (-Cu-Au-REE-P-Ag-U-Co) Systems. In: Holland H and Turkian K (eds) Treatise in Geochemistry 2nd Edition 13:515–541

Benavides J, Kyser TK, Clark AH, Oates CJ, Zamora R, Tarnovschi R, Castillo B (2007) The Mantoverde iron oxide-copper-gold district, III Región, Chile: the role of regionally derived, nonmagmatic fluids in chalcopyrite mineralization. Econ Geol 102:415–440

Bilenker LD, Simon AC, Reich M, Lundstrom CC, Gajos N, Bindeman I, Barra F, Munizaga R (2016) Fe-O stable isotope pairs elucidate a high-temperature origin of Chilean iron oxide-apatite deposits. Geochim Cosmochim Acta 177:94–104

Black LP, Kamo SL, Allen CM, Davis DW, Aleinikoff JN, Valley JW, Mundil R, Campbell IH, Korsch RJ, Williams IS, Foudoulis C (2004) Improved Pb-206/U-218 microprobe geochronology by the monitoring of a trace-element-related matrix effect; SHRIMP, IDTIMS, ELA-ICP-MS and oxygen isotope documentation for a series of zircon standards. Chem Geol 205:115–140

Bookstrom A (1977) The magnetite deposits of El Romeral, Chile. Econ Geol 72:1101–1130

Broughm SG, Hanchar JM, Tornos F, Westhues A, Attersley S (2017) Mineral chemistry of magnetite from magnetite-apatite mineralization and their host rocks: examples from Kiruna, Sweden, and El Laco, Chile. Miner Deposita 52:1223-1244

Brown M, Díaz F, Grocott J (1993) Displacement history of the Atacama Fault System, 25°00′S 27°00′S, northern Chile. Geol Soc Am Bull 105:1165–1174

Cembrano J, González G, Arancibia G, Olivares V, Herrera V (2005) Fault zone development and strain partitioning in an extensional strike-slip duplex: A case study from the Mesozoic Atacama Fault System, Northern Chile. Tectonophysics 400:105-125

Chen H, Cooke DR, Baker MJ (2013) Mesozoic iron oxide copper-gold mineralization in the Central Andes and the Gondwana supercontinent breakup. Econ Geol 108:37–44

Coleman ML, Moore MP (1978) Direct reduction of sulfates to sulfur dioxide for isotopic analysis. Anal Chem 50:1594-1595

Dare SAS, Barnes S-J, Beaudoin G, Méric J, Boutroy E, Potvin-Doucet C (2014) Trace elements in magnetite as petrogenetic indicators. Miner Deposita 49:785–796

Dare SAS, Barnes S-J, Beaudoin G (2015) Did the massive magnetite "lava flows" of El Laco (Chile) form by magmatic or hydrothermal processes? New constraints from magnetite composition by LA-ICP-MS. Miner Deposita 50:607-617

Deditius AP, Reich M, Simon AC, Suvorova A, Knipping J, Roberts MP, Rubanov S, Dodd A, Sauders M (2018) Nanogeochemistry of hydrothermal magnetite. Contrib Miner Petrol 173:46 https://doi.org/10.1007/s00410-018-1474-1

Dupuis C, Beaudoin G (2011) Discriminant diagrams for iron oxide trace element fingerprinting of mineral deposit types. Mineral Deposita 46:319–335

Espinoza S (1990) The Atacama-Coquimbo ferriferous belt, northern Chile. In: Fontboté L, Amstutz GC, Cardozo M, Cedillo E, Frutos J (eds) Stratabound ore deposits in the Andes. Berlin,Springer-Verlag, 353-364

Gelcich S, Davis DW, Spooner ETC (2005) Testing the apatite-magnetite geochronometer: U-Pb and $^{40}Ar/^{39}Ar$ geochronology of plutonic rocks, massive magnetite-apatite tabular bodies, and IOCG mineralization in Northern Chile. Geochim Cosmochim Acta 69:3367–3384

Grocott J, Taylor GK (2002) Magmatic arc fault systems, deformation partitioning and emplacement of granitic complexes in the Coastal Cordillera, north Chilean Andes (25°30'S to 27°00'S). J Geol Soc 159:425-443

Jenkins DM (1983) Stability and composition relations of calcic amphiboles in ultramafic rocks. Contrib Mineral Petrol 83:375–384

Kamvong T, Zaw K, Siegele R (2007) PIXE/PIGE microanalysis of trace elements in hydrothermal magnetite and exploration significance: a pilot study. 15th Australian Conference on Nuclear and Complementary Techniques of Analysis and 9th Vacuum Society of Australia Congress. University of Melbourne, Melbourne, Australia

Knipping JL, Bilenker LD, Simon AC, Reich M, Barra F, Deditius AP, Lundstrom C, Bindeman I, Munizaga R (2015a) Giant Kiruna-type deposits form by efficient flotation of magmatic magnetite suspensions. Geology 43:591-594

Knipping JL, Bilenker LD, Simon AC, Reich M, Barra F, Deditius AP, Wälle M, Heinrich CA, Holtz F, Munizaga R (2015b) Trace elements in magnetite from massive iron oxide-apatite deposits indicate a combined formation by igneous and magmatic-hydrothermal processes. Geochim Cosmochim Acta 171:15-38

Laetsch T, Downs T (2006) Software for identification and refinement of cell parameters from powder diffraction data of minerals using the RRUFF project and American Mineralogist Crystal Structure databases. Abstracts from the 19th General Meeting of the International Mineralogical Association, Kobe, Japan, 2006

Lara L, Godoy E (1998) Hoja Quebrada Salitrosa, Región de Atacama. Servicio Nacional de Geologia y Mineria (SERNAGEOMIN), Mapas Geológicos, 1:100,000 scale, No. 4

Loberg BEH, Horndahl A-K (1983) Ferride geochemistry of Swedish Precambrian iron ores. Mineral Deposita 18:487–504

Longerich HP, Jackson SE, Günther D (1996) Laser ablation inductively coupled plasma mass spectrometric transient signal data acquisition and analyte concentration calculation. J Anal At Spectrom 11:899-904.

Loyola N (2016) Origen de la mineralización y alteración hidrotermal del depósito tipo IOCG Diego de Almagro, III Región de Atacama, Chile. Honours thesis, Universidad de Chile, Santiago, Chile, 130 pp.

Ludwig K (2010) Isoplot/Ex version 4.1, a geochronological toolkit for Microsoft Excel: Berkeley Geochronology Center, Special Publication No. 4

Marschik R, Fontboté L (2001) The Candelaria-Punta del Cobre iron oxide Cu-Au(-Zn-Ag) deposits, Chile. Econ Geol 96:1799–1826

McInnes BIA, Keays RR, Lambert DD, Hellstrom J, Allwood JS (2008) Re–Os geochronology and isotope systematics of the Tanami, Tennant Creek and Olympic Dam Cu–Au deposits. Aust J Earth Sci 55:967–981

Ménard J (1995) Relationship between altered pyroxene diorite and the magnetite mineralization in the Chilean Iron Belt, with emphasis on the El Algarrobo iron deposits (Atacama region, Chile). Miner Deposita 30:268–274

Meng Y, Hu R, Huang X, Gao J (2017) Germanium in magnetite: A preliminary review. Acta Geol Sinica 91:711-726

Mpodozis C, Ramos VA (1990) The Andes of Chile and Argentina. In: Ericksen E, Cañas Pinochet T, Reinemund A (eds) Geology of the Andes and its Relation to Hydrocarbon and Mineral Resources. Circum-Pacific Council for Energy and Mineral Resources, Earth Science Series 11:59–90

Nadoll P (2011) Geochemistry of magnetite from hydrothermal ore deposits and host rocks – Case studies from the Proterozoic Belt Supergroup, Cu-Mo-porphyry + skarn and Climax-Mo deposits in the western United States. PhD thesis, The University of Auckland, 313 p

Nadoll P, Koenig AE (2011) LA-ICP-MS of magnetite: methods and reference materials. J Anal At Spectrom 26:1872-1877

Nadoll P, Angerer T, Mauk JL, French D, Walshe J (2014) The chemistry of hydrothermal magnetite: a review. Ore Geol Rev 61:1-32

Nadoll P, Mauk JL, Richard AL, Koenig AE (2015) Geochemistry of magnetite from porphyry Cu and skarn deposits in the southwestern United States. Miner Deposita 50:493-515

Nyström JO, Henríquez F (1994) Magmatic features of iron ores of the Kiruna type in Chile and Sweden: Ore textures and magnetite geochemistry. Econ Geol 89:820-839

Paton C, Hellstrom J, Paul B, Woodhead J, Hergt J (2011) Iolite: Freeware for the visualisation and processing of mass spectrometric data. J Anal At Spectrom 26:2508-2518

Raab A (2001) Geology of the Cerro Negro Norte Fe-Oxide (Cu-Au) District, Coastal Cordillera, northern Chile. Msc thesis, Oregon State University, 273 p

Reich M, Simon AC, Deditius A, Barra F, Chryssoulis S, Lagas G, Tardani D, Knipping J, Bilenker L, Sánchez-Alfaro P, Roberts MP, Munizaga R (2016) Trace element signature of pyrite from the Los Colorados Iron oxide-apatite (IOA) deposit, Chile: a missing link between Andean IOA and iron oxide copper-gold systems. Econ Geol 111:743-761

Rieger AA, Marschik R, Díaz M, Hölzl S, Charadia M, Akker B, Spangenberg JE (2010) The hypogene iron oxide copper-gold mineralization in the Mantoverde district, northern Chile. Econ Geol 105:1271–1299

Rojas P, Barra F, Deditius A, Reich M, Simon A, Roberts M, Rojo M (2018a) New contributions to the understanding of Kiruna-type iron oxide-apatite deposits revealed by magnetite ore and gangue mineral geochemistry at the El Romeral deposit, Chile. Ore Geol Rev 93:413-435

Rojas P, Barra F, Reich M, Deditius A, Simon A, Uribe F, Romero R, Rojo M (2018b) A genetic link between magnetite mineralization and diorite intrusion at the El Romeral iron oxide-apatite deposit, northern Chile. Miner Deposita. https://doi.org/10.1007/s00126-017-0777-x

Rubatto D (2002) Zircon trace element geochemistry; partitioning with garnet and the link between U-Pb ages and metamorphism. Chem Geol 184:123-138

Ruíz FC, Corvalán J, Klohn C, Klohn E, Levi B (1965) Geología y yacimientos metalíferos de Chile. Instituto de Investigaciones Geológicas, Santiago 305 pp

Scheuber E, Andriessen PAM (1990) The kinematic and geodynamic significance of the Atacama Fault Zone, northern Chile. J Struct Geol 12:243-257

Scheuber E, Gonzalez G (1999) Tectonics of the Jurassic-Early Cretaceous magmatic arc of the north Chilean Coastal Cordillera (22°S - 26°S): A story of crustal deformation along a convergent plate boundary. Tectonics 18:895-910

Scheuber E, Hammerschmidt K, Fiedrichsen H (1995) $^{40}Ar/^{39}Ar$ and Rb-Sr analyses from ductile shear zones from the Atacama Fault Zone, northern Chile: the age of deformation. Tectonophysics 250:61-87

Segerstrom K (1968) Geología de las hojas Copiapó y Ojos del Salado, Provincia de Atacama. Instituto de Investigaciones Geológicas, Boletín No. 24, 58 p

Sillitoe RH, Burrows DR (2002) New field evidence bearing on the origin of the El Laco magnetite deposit, northern Chile. Econ Geol 97:1101-1109

Sillitoe RH (2003) Iron oxide-copper-gold deposits: an Andean view. Miner Deposita 38:787-812

Sláma J, Košler J, Condon D, Crowley J, Gerdes A, Hanchar J, Horstwood M, Morris G, Nasdala L, Norberg N, Schaltegger U, Schoene B, Tubrett M, Whitehouse M (2008) Plešovice zircon — A new natural reference material for U–Pb and Hf isotopic microanalysis. Chem Geol 249:1-35

Staudigel H, Schreyer W (1977) Upper thermal stability of clinochlore at PH_2O = 10-35 kb. Contrib Mineral Petrol 61:187-198

Toplis MJ, Corgne A (2002) An experimental study of element partitioning between magnetite, clinopyroxene and iron-bearing silicate liquids with particular emphasis on vanadium. Contrib Mineral Petrol 144:22-37.

Van Baalen MR (1993) Titanium mobility in metamorphic systems: a review. Chem Geol 110:233–249

Vivallo W, Henríquez F, Espinoza S (1995a) Metasomatismo y alteración hidrotermal en el distrito ferrífero Cerro Negro Norte, Copiapó, Chile. Rev Geol de Chile 22:75-88

Vivallo W, Espinoza S, Henríquez F (1995b) Los depósitos de hierro del tipo magnetita-apatita: geoquímica de las rocas volcánicas asociadas y potencialidad de la mena de hierro como fuente de mineralización de oro. Rev Geol de Chile 22:159-175

Wen G, Li JW, Hofstra A, Koenig AE, Lowers HA, Adams D (2017) Hydrothermal reequilibration of igneous magnetite in altered granitic plutons and its implications for magnetite classification schemes: Insights from the Handan-Xingtai iron district, North China Craton. Geochim Cosmochim Acta 213:255-270

Williams PJ, Barton MD, Johnson DA, Fontboté L, De Haller A, Mark G, Oliver NHS, Marschik R (2005) Iron oxide copper-gold deposits: Geology, space-time distribution, and possible modes of origin. In: Hedenquist JW, Thompson JFH, Goldfard RJ, Richards JP (eds) Economic Geology 100th Anniversary Volume. Society of Economic Geologists, Littleton CO, pp. 371–405

Zhimin Z, Yali S (2013) Direct Re-Os dating of chalcopyrite from the Lala IOCG deposit in the Kangdian copper belt, China. Econ Geol 108:871–882

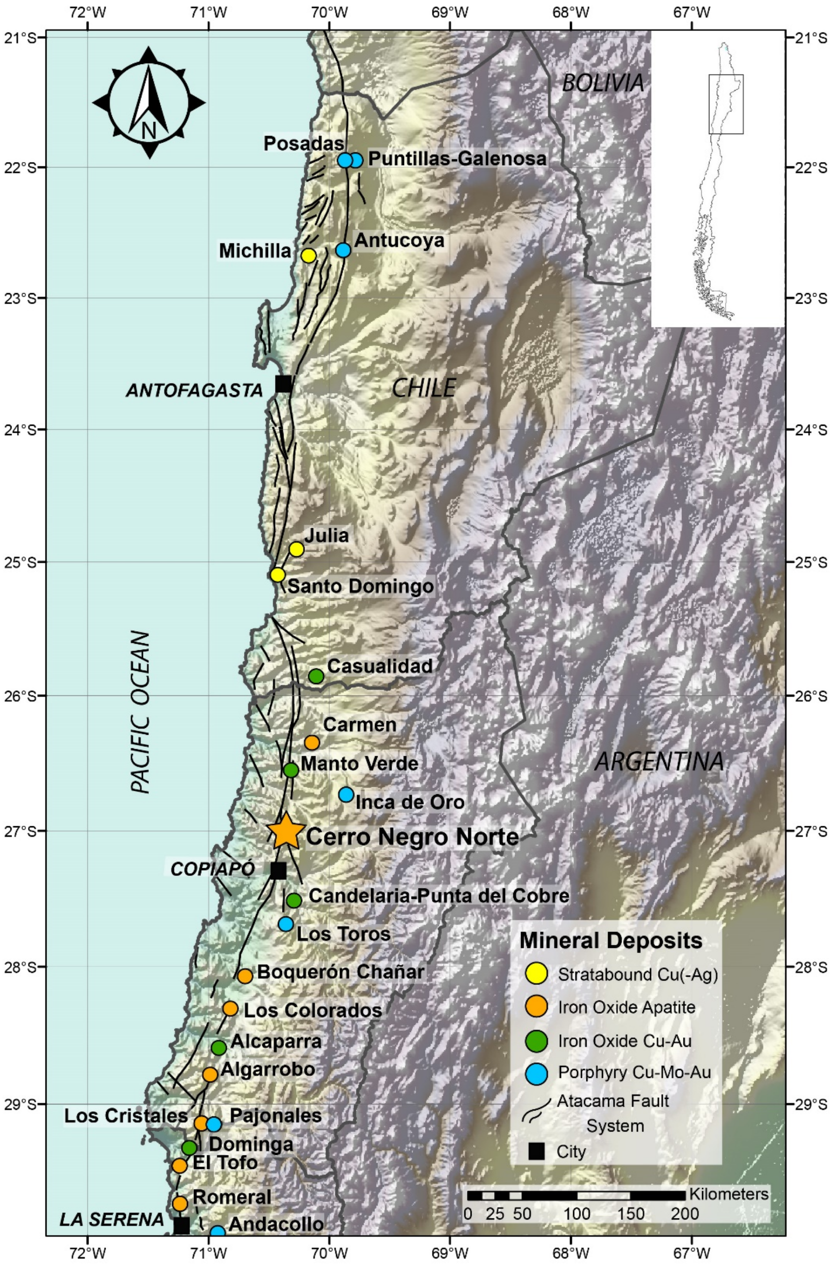

Fig. 1. Map showing the location of the Cerro Negro Norte IOA deposit within the Coastal Cordillera of northern Chile. Other ore deposits from the Cretaceous metallogenetic belt are also shown.

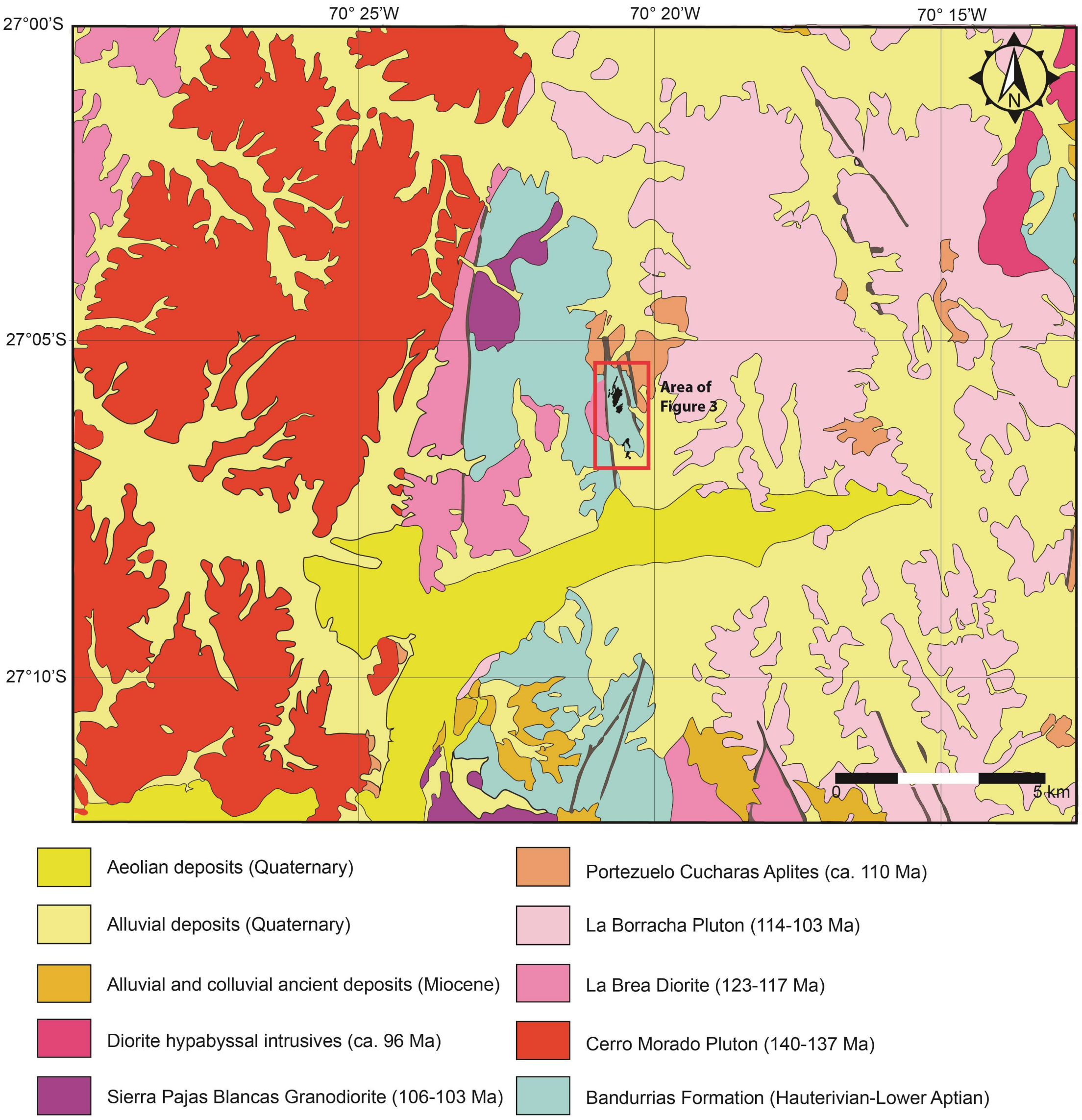

Fig. 2. Geology of the Cerro Negro Norte district. Modified from Arévalo (2005).

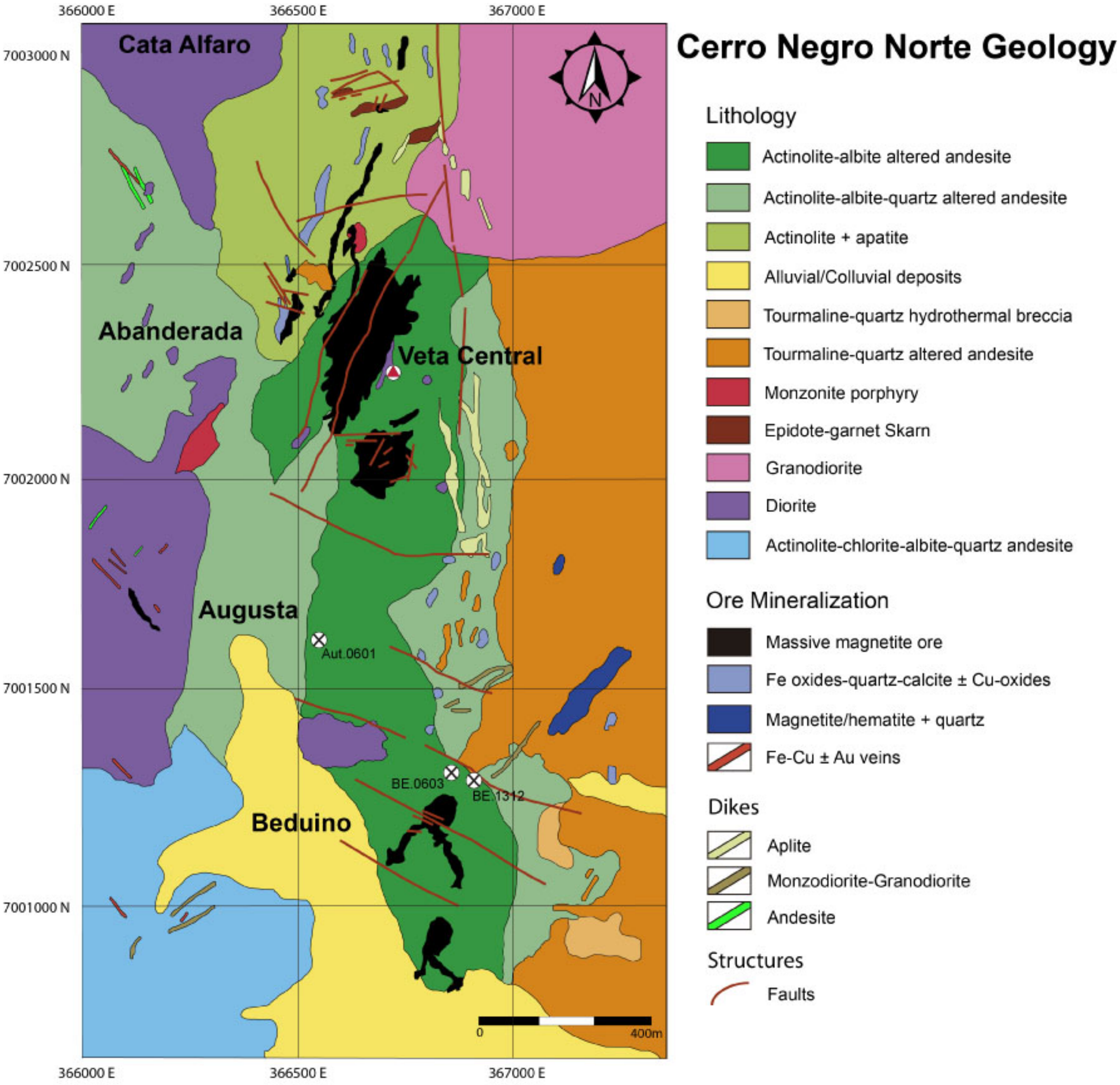

Fig. 3. Geologic map of Cerro Negro Norte deposit. Modified from CMP unpublished map.

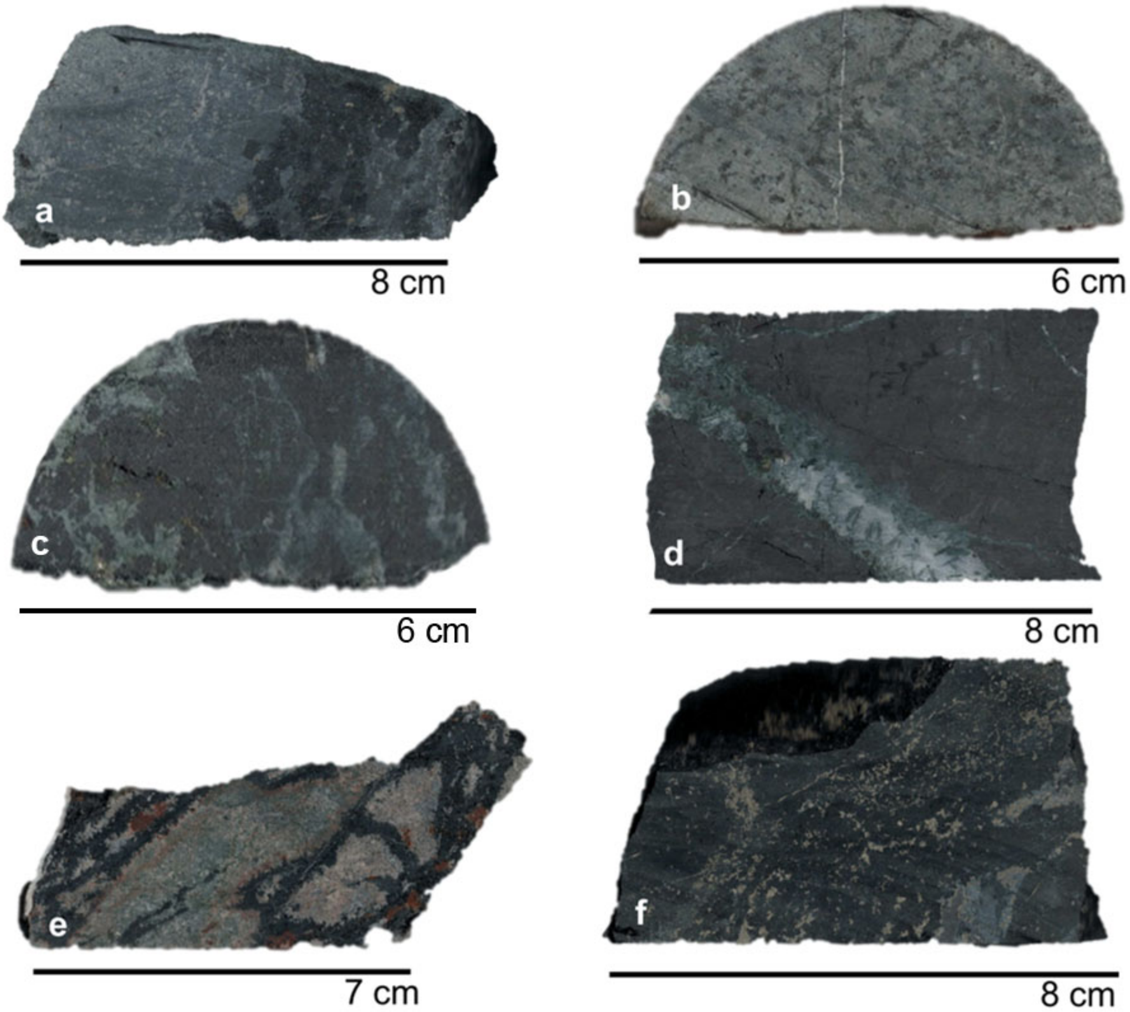

Fig. 4. Representative rock samples from the Cerro Negro Norte deposit. (a) Andesite host rock crosscut by a magnetite vein; (b) Diorite intrusion; (c) Magnetite intergrown with actinolite (dark green); (d) Massive magnetite crosscut by a quartz-actinolite vein; (e) Tourmaline breccias; and (f) massive magnetite with disseminated chalcopyrite grains.

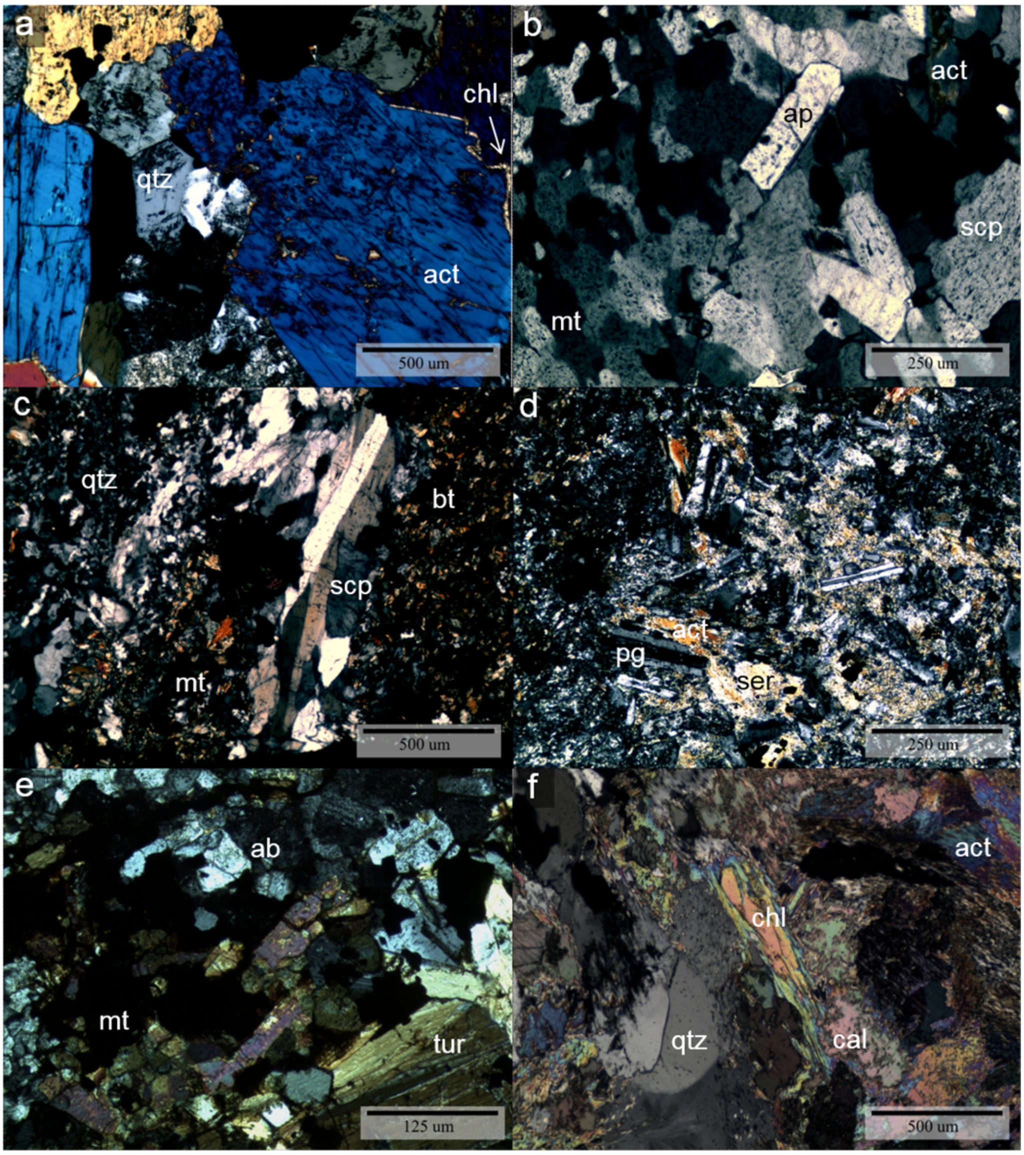

Fig. 5. Cross polarized photomicrographs of different alteration types at Cerro Negro Norte. (a) Elongated prismatic actinolite (act) crystals with quartz (qtz) and chlorite (chl). (b) Tabular aggregates of euhedral apatite (ap) and subhedral scapolite (scp) with magnetite (mt) and actinolite (act). (c) Tabular aggregates of scapolite (scp) with fine-grained biotite (bt) and magnetite (mt). (d) Fibrous actinolite (act) crystals intergrowth with plagioclase (pg) and sericite (ser). (e) Tourmaline (tur) crystals with albite (ab), quartz and disseminated magnetite (mt). (f) Actinolite (act) replaced by an assemblage of chlorite (chl), calcite (cal) and quartz (qtz).

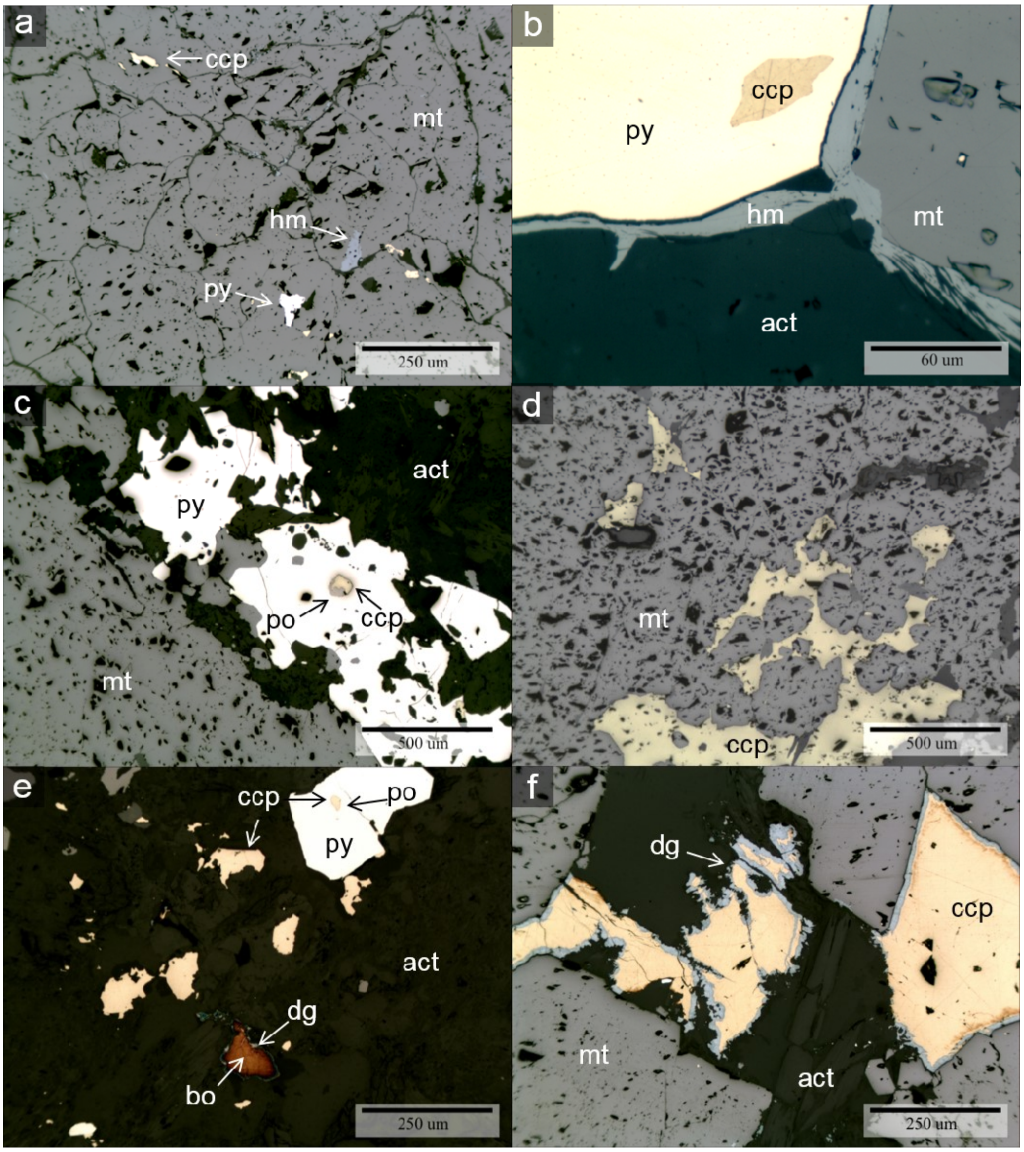

Fig. 6. Reflected light photomicrographs of ore mineralization at Cerro Negro Norte deposit. (a) Granular aggregate of magnetite with pyrite (py), chalcopyrite (ccp) inclusions and hematite (hm) patches. (b) Simple contact between magnetite (mt) and pyrite (py) grains with hematite (hm) along the grain boundaries. Also, chalcopyrite (ccp) is present as an inclusion in pyrite. (c) Anhedral pyrite grain with chalcopyrite (ccp) and pyrrothite (po) inclusions. (d) Chalcopyrite (ccp) filling spaces between magnetite grains. (e) Bornite (bo), chalcopyrite (ccp) and pyrite (py) immersed in an actinolite matrix. Bornite is slightly replaced by digenite (dg), and pyrite (py) shows chalcopyrite (ccp) and pyrrothite (po) inclusions. (f) Chalcopyrite (ccp) in contact with actinolite (act) and magnetite (mt). Digenite (dg) is observed as a incipient replacement of chalcopyrite.

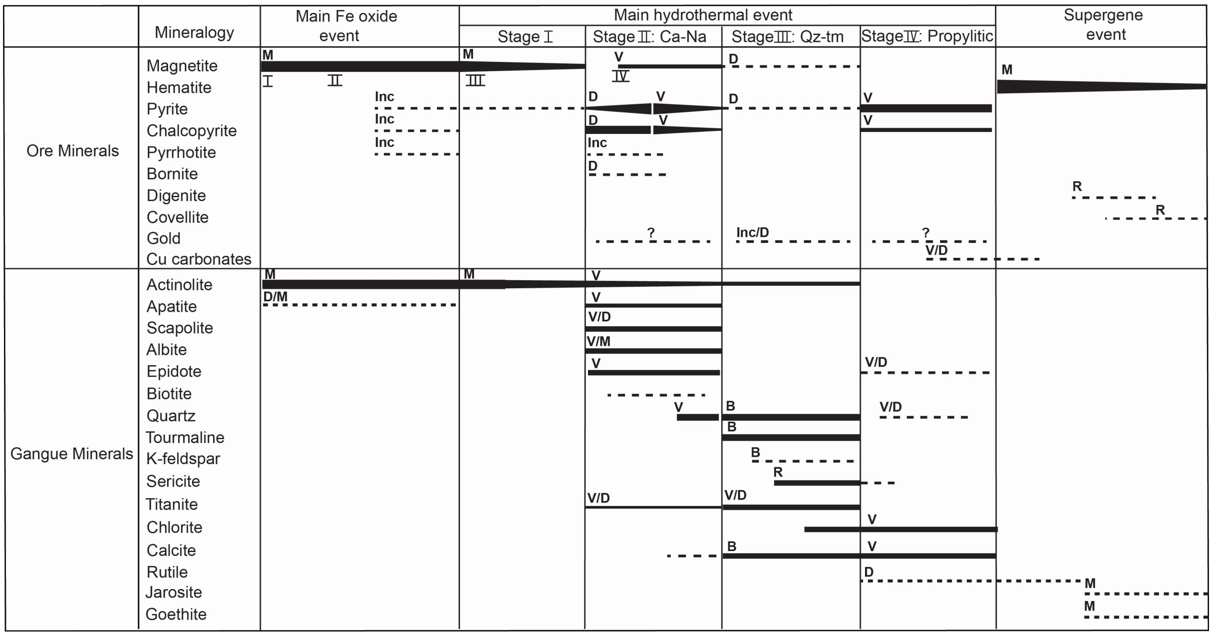

Fig. 7. Paragenetic chart for the Cerro Negro Negro deposit.
Abbreviations: I, II, III and IV: magnetite types; M: massive; D: disseminated; V: veinlets, B: breccias; Inc: inclusion; R: replacement.

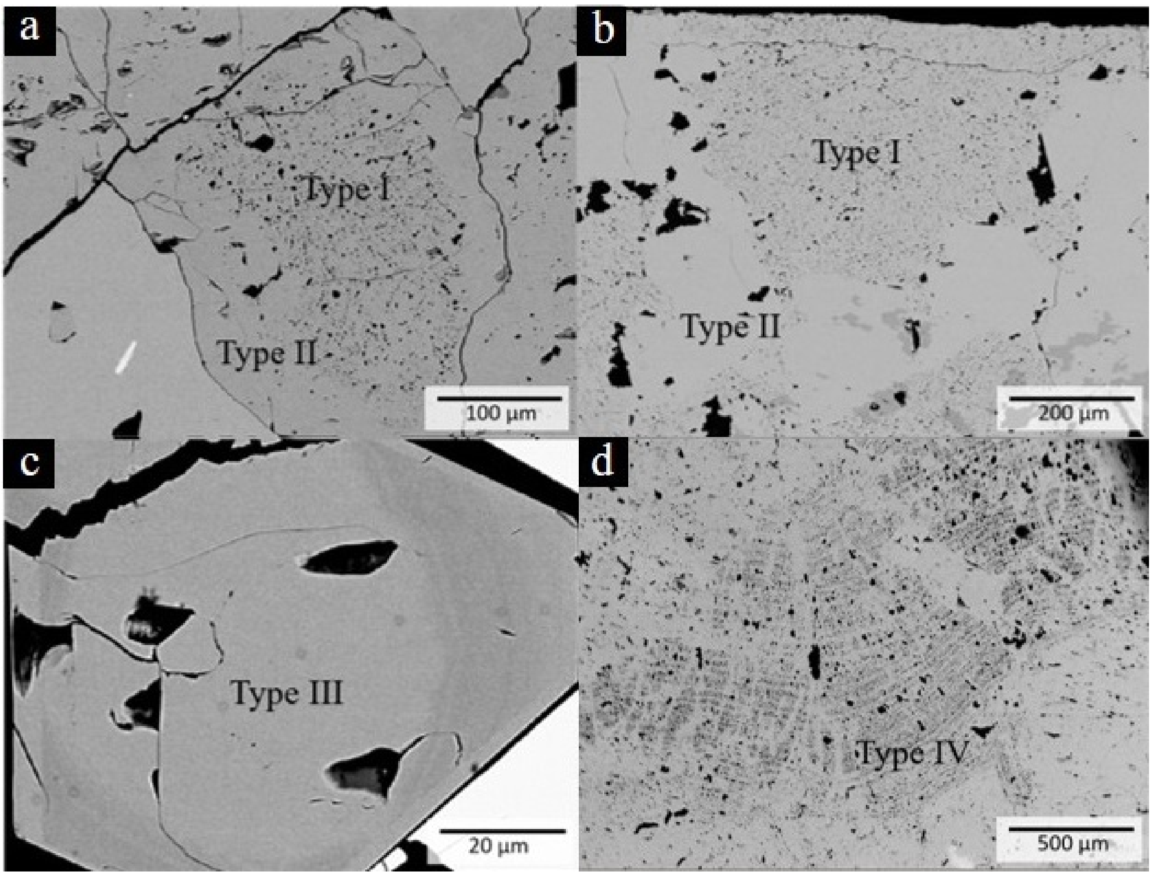

Fig. 8. BSE-images of different magnetite grains. (a) Magnetite grain with randomly distributed inclusions in the core and inclusion-free rim. (b) Magnetite grain with an inclusion-rich core (Type I) and pristine rim (Type II). (c) Euhedral magnetite grain Type III with cryptic zonation towards the edges of the crystal. (d) Oscillatory and sinusoidal inclusion arrangement in magnetite Type IV.

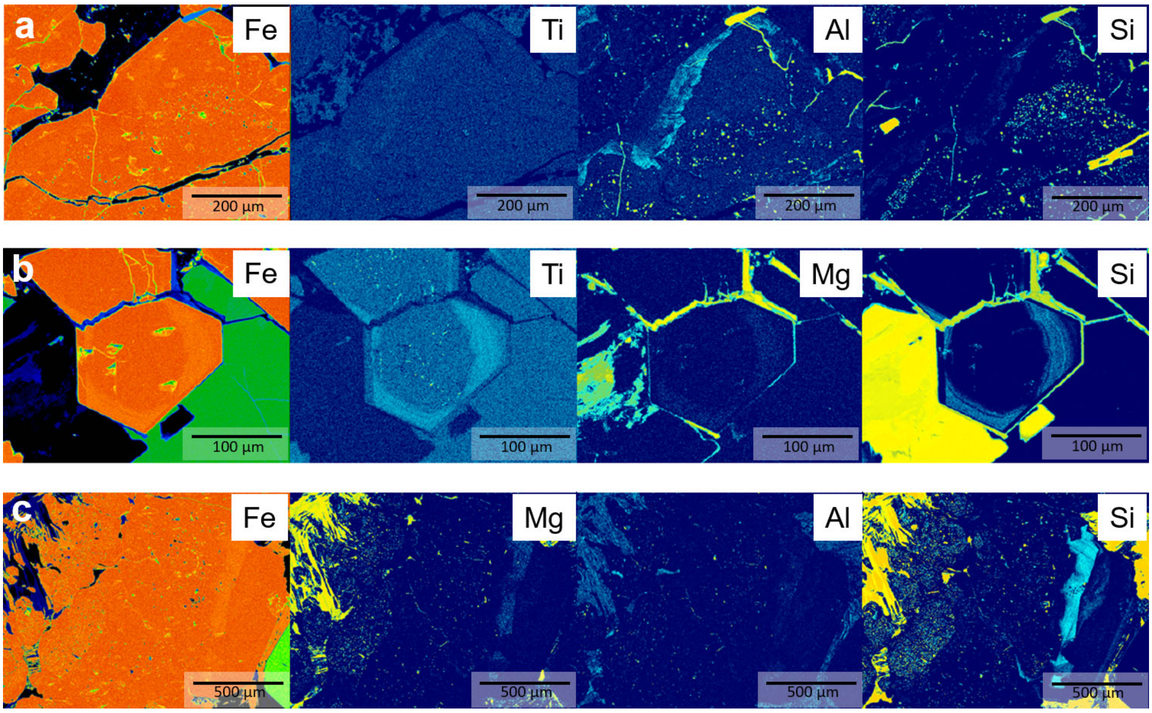

Fig. 9. WDS elemental maps of selected trace elements in each magnetite type. (a) Magnetite grain showing abundant Al-Si inclusions in the core (Type I) surrounded by inclusion-poor magnetite (Type II) that contains Ti-Al- and Si- enrichment zones (sample BEDII3); (b) Inclusion-poor magnetite Type III grain with Ti-Mg and Si- zoning at rims (sample BED09); (c) Type IV magnetite grain in contact with pyrite and actinolite that shows Mg-Al- and Si- zonation. Warmer colors indicate a higher element concentration.

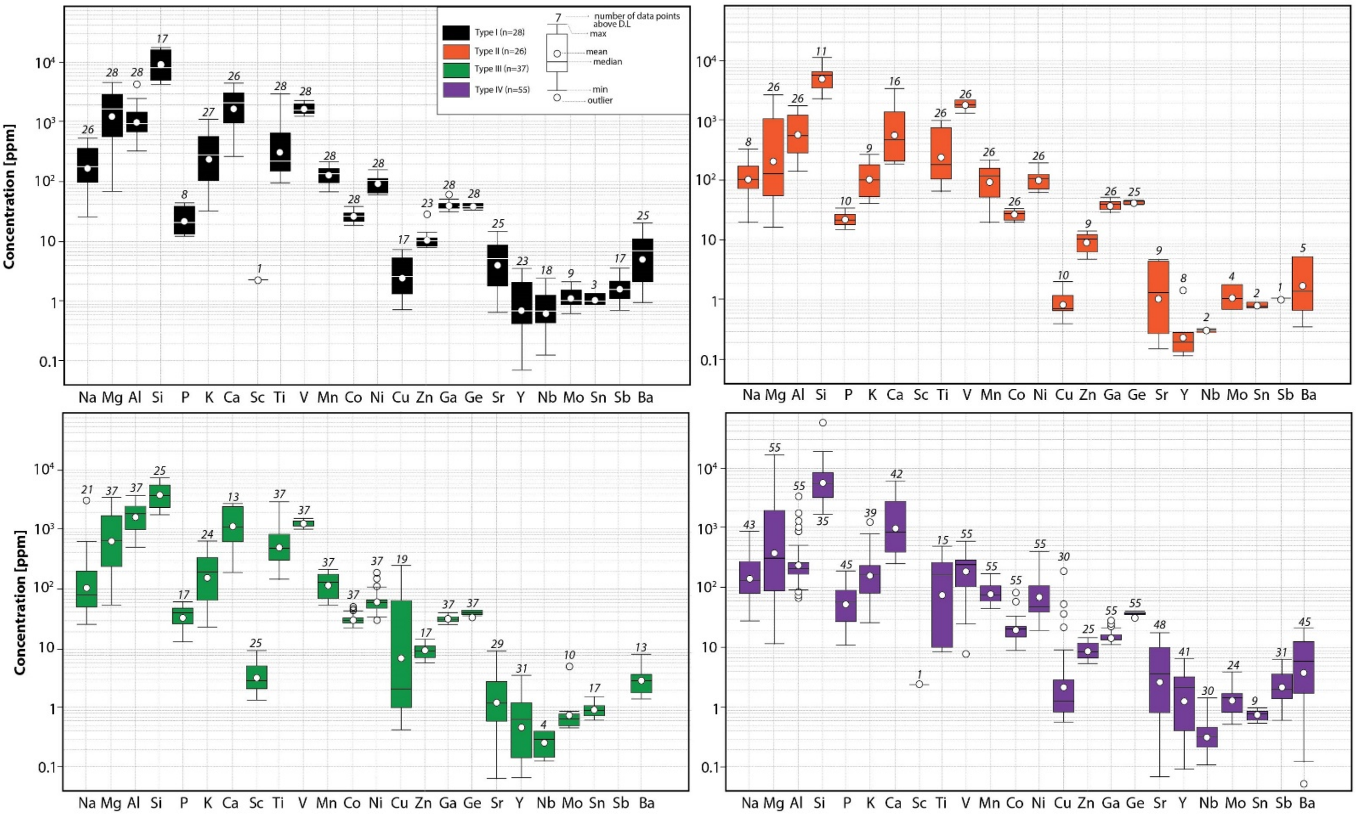

Fig. 10. Statistical summary of trace element concentrations determined by using LA-ICPMS for the magnetite types described in Cerro Negro Norte. Note similar pattern for all types.

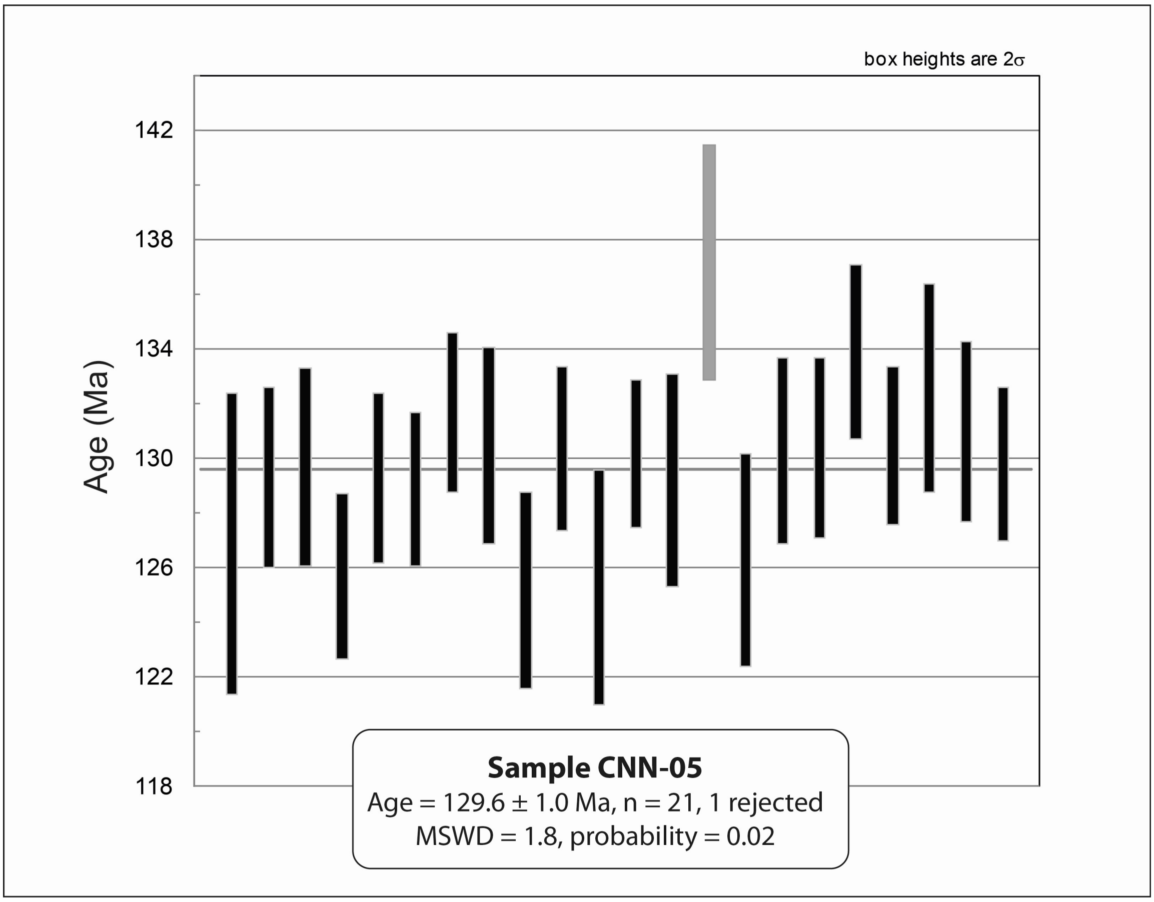

Fig. 11. Weighted average plot for igneous zircons from the diorite intrusion.

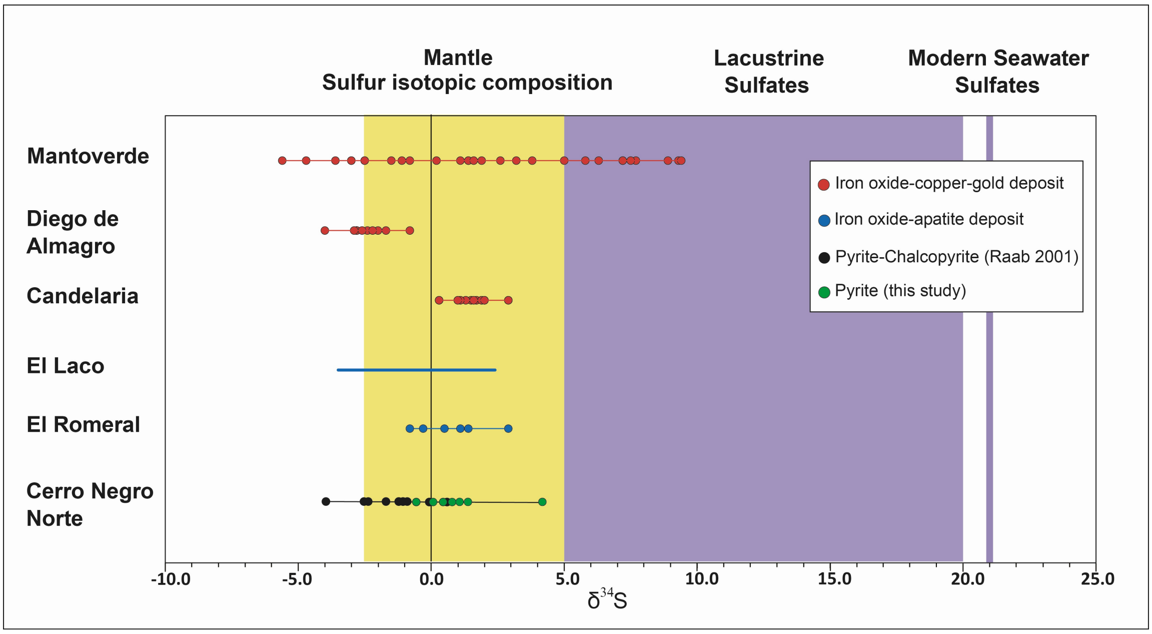

Fig. 12. δ^{34}S values for Cerro Negro Norte and other IOA and IOCG deposits in northern Chile. The values range between -0.5 and +4.3‰ for Cerro Negro Norte, which is consistent with a magmatic source of sulfur. Sulfur data for IOA deposits is less dispersed than for IOCG deposits where other possible sulfur sources have been proposed. Source of data: Mantoverde (Rieger et al. 2010), Diego de Almagro (Loyola 2016); Candelaria (Marschik and Fontboté 2001); El Laco and El Romeral (Rojas et al. 2018b).

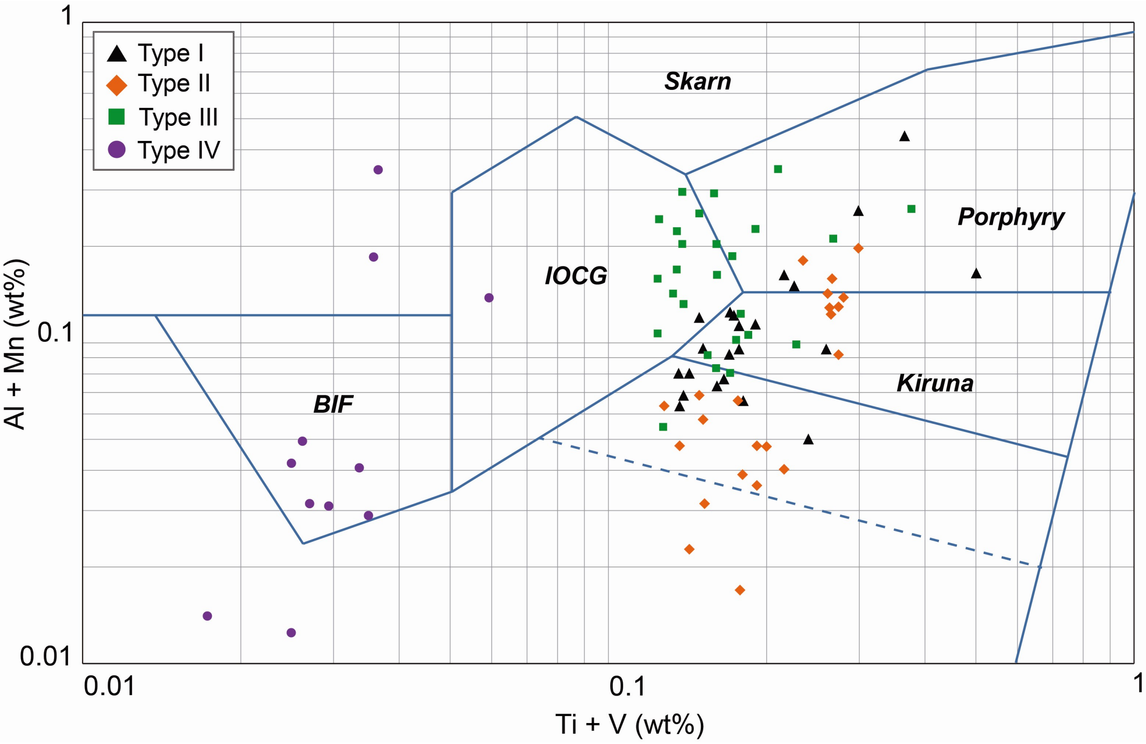

Fig. 13. Chemical discrimination diagram for magnetite after Dupuis and Beaudoin (2011) and modified by Nadoll et al. (2014). Types I and II plot in the Porphyry and Kiruna fields, whereas Type III in the IOCG, Kiruna and Porphyry fields. Magnetite-vein mineralization (Type IV) shows the lowest trace element content and plot mostly in the BIF field. Concentrations determined by using EMPA.

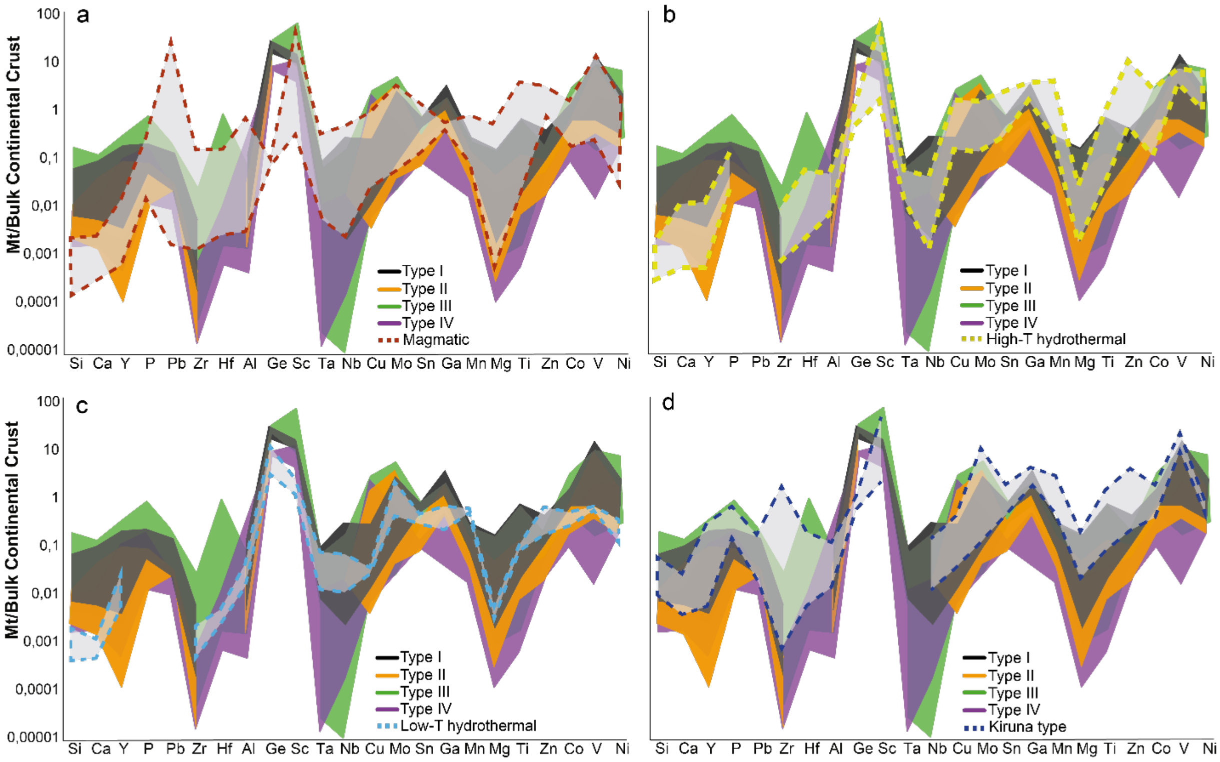

Fig. 14. Trace element spidergrams normalized to bulk continental crust (Rudnick and Gao 2003). Results are compared with available trace element data for (a) magmatic, (b) high-T hydrothermal, and (c) low-T hydrothermal magnetite (Dupuis and Beaudoin 2011; Dare et al. 2015). In addition, results are also compared with data for the Los Colorados Kiruna-type deposit (d) reported by Knipping et al. (2015a,b).

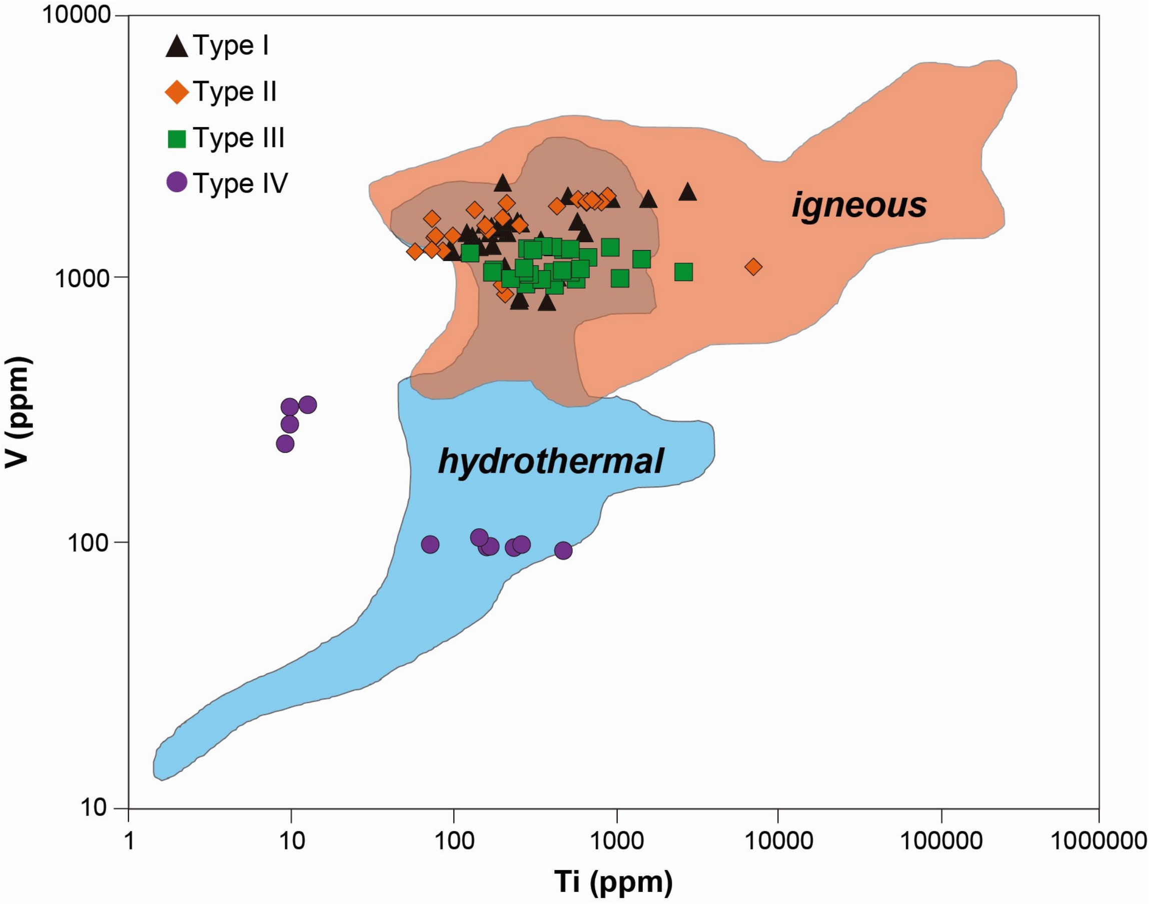

Fig. 15. Ti vs. V concentration in magnetite. Blue field represents hydrothermal magnetite, whereas the red area is defined by igneous magnetite. The data for Cerro Negro Norte plot mostly in the overlapping area with a few samples plotting solely in the igneous magnetite. Type IV magnetite plots in or close to the hydrothermal field. Fields based on data from Nadoll (2011).

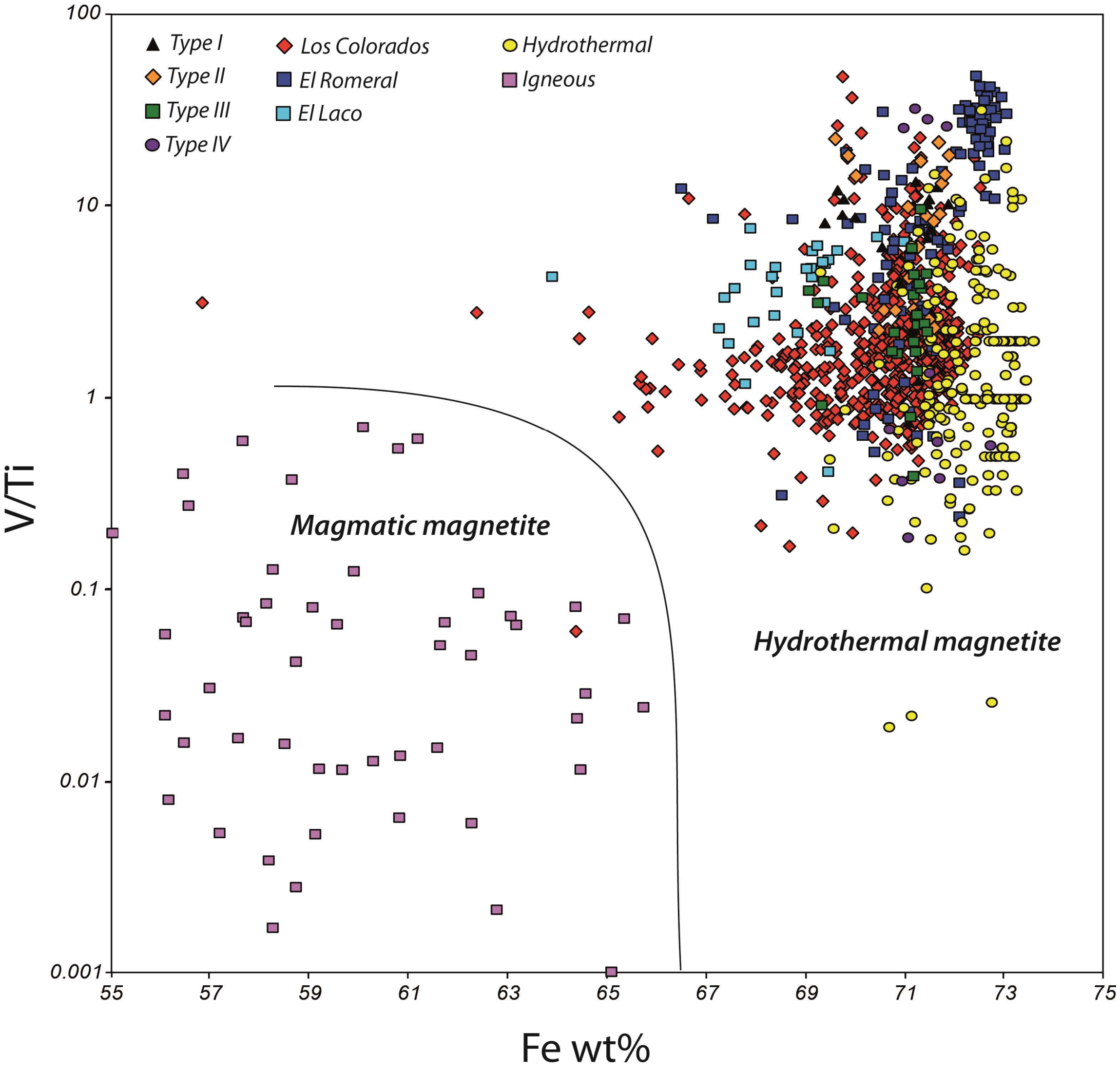

Fig. 16. Magmatic-hydrothermal discrimination diagram proposed by Wen et al. (2017). Data from Cerro Negro Norte and other Andean IOA deposits (El Romeral, Los Colorados and El Laco) plot in the hydrothermal area.

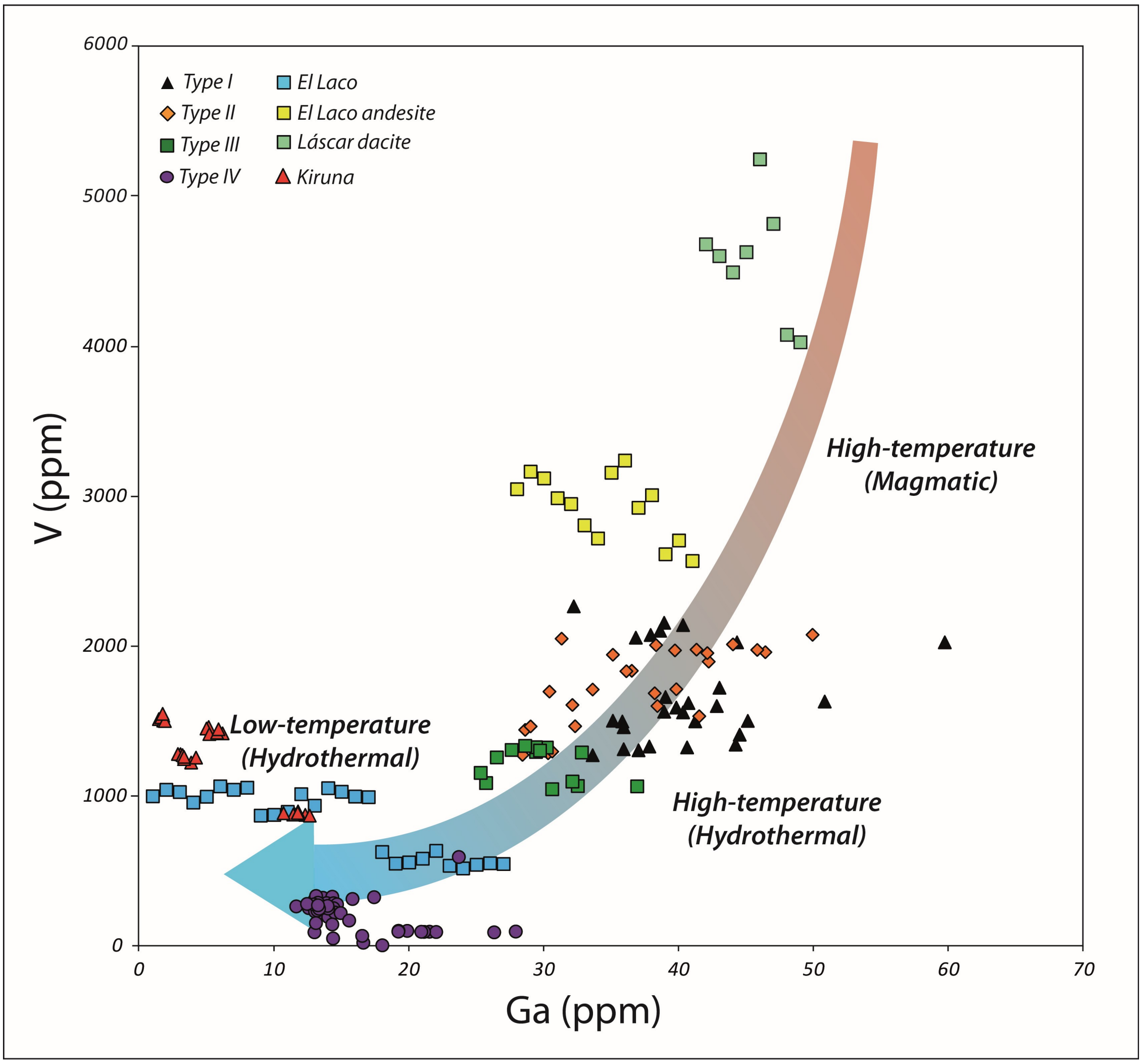

Fig. 17. V vs. Ga content in magnetite. Type I and II magnetite grains plot in a transition position between magmatic and high-temperature hydrothermal conditions. Type III magnetite is associated with high-temperature hydrothermal fluids, whereas Type IV precipitated from low-T, high fO_2 hydrothermal fluids. Data for Kiruna magnetite ore and El Laco and Láscar samples from Broughm et al. (2017).

CAPÍTULO III – CONCLUSIONES

Las observaciones mineralógicas combinadas con técnicas microanalíticas (SEM, EMPA, LA-ICP-MS y micro-Raman) revelan cuatro eventos principales de mineralización: (i) mineralización de magnetita (Tipo I) representada por núcleos de magnetita formados a alta temperatura con presencia de anfíbol, piroxeno y algunas inclusiones de óxidos de Fe-Ti; (ii) magnetita libre de inclusiones (Tipo II), generalmente rodeando núcleos de magnetita primaria Tipo I; (iii) magnetita Tipo III con zonación oscilatoria y química y generalmente sin o con pocas inclusiones; y, (iv), vetillas de magnetita (Tipo IV) con inclusiones dispuestas en bandas oscilantes y sinuosas.

La composición química de los distintos tipos de magnetita reflejan una variación de la temperatura de formación en donde las magnetitas formadas a mayor temperatura presentan altos contenidos de Ti + V, mientras que aquellos formados a baja temperatura presentan bajos contenidos de Ti + V y Al + Mn. En particular, los granos de magnetita muestran contenidos variables de V desde 2269 (Tipo I) a 7.98 ppm (Tipo IV), y concentraciones de Ga, que varían desde 59.7 (Tipo I) a 11.63 ppm (Tipo IV). En base a estas características químicas particulares, se propone un nuevo diagrama basado en los contenidos V y Ga para discriminar entre una formación magmática de una hidrotermal.

La formación de microlitos de magnetita (Tipo I) occurre a partir de magma de composición diorítica, mientras que la composición química de magnetita Tipo II refleja una transición desde condiciones magmáticas a condiciones magmáticas-hidrotermales, en donde las reacciones de disolución-precipitación son inducidas por fluidos de alta temperatura. Finalmente, la magnetita Tipo III y IV son generadas por eventos hidrotermales tardíos evidenciados por la presencia de vetillas de magnetita y sulfuros que cortan transversalmente los principales cuerpos minerales de magnetita

En consecuencia, los datos presentados aquí para el depósito Cerro Negro Norte son consistentes con el modelo de flotación para Los Colorados propuesto por Knipping et al. (2015a, b) y también por Rojas et al. (2017a, b) para el depósito de Fe El Romeral. Por otro lado, los diferentes diagramas de discriminación propuestos por Dupuis y Beaduin (2011), Dare et al. (2014), Knipping et al. (2015a) y Wen et al. (2017) reflejan una variación en base a temperatura de formación. En este trabajo se propone un nuevo diagrama de discriminación basado en la relación de V y Ga. Este diagrama representa de mejor manera los cambios químicos que experimenta la magnetita y permite determinar el origen magmático vs hidrotermal de las magnetitas de Cerro Negro Norte.

BIBLIOGRAFÍA

Aguirre, L. 1985. The Southem Andes. In Ocean Basins and Trenehes (l'Jaim, A.E. M.; Stehli, F.G.; Uyeda, S.; editors). The Pacific Ocean Plenum Press, Vol. 7, p. 265-376. New York.

Altree-Williams, A., Pring, A., Ngothai, Y., and Brugger, J., 2015, Textural and compositional complexities resulting from coupled dissolution-reprecipitation reactions in geomaterials. Earth-Science Reviews, 150, 628–651.

Arevalo, C., 1995, Mapa Geológico del Hoja Copiapo; Region de Atacama, escala 100,000: Documentos de Trabajo: Servicio Nacional de Geologia y Minería.

Arevalo, C., 2005, Mapa Geologico del Hoja Copiapo; Region de Atacama, escala 100,000: Servicio Nacional de Geologia y Minería.

Amilibia, A., Sabat, F., McClay, K. R., Muñoz, J., Chong, G, 2008; The role of inherited tectono-sedimentary architecture in the development of the central Andean mountain belt: Insights from the Cordillera de Domeyko. Journal of Structural Geology, v 30 (12), p. 1520-1539.

Bau, M., and Alexander, B.W., 2009, Distribution of high field strength elements (Y, Zr, REE, Hf, Ta, Th, U) in adjacent magnetite and chert band and in reference standards FeR-3 and FeR-4 from the Temagami iron-formation, Canada, and the redox level of the Neoarchean ocean: Precambrian Res. v.174, p.337-346.

Beard, J. S., and G. E. Lofgren, 1991. Dehydration melting and water-saturated melting of basaltic and andesitic greenstones and amphibolites, J. Petrol., 32,365-401.

Barra, F; Reich, M; Selby, D; Rojas, P; Simon, A; Salazar, E; Palma, G., 2017. Unraveling the origin of the Andean IOCG clan: A Re-Os isotope approach. Ore Geology Reviews http://dx.doi.org/10.1016/j.oregeorev.2016.10.016.

Bilenker, L.D., Simon, A.C., Reich, M., Lundstrom, C.C., Gajos, N., Bindeman, I., Barra, F., and Munizaga, R., 2016, Fe-O stable isotope pairs elucidate a high-temperature origin of Chilean iron oxide-apatite deposits: Geochimica et Cosmochimica Acta, v.177, p.94-104.

Black, L.P., Kamo, S.L., Allen, C.M., Davis, D.W., Aleinikoff, J.N., Valley, J.W., Mundil, R., Campbell, I.H., Korsch, R.J., Williams, I.S., Foudoulis, C., 2004, Improved Pb-206/U-218 microprobe geochronology by the monitoring of a trace-element-related matrix effect; SHRIMP, ID-TIMS, ELA-ICP-MS and oxygen isotope documentation for a series of zircon standards: Chemical Geology, v.205, p.115-140.

Bookstrom, A., 1977, The magnetite deposits of El Romeral, Chile: Economic Geology, v.72, p.1101-1130.

Boric, R., Díaz, F., and Maksaev, V., 1990, Geologia y yacimientos metaliferos de la Region de Antofagasta: Servicio Nacional de Geologia y Mineria, Santiago, Boletin 40.

Brown, M., Diaz, F., and Grocott, J., 1993, Displacement history of the Atacama Fault System 25°00'S-27°00'S, northern Chile: Geological Society of America Bulletin, v. 105, p. 1165-1174.
Cawthorn, R.G., 2005. Contrasting sulphide contents of the Bushveld and Sudbury igneous complexes. Miner Deposita 40:1–12.

Cawthorn, R. G. & McCarthy, T. S. (1980). Variations in Cr content of magnetite from the Upper Zone of the Bushveld Complex: evidence for heterogeneity and convection currents in magma chambers. Earth and Planetary Science Letters 46, 335-343.

Cawthorn, R. G. & McCarthy, T. S. (1985). Incompatible trace element behaviour in the Bushveld Complex. Economic Geology 80, 1016-1026.

Cawthorn, R.G., Ashwal, L.D., 2009. Origin of anorthosite and magnetitite layers in the Bushveld Complex, constrained by major element compositions of plagioclase. J Petrol 50:1607–1637.

Cembrano, J.; González, G.; Arancibia, G.; Olivares, V; Herrera, V 2005. Fault zone development and strain partitioning in an extensional strike-slip duplex: A case study from the Mesozoic Atacama Fault System, Northern Chile. Tectonophysics 400: 105-125.

Dare S. A. S., Barnes S.-J., Beaudoin G., Méric J., Boutroy E. and Potvin-Doucet C. (2014) Trace elements in magnetite as petrogenetic indicators. Miner. Deposita 49, 785–796.

Dare, S.A.S., Barnes, S., and Beaudoin, G., 2015. Did the massive magnetite "lava flows" of El Laco (Chile) form by magmatic or hydrothermal processes? New contraints from magnetite composition by LA-ICP-MS: Mineralium Deposita, v.50, p.607-617.

Eales HV (2000) Implications of the chromium budget of the Western Limb of the Bushveld Complex. S Afr J Geol 103:141.

Espinoza, R.S., Véliz, G.H., Esquivel, L.J., Arias, F.J., Moraga, B.A., 1996. The cupriferous province of the Coastal Range, northern Chile. In: Camus, F., Sillitoe, R.H., Petersen, R. (eds) Andean copper deposits: New discoveries, mineralization styles and metallogeny. Society of Economic Geologist 5, 19–32.

Espinoza, L., 2000, Estudio petrográfico del cuerpo Cerro Principal del distrito ferrífero El Romeral IV región- La Serena, Chile. Memoria para optar al título de geólogo. Universidad de Chile, Facultad de Ciencias Físicas y Matemáticas, Departamento de Geología, Santiago, Chile.

Frietsch R and Perdahl J A 1995 Rare earth elements in apatite and magnetite in Kiruna-type iron ores and some other iron types; Ore Geol. Rev. 9489–510.

Grocott, J., Brown, M., Dallmeyer, R. D., Taylor, G. K., and Treloar, P. J., 1994, Mechanisms of continental growth in extensional arcs: An example from the Andean plate-boundary zone: Geology, v. 22, p. 391-394.

Grocott, J., and Taylor, G. K., 2002, Magmatic arc fault systems, deformation partitioning and emplacement of granitic complexes in the Coastal Cordillera, north Chilean Andes (25°30'S to 27°00'S): Journal of the Geological Society, v. 159, no. 4, p. 425-443.

Harney, D. M.W., von Gruenewaldt, G. & Merkle, R. K.W. (1996). The use of plagioclase composition as an indicator of magmatic processes in the Upper Zone of the Bushveld Complex. Mineralogy and Petrology 56, 91-103.

Hitzman M.W. 2000. Iron, oxide,Cu-Au deposits: What, where, when and why. In Hydrotermal iron oxide, copper- gold and related deposits a global perspective (Porter, T.M., editor). Adelaide, Australian Mineral Foundation: 9-26, Australia.

Kamvong, T., Zaw, K., Siegele, R., 2007. PIXE/PIGE microanalysis of trace elements in hydrothermal magnetite and exploration significance: a pilot study. 15th Australian Conference on Nuclear and Complementary Techniques of Analysis and 9th Vacuum Society of Australia Congress. University of Melbourne, Melbourne, Australia.

Klemm, D. D., Henckel, J., Dehm, R. & von Gruenewaldt, G. (1985). The geochemistry of titanomagnetite in magnetite layers and their host rocks of the Eastern Bushveld Complex. Economic Geology 80, 1075-1088.

Knipping J.L., Bilenker, L.D., Simon, A.C., Reich, M., Barra, F., Deditius, A.P., Lundstrom, C., Bindeman, I., and Munizaga, R., 2015a, Giant Kiruna-type deposits form by efficient flotation of magmatic magnetite suspensions: Geology, v.43, p.591-594.

Knipping J.L., Bilenker, L.D., Simon, A.C., Reich, M., Barra, F., Deditius, A.P., Wälle, M., Heinrich, C.A., Holtz, F., and Munizaga, R., 2015b, Trace elements in magnetite from massive iron oxide-apatite deposits indicate a combined formation by igneous and magmatic-hydrothermal processes: Geochimica et Cosmochimica Acta, v.171, p.15-38.

Laetsch, T., and Downs, T., 2006, Software for identification and refinement of cell parameters from powder diffraction data of minerals using the RRUFF project and American Mineralogist Crystal Structure databases. Abstracts from the 19th General Meeting of the International Mineralogical Association, Kobe, Japan, 23-28 July, 2006.

Lara, L., and Godoy, E., 1998, Hoja Quebrada Salilrosa, Region de Atacama: Servicio Nacional de Geologia y Mineria (SERNAGEOMIN), Mapas Geologicos, 1:100,000 scale, No. 4.

Leuthold, J., Blundy, J.D., Holness, M.B., Sides R., 2014. Successive episodes of reactive liquid flow through a layered intrusion (Unit 9, Rum Eastern Layered Intrusion, Scotland). Contrib Mineral Petrol 168:1–27.

Lledo, H.L., Jenkins, D.M., 2008, Experimental Investigation of the Upper Thermal Stability of Mg-rich Actinolite; Implications for Kiruna-Type Iron Deposits: Journal of Petrology, v.49, p.225-238.

Longerich, H.P., Jackson, S.E., Günther, D., 1996. Laser ablation inductively coupled plasma mass spectrometric transient signal data acquisition and analyte concentration calculation. J. Anal. At. Spectrom. 11 (9), 899e904.

Ludwig, K., 2010, Isoplot/Ex version 4.1, a geochronological toolkit for Microsoft Excel: Berkeley Geochronology Center, Special Publication no.4.

Lykins, R.W. and Jenkins, D.M. (1992) Experimental determination of pargasite stability relations in the presence of orthopyroxene. Contributions to Mineralogy and Petrology, vol. 112, p 405–413.

Maksaev, V., Zentilli, M., 2002. Chilean strata-bound Cu–(Ag) deposits: an overview. In: Porter, T.M. (ed.), Hydrothermal Iron Oxide Copper–Gold and Related Deposits: A Global Perspective, PGC Publishing, Adelaide, pp 163–184.

Marsh, B.D., 2004. A magmatic mush column Rosetta Stone: The McMurdo Dry Valleys of Antarctica, EOS Transactions, American Geophysical Union, vol. 85 pg. 497.

Mathur, R., Marschik, R., Ruiz, J., Munizaga, F., Leveille, R. A., Martin, W., 2002. Age of mineralization of the Candelaria Fe oxide Cu-Au deposit and the origin of the Chilean iron belt, based on Re-Os isotopes. Econ Geol 97, 59-71.

Ménard, J. 1995. Relationship between altered pyroxene diorite and the magnetite mineralization in the Chilean Iron Belt, with emphasis on the El Algarrobo iron deposits (Atacama region, Chile). Miner Deposita, 30, 268–274.

Mpodozis, C. y Ramos, V.A. 1990. The Andes of Chile and Argentina. En Ericksen, G.E., M.T. Cañas Pinochet y J.A. Reinemund (eds.) Geology of the Andes and its relation to Hydrocarbon and Mineral Resources, Circum Pacific Council for Energy and Mineral Resources, Earth Sciences Series 11: 59-90, Houston.

Nadoll P., 2011, Geochemistry of magnetite from hydrothermal ore deposits and host rocks - case studies from the Proterozoic Belt Supergroup, Cu-Mo-porphyry + skarn and Climax-Mo deposits in the western United States. Ph. D. thesis, University of Auckland.

Nadoll, P., 2013, Mineral Inclusions in magnetite as a guide to exploration-Preliminary results: 12th SGA Biennial Meeting 2013 Proceedings, v.1, p.280-282.

Nadoll, P., and Koenig, A.E., 2011, LA-ICP-MS of magnetite: methods and reference materials: Journal of Analytical Atomic Spectrometry, v.26, p.1872-1877.

Nadoll, P., Angerer, T., Mauk, J.L., French, D., and Walshe, J., 2014a, The chemistry of hydrothermal magnetite: a review: Ore Geology Reviews, v.61, p.1-32.

Nadoll, P., Mauk, J.L., Richard, A.L., and Koenig, A.E., 2014b, Geochemistry of magnetite from porphyry Cu and skarn deposits in the southwestern United States: Miner Deposita. http://dx.doi.org/10.1007/s00126-014-0539-y.

Naslund, H. R. & McBirney, A. R. (1996). Mechanisms of formation of igneous layering. In: Cawthorn, R. G. (ed.) Layered Intrusions. Amsterdam: Elsevier, pp. 1-44.

Nold, J.L., Dudley, M.A. and Davidson, P., 2014, The southeast Missouri (USA) Proterozoic iron metallogenic province-Types of deposits and genetic relationships to magnetite-apatite and iron oxide-copper-gold deposits: Ore Geology Reviews, v.57, p.154-171.

Nyström, J.O., and Henríquez, F., 1994, Magmatic features of iron ores of the Kiruna type in Chile and Sweden: Ore textures and magnetite geochemistry: Economic Geology, v.89, p.820-839.

Otake T., Wesolowski D. J., Anovitz L. A., Allard L. F. and Ohmoto H. (2007), Experimental evidence for non-redox transformations between magnetite and hematite under H_2-rich hydrothermal conditions. Earth Planet. Sci. Lett.257, 60–70.

Paton, C., Hellstrom, J., Paul, B., Woodhead, J., y Hergt, J., 2011, Iolite: Freeware for the visualisation and processing of mass spectrometric data: Journal of Analytical Atomic Spectrometry, no.26, p.2508-2518.

Pichowiak, S., Buchelt, M., and Damm, K.-W., 1990, Magmatic activity and tectonic setting of the early stages of the Andean cycle in northern Chile: Geological Society of America Special Papers, v. 241, p. 127-144.

Raab A., 2001, Geology of the Cerro Negro Norte Fe-Oxide (Cu-Au) District, Coastal Cordillera, northern Chile. Msc. D. thesis, Oregon State University.

Reich, M., Simon, A.C., Deditius, A., Barra, F., Chryssoulis, S., Lagas, G., Tardani, D., Knipping, J., Bilenker, L., Sánchez-Alfaro, P., Roberts, M.P., and Munizaga, R., 2016, Trace element signature of pyrite from the Los Colorador Iron oxide-apatite (IOA) deposit, Chile: a missing link between Andean IOA and Iron oxide copper-gold systems: Economic Geology, v.111, p.743-761.

Reynolds, I. M. (1985a). The nature and origin of titaniferous magnetite-rich layers in the Upper Zone of the Bushveld Complex: a review and synthesis. Economic Geology 80, 1089-1108.

Rojas, P., Barra F., Reich, M., Deditius, A., Simon, A., Uribe, F., Romero, R., Rojo, M., 2018, A genetic link between magnetite mineralization and diorite intrusion at the El Romeral iron oxide-apatite deposit, northern Chile. Miner Deposita. https://doi.org/10.1007/s00126-017-0777-x

Rojas, P., Barra F., Deditius, A., Reich, M., Simon, A., Roberts, M., Rojo, M., 2018, New contributions to the understanding of Kiruna-type iron oxide-apatite deposits revealed by magnetite ore and gangue mineral geochemistry at the El Romeral deposit, Chile. Ore Geology Reviews, https://doi.org/10.1016/j.oregeorev.2018.01.003

Rubatto, D., 2002, Zircon trace element geochemistry; partitioning with garnet and the link between U-Pb ages and metamorphism: Chemical Geology, 184, 123-138.

Rudnick R. L. and Gao S. (2003) Composition of the continental crust. In The Crust (ed. R. L. Rudnick) vol. 3, Treatise on Geochemistry (eds. H. D. Holland and K. K. Turekian), Elsevier, Oxford.

Ruiz-Agudo E., Putnis C.V., Putnis A., 2014, Coupled dissolution and precipitation at mineral–fluid interfaces. Chemical Geology, 383, 132-146.

Segerstrom, K. 1968. Geología de las hojas Copiapó y Ojos del Salado, Provincia de Atacama. Instituto de Investigaciones Geológicas, Boletín, No. 24, 58 p.

Scheuber, E., Hammerschmidt, K., and Fiedrichsen, H., 1995, 40Ar/39Ar and Rb-Sr analyses from ductile shear zones from the Atacama Fault Zone, northern Chile: the age of deformation: Tectonophysics, v. 250, p. 61-87.

Scheuber, E., and Gonzalez, G., 1999, Tectonics of the Jurassic-Early Cretaceous magmatic arc of the north Chilean Coastal Cordillera (22°S - 26°S): A story of crustal deformation along a convergent plate boundary: Tectonics, v. 18, no. 5, p. 895-910.

Scheuber, E., and Andriessen, P. A. M., 1990. The kinematic and geodynamic significance of the Atacama Fault Zone, northern Chile: Journal of Structural Geology, v. 12, no. 2, p. 243-257.

Sillitoe, R.H., and Burrows, D.R., 2002. New field evidence bearing on the origin of the El Laco magnetite deposit, northern Chile: Economic Geology, v.97, p.1101-1109.

Sláma, J., Košler, J., Condon, D., Crowley, J., Gerdes, A., Hanchar, J., Horstwood, M., Morris, G., Nasdala, L., Norberg, N., Schaltegger, U., Schoene, B., Tubrett, M., Whitehouse, M., 2008. Plešovice zircon — A new natural reference material for U–Pb and Hf isotopic microanalysis: Chemical Geology, v.249, p.1-35.

Tegner, C., Cawthorn, R. G. & Kruger, F. J. (2006). Cyclicity in the Main and Upper Zones of the Bushveld Complex, South Africa: crystallization from a zoned magma sheet. Journal of Petrology 47, 2257-2279.

Toplis, M.J. and Carroll, M.R., 1995. An experimental study of the influence of oxygen fugacity on Fe–Ti oxide stability, phase relations, and mineral-melt equilibria in ferro-basaltic systems. J Petrol 36:1137–1170.

Toplis, M. J. & Corgne, A. (2002). An experimental study of element partitioning between magnetite, clinopyroxene and iron-bearing silicate liquids with particular emphasis on vanadium. Contributions to Mineralogy and Petrology, Vol. 144, p 22-37.

Van Baalen, M.R., 1993. Titanium mobility in metamorphic systems: a review. Chem. Geol. 110, 233–249.

Vaughan, D. J., and Craig, J. R., 1978, Mineral chemistry of metal sulfides: Cambridge University Press.

Veksler, I. V., Dorfman, A. M., Borisov, A. A., Wirth, R. and Dingwell, D. B. (2007). Liquid immiscibility and the evolution of basaltic magma. Journal of Petrology 48, 218-2210.

Vivallo, W.; Henríquez, F.; Espinoza, S. 1995a. Metasomatismo y alteración hidrotermal en el distrito ferrífero Cerro Negro Norte, Copiapó, Chile. Revista Geológica de Chile, Vol. 22, No. 1, p. 75-88.

Vivallo, W., Espinoza, S. y Henríquez, F., 1995. Los depósitos de hierro del tipo magnetita-apatita: geoquímica de las rocas volcánicas asociadas y potencialidad de la mena de hierro como fuente de mineralización de oro. Revista Geológica de Chile, Vol.22, Nº 2, 159-175.

Wen G., Li J.W., Hofstra, A., Koenig, A.E., Lowers, H.A., Adams, D., 2017. Hydrothermal reequilibration of igneous magnetite in altered granitic plutons and its implications for magnetite classification schemes: Insights from the Handan-Xingtai iron district, North China Craton. Geochimica et Cosmochimica Acta, Vol. 213, p 255-270.

Williams, P.J., Barton, M.D., Johnson, D.A., Fontboté, L., De Haller, A., Mark, G., Oliver, N.H.S., and Marschik, R., 2005, Iron oxide copper-gold deposits: Geology, space-time distribution, and possible modes of origin. Economic Geology, 100th Anniversary Volume, p.371-405.

Yin, S., Ma, C., Robinson, P.T., 2017, Textures and high field strength elements in hydrothermal magnetite from a skarn system: Implications for coupled dissolution-reprecipitation reactions. American Mineralogist, Vol. 102, p 10.

MATERIAL COMPLEMENTARIO

Tabla 1. Microsonda Electrónica en Magnetita

Element		**Al**	**Si**	**Cr**	**Ti**	**V**	**Ca**	**Fe**	**Mn**	**Mg**	**Zn**	**Ni**	**Cu**	**Na**	**K**	**O**	**Total**
Line		Kα	Kα	Kα	Kα	Kα	Kα	Kα	Kα	Kα	Kα	Kα	Kα	Kα	Kα		
Detection limit (wt%)		0,019	0,019	0,012	0,021	0,044	0,016	0,11	0,051	0,025	0,142	0,083	0,109	0,034	0,015		
Sample	**Type**	**(wt%)**	**(wt%)**	**(wt%)**	**(wt%)**	**(wt%)**	**(wt%)**	**(wt%)**	**(wt%)**	**(wt%)**	**(wt%)**	**(wt%)**	**(wt%)**	**(wt%)**	**(wt%)**	**(wt%)**	**(wt%)**
BEDII23_01_MT1_01	I	0,026	0,041	B.D.L.	B.D.L.	0,155	0,026	71,61	N.D.	B.D.L.	B.D.L.	B.D.L.	N.D.	0,211	0,081	20,54	92,02
BEDII23_01_MT1_02	I	B.D.L.	0,025	0,013	N.D.	0,160	B.D.L.	71,44	N.D.	B.D.L.	B.D.L.	N.D.	N.D.	0,086	0,039	20,77	92,96
BEDII23_01_MT1_03	I	0,046	0,492	0,012	0,019	0,199	0,212	70,53	B.D.L.	0,109	B.D.L.	B.D.L.	B.D.L.	0,081	0,055	20,65	92,48
BEDII23_01_MT1_04	I	B.D.L.	0,019	0,008	B.D.L.	0,189	0,030	70,23	0,058	N.D.	B.D.L.	N.D.	N.D.	0,136	0,214	21,13	92,93
BEDII23_01_MT1_05	I	B.D.L.	0,018	N.D.	B.D.L.	0,193	B.D.L.	71,41	N.D.	B.D.L.	B.D.L.	N.D.	N.D.	0,061	0,030	20,39	91,38
BEDII23_01_MT2_01	II	0,022	B.D.L.	B.D.L.	B.D.L.	0,175	B.D.L.	71,54	N.D.	B.D.L.	B.D.L.	B.D.L.	N.D.	0,081	B.D.L.	20,62	92,38
BEDII23_01_MT2_02	II	0,060	B.D.L.	B.D.L.	B.D.L.	0,181	B.D.L.	71,31	N.D.	N.D.	B.D.L.	B.D.L.	N.D.	0,116	B.D.L.	20,67	92,60
BEDII23_01_MT2_03	II	0,054	B.D.L.	B.D.L.	B.D.L.	0,173	N.D.	71,22	N.D.	B.D.L.	N.D.	B.D.L.	B.D.L.	0,071	B.D.L.	20,65	92,45
BEDII23_01_MT2_04	II	0,064	B.D.L.	0,008	B.D.L.	0,175	B.D.L.	71,88	B.D.L.	B.D.L.	N.D.	N.D.	N.D.	0,064	B.D.L.	20,61	92,23
BEDII23_01_MT2_05	II	0,020	B.D.L.	0,006	B.D.L.	0,210	B.D.L.	71,66	B.D.L.	B.D.L.	B.D.L.	B.D.L.	B.D.L.	0,105	0,019	20,79	93,04
BEDII23_01_MT2_06	II	0,023	B.D.L.	N.D.	N.D.	0,204	B.D.L.	71,48	N.D.	N.D.	B.D.L.	B.D.L.	N.D.	0,061	B.D.L.	20,74	92,91
BEDII23_02_MT1_01	I	B.D.L.	0,030	B.D.L.	B.D.L.	0,173	0,018	69,99	B.D.L.	B.D.L.	B.D.L.	B.D.L.	B.D.L.	0,037	B.D.L.	20,66	92,54
BEDII23_02_MT1_02	I	B.D.L.	0,020	0,010	N.D.	0,158	B.D.L.	69,76	B.D.L.	B.D.L.	B.D.L.	B.D.L.	N.D.	0,053	B.D.L.	20,24	90,64
BEDII23_02_MT1_03	I	0,022	0,021	B.D.L.	B.D.L.	0,168	B.D.L.	69,38	B.D.L.	B.D.L.	B.D.L.	N.D.	B.D.L.	0,246	0,041	20,15	90,26
BEDII23_02_MT1_04	I	B.D.L.	0,022	N.D.	B.D.L.	0,159	B.D.L.	69,73	B.D.L.	N.D.	B.D.L.	N.D.	N.D.	0,046	0,020	20,12	90,10
BEDII23_02_MT1_05	I	0,026	0,031	B.D.L.	N.D.	0,167	0,017	69,63	B.D.L.	B.D.L.	B.D.L.	N.D.	B.D.L.	B.D.L.	B.D.L.	20,13	90,16
BEDII23_02_MT2_01	II	0,026	0,024	B.D.L.	B.D.L.	0,165	B.D.L.	70,01	B.D.L.	B.D.L.	N.D.	B.D.L.	N.D.	B.D.L.	B.D.L.	20,12	90,10
BEDII23_02_MT2_02	II	0,057	B.D.L.	N.D.	B.D.L.	0,177	B.D.L.	69,38	N.D.	N.D.	N.D.	N.D.	B.D.L.	B.D.L.	N.D.	20,21	90,49

BEDII23_02_MT2_03	II	0,038	0,023	B.D.L.	B.D.L.	0,169	N.D.	69,85	B.D.L.	B.D.L.	N.D.	B.D.L.	N.D.	0,044	B.D.L.	20,05	89,72
BEDII23_02_MT2_04	II	0,040	0,022	N.D.	N.D.	0,173	N.D.	69,72	N.D.	B.D.L.	N.D.	B.D.L.	N.D.	0,046	B.D.L.	20,19	90,36
BEDII23_02_MT2_05	II	0,025	0,024	B.D.L.	B.D.L.	0,166	B.D.L.	69,59	B.D.L.	B.D.L.	B.D.L.	N.D.	N.D.	0,050	N.D.	20,16	90,22
BEDII23_03_MT1_01	I	B.D.L.	B.D.L.	B.D.L.	B.D.L.	0,157	0,018	69,90	B.D.L.	B.D.L.	B.D.L.	N.D.	N.D.	B.D.L.	0,034	20,11	90,05
BEDII23_03_MT1_02	I	0,028	0,023	N.D.	B.D.L.	0,174	B.D.L.	70,09	B.D.L.	B.D.L.	N.D.	B.D.L.	B.D.L.	B.D.L.	B.D.L.	20,15	90,32
BEDII23_03_MT1_03	I	B.D.L.	B.D.L.	N.D.	B.D.L.	0,163	0,018	69,99	B.D.L.	B.D.L.	N.D.	B.D.L.	B.D.L.	B.D.L.	B.D.L.	20,26	90,70
BEDII23_03_MT1_04	I	0,036	0,182	B.D.L.	0,025	0,167	0,028	69,61	B.D.L.	B.D.L.	B.D.L.	B.D.L.	B.D.L.	0,064	0,063	20,19	90,48
BEDII23_03_MT1_05	I	0,039	0,098	B.D.L.	0,022	0,166	0,028	69,89	B.D.L.	B.D.L.	N.D.	N.D.	N.D.	B.D.L.	0,056	20,36	90,69
BEDII23_03_MT2_01	II	0,025	B.D.L.	B.D.L.	N.D.	0,165	0,021	70,21	B.D.L.	B.D.L.	B.D.L.	N.D.	N.D.	B.D.L.	N.D.	20,31	90,66
BEDII23_03_MT2_02	II	0,035	0,023	B.D.L.	B.D.L.	0,160	N.D.	69,63	B.D.L.	B.D.L.	B.D.L.	N.D.	B.D.L.	B.D.L.	B.D.L.	20,26	90,77
BEDII23_03_MT2_03	II	0,043	0,019	N.D.	B.D.L.	0,153	B.D.L.	69,89	N.D.	B.D.L.	B.D.L.	B.D.L.	N.D.	B.D.L.	B.D.L.	20,12	90,09
BEDII23_03_MT2_04	II	0,048	B.D.L.	0,011	B.D.L.	0,162	B.D.L.	70,11	N.D.	B.D.L.	B.D.L.	N.D.	N.D.	0,041	B.D.L.	20,19	90,37
BEDII23_03_MT2_05	II	0,039	0,019	0,010	B.D.L.	0,164	N.D.	70,01	N.D.	B.D.L.	B.D.L.	B.D.L.	N.D.	0,054	B.D.L.	20,25	90,66
BEDII23_04_MT2_01	II	B.D.L.	B.D.L.	0,011	B.D.L.	0,188	B.D.L.	71,69	N.D.	B.D.L.	N.D.	N.D.	N.D.	0,086	B.D.L.	20,25	90,67
BEDII23_04_MT2_02	II	0,050	0,037	B.D.L.	0,025	0,230	0,023	71,48	N.D.	B.D.L.	B.D.L.	B.D.L.	N.D.	0,142	0,018	20,70	92,73
BEDII23_04_MT2_03	II	0,044	B.D.L.	0,011	B.D.L.	0,208	B.D.L.	71,42	B.D.L.	B.D.L.	B.D.L.	B.D.L.	N.D.	0,094	0,016	20,78	92,88
BEDII23_04_MT2_04	II	0,048	0,027	B.D.L.	0,019	0,178	B.D.L.	71,57	B.D.L.	B.D.L.	N.D.	B.D.L.	N.D.	0,056	B.D.L.	20,68	92,57
BEDII23_04_MT2_05	II	0,025	0,027	0,009	0,019	0,200	N.D.	71,73	N.D.	B.D.L.	B.D.L.	B.D.L.	N.D.	0,057	B.D.L.	20,72	92,68
BEDII23_04_MT1_01	I	B.D.L.	B.D.L.	0,011	B.D.L.	0,175	0,031	71,16	B.D.L.	B.D.L.	B.D.L.	N.D.	B.D.L.	0,298	0,040	20,76	92,91
BEDII23_04_MT1_02	I	B.D.L.	B.D.L.	N.D.	B.D.L.	0,141	0,018	71,26	B.D.L.	N.D.	B.D.L.	B.D.L.	N.D.	0,170	0,037	20,63	92,42
BEDII23_04_MT1_03	I	0,040	B.D.L.	0,011	B.D.L.	0,139	0,021	71,50	N.D.	B.D.L.	B.D.L.	B.D.L.	B.D.L.	0,111	B.D.L.	20,62	92,36
BEDII23_04_MT1_04	I	0,044	0,052	N.D.	B.D.L.	0,147	0,027	71,21	B.D.L.	N.D.	B.D.L.	B.D.L.	B.D.L.	0,132	0,046	20,68	92,59
BEDII23_04_MT1_05	I	B.D.L.	B.D.L.	0,013	N.D.	0,153	B.D.L.	71,45	N.D.	N.D.	B.D.L.	B.D.L.	N.D.	0,124	0,021	20,67	92,42
BEDII23_05_MT_01	II	0,027	B.D.L.	0,011	N.D.	0,139	B.D.L.	71,31	N.D.	N.D.	B.D.L.	B.D.L.	N.D.	0,116	0,026	20,63	92,47
BEDII23_05_MT_02	II	0,034	B.D.L.	N.D.	B.D.L.	0,144	B.D.L.	71,80	B.D.L.	N.D.	B.D.L.	B.D.L.	B.D.L.	0,076	B.D.L.	20,61	92,37
BEDII23_05_MT_03	I	B.D.L.	B.D.L.	N.D.	B.D.L.	0,143	0,017	71,80	B.D.L.	N.D.	N.D.	B.D.L.	B.D.L.	0,107	B.D.L.	20,75	92,95

BEDII23_05_MT_04	I	B.D.L.	0,024	N.D.	B.D.L.	0,142	0,022	71,46	B.D.L.	N.D.	N.D.	B.D.L.	B.D.L.	0,074	0,034	20,72	92,87
BEDII23_05_MT_05	I	B.D.L.	B.D.L.	B.D.L.	B.D.L.	0,147	0,019	71,55	0,052	N.D.	B.D.L.	B.D.L.	B.D.L.	0,069	0,019	20,64	92,45
BEDII23_05_MT_06	I	B.D.L.	B.D.L.	B.D.L.	B.D.L.	0,140	0,020	71,64	B.D.L.	N.D.	B.D.L.	N.D.	B.D.L.	0,043	B.D.L.	20,66	92,62
BEDII23_05_MT_07	I	0,027	0,019	B.D.L.	B.D.L.	0,137	0,018	71,03	B.D.L.	B.D.L.	B.D.L.	B.D.L.	N.D.	0,072	0,056	20,66	92,59
BEDII23_05_MT_08	I	B.D.L.	0,024	B.D.L.	B.D.L.	0,146	0,017	71,56	B.D.L.	N.D.	B.D.L.	B.D.L.	B.D.L.	0,102	0,061	20,53	91,98
BEDII23_05_MT_09	I	B.D.L.	0,029	B.D.L.	N.D.	0,139	0,019	71,87	N.D.	B.D.L.	B.D.L.	N.D.	N.D.	0,072	0,028	20,67	92,64
BEDII23_05_MT_10	II	0,020	0,173	N.D.	B.D.L.	0,151	0,170	71,21	N.D.	B.D.L.	N.D.	B.D.L.	B.D.L.	0,073	B.D.L.	20,75	92,92
BEDII23_05_MT_11	II	0,035	B.D.L.	N.D.	B.D.L.	0,143	B.D.L.	71,58	B.D.L.	B.D.L.	B.D.L.	B.D.L.	B.D.L.	0,088	B.D.L.	20,80	92,65
BEDII23_05_MT_12	II	B.D.L.	0,027	B.D.L.	B.D.L.	0,131	B.D.L.	71,67	B.D.L.	B.D.L.	B.D.L.	B.D.L.	N.D.	0,126	0,019	20,67	92,61
BED09_01_MT_01	III	0,099	0,227	N.D.	0,042	0,021	0,101	70,85	N.D.	B.D.L.	B.D.L.	B.D.L.	0,192	B.D.L.	B.D.L.	20,81	92,46
BED09_02_MT_02	III	0,284	0,571	B.D.L.	0,126	B.D.L.	0,220	70,28	B.D.L.	0,047	B.D.L.	N.D.	B.D.L.	0,053	0,043	21,30	93,02
BED09_01_MT_03	III	0,029	B.D.L.	B.D.L.	0,020	B.D.L.	N.D.	71,81	B.D.L.	N.D.	N.D.	N.D.	B.D.L.	0,043	B.D.L.	20,67	92,69
BED09_01_MT_04	III	0,031	B.D.L.	N.D.	B.D.L.	0,020	B.D.L.	71,99	B.D.L.	B.D.L.	N.D.	N.D.	B.D.L.	B.D.L.	B.D.L.	20,71	92,84
BED09_01_MT_05	III	0,031	0,018	B.D.L.	B.D.L.	B.D.L.	N.D.	71,96	B.D.L.	B.D.L.	B.D.L.	N.D.	N.D.	B.D.L.	B.D.L.	20,71	92,85
BED09_01_MT_06	III	0,338	0,564	B.D.L.	0,117	N.D.	0,210	70,43	B.D.L.	0,056	B.D.L.	B.D.L.	B.D.L.	0,083	0,051	21,38	93,32
BED09_01_MT_07	III	B.D.L.	0,025	B.D.L.	B.D.L.	B.D.L.	B.D.L.	71,61	B.D.L.	N.D.	B.D.L.	B.D.L.	B.D.L.	B.D.L.	B.D.L.	20,61	92,45
BED09_02_MT_01	III	0,024	0,046	B.D.L.	B.D.L.	B.D.L.	N.D.	71,69	N.D.	B.D.L.	B.D.L.	B.D.L.	N.D.	0,047	B.D.L.	20,65	92,50
BED09_02_MT_02	III	0,067	0,140	N.D.	0,031	B.D.L.	0,047	71,35	B.D.L.	B.D.L.	N.D.	B.D.L.	N.D.	0,051	B.D.L.	20,74	92,49
BED09_02_MT_03	III	0,034	B.D.L.	B.D.L.	B.D.L.	B.D.L.	N.D.	71,91	N.D.	N.D.	B.D.L.	B.D.L.	B.D.L.	0,037	N.D.	20,68	92,73
BED09_02_MT_04	III	0,056	B.D.L.	B.D.L.	B.D.L.	B.D.L.	B.D.L.	72,05	B.D.L.	B.D.L.	N.D.	B.D.L.	N.D.	B.D.L.	N.D.	20,74	92,94
BED09_02_MT_05	III	0,049	0,022	B.D.L.	B.D.L.	B.D.L.	B.D.L.	72,06	B.D.L.	B.D.L.	B.D.L.	B.D.L.	B.D.L.	B.D.L.	N.D.	20,74	92,94
BED09_02_MT_06	III	0,039	B.D.L.	B.D.L.	B.D.L.	B.D.L.	N.D.	71,83	B.D.L.	B.D.L.	B.D.L.	B.D.L.	B.D.L.	B.D.L.	N.D.	20,67	92,64
BED09_02_MT_07	III	B.D.L.	B.D.L.	N.D.	B.D.L.	B.D.L.	N.D.	71,79	N.D.	B.D.L.	B.D.L.	N.D.	N.D.	B.D.L.	N.D.	20,60	92,45
BED09_02_MT_08	III	0,019	0,029	B.D.L.	B.D.L.	B.D.L.	B.D.L.	71,36	B.D.L.	N.D.	B.D.L.	N.D.	B.D.L.	0,047	0,040	20,56	92,16
BED09_02_MT_09	III	B.D.L.	B.D.L.	B.D.L.	B.D.L.	B.D.L.	B.D.L.	71,96	N.D.	N.D.	N.D.	N.D.	N.D.	B.D.L.	B.D.L.	20,66	92,70
BED09_02_MT_10	III	B.D.L.	B.D.L.	B.D.L.	0,445	B.D.L.	B.D.L.	71,09	B.D.L.	B.D.L.	B.D.L.	B.D.L.	B.D.L.	B.D.L.	B.D.L.	20,74	92,45

BED09_03_MT_01	III	0,022	B.D.L.	N.D.	B.D.L.	0,021	N.D.	71,54	N.D.	N.D.	N.D.	B.D.L.	B.D.L.	B.D.L.	B.D.L.	20,57	92,24
BED09_03_MT_02	III	B.D.L.	B.D.L.	B.D.L.	B.D.L.	B.D.L.	0,018	71,49	N.D.	N.D.	N.D.	N.D.	N.D.	0,085	0,043	20,56	92,24
BED09_03_MT_03	III	B.D.L.	B.D.L.	B.D.L.	B.D.L.	B.D.L.	B.D.L.	71,47	N.D.	N.D.	N.D.	N.D.	B.D.L.	B.D.L.	B.D.L.	20,53	92,13
BED09_03_MT_04	III	B.D.L.	B.D.L.	B.D.L.	B.D.L.	B.D.L.	B.D.L.	71,61	B.D.L.	B.D.L.	B.D.L.	N.D.	B.D.L.	B.D.L.	0,016	20,59	92,37
BED09_03_MT_05	III	0,081	0,167	B.D.L.	0,026	B.D.L.	B.D.L.	71,16	B.D.L.	B.D.L.	N.D.	N.D.	B.D.L.	0,054	0,062	20,72	92,32
BED09_03_MT_06	III	0,135	0,193	N.D.	B.D.L.	B.D.L.	0,019	71,00	B.D.L.	B.D.L.	B.D.L.	N.D.	B.D.L.	0,064	0,081	20,76	92,33
BED09_03_MT_07	III	0,030	B.D.L.	N.D.	0,051	B.D.L.	B.D.L.	71,53	B.D.L.	N.D.	N.D.	B.D.L.	B.D.L.	B.D.L.	B.D.L.	20,61	92,37
BED09_03_MT_08	III	0,033	B.D.L.	B.D.L.	N.D.	B.D.L.	N.D.	71,58	B.D.L.	N.D.	B.D.L.	B.D.L.	B.D.L.	B.D.L.	B.D.L.	20,60	92,40
BED09_04_MT_01	III	B.D.L.	B.D.L.	B.D.L.	N.D.	N.D.	N.D.	71,90	B.D.L.	N.D.	N.D.	N.D.	N.D.	0,072	B.D.L.	20,65	92,67
BED09_04_MT_02	III	B.D.L.	B.D.L.	B.D.L.	B.D.L.	B.D.L.	B.D.L.	71,65	B.D.L.	B.D.L.	B.D.L.	B.D.L.	B.D.L.	0,076	B.D.L.	20,61	92,46
BED09_04_MT_03	III	B.D.L.	B.D.L.	B.D.L.	B.D.L.	B.D.L.	N.D.	71,72	N.D.	B.D.L.	B.D.L.	B.D.L.	N.D.	B.D.L.	B.D.L.	20,61	92,45
BED09_04_MT_04	III	0,020	B.D.L.	B.D.L.	B.D.L.	B.D.L.	B.D.L.	71,81	B.D.L.	B.D.L.	N.D.	N.D.	B.D.L.	0,103	B.D.L.	20,67	92,74
BED09_04_MT_05	III	0,026	B.D.L.	B.D.L.	B.D.L.	B.D.L.	B.D.L.	71,47	N.D.	N.D.	N.D.	B.D.L.	N.D.	0,078	B.D.L.	20,56	92,20
BED09_04_MT_06	III	B.D.L.	0,025	N.D.	B.D.L.	B.D.L.	B.D.L.	71,72	B.D.L.	B.D.L.	N.D.	B.D.L.	B.D.L.	0,082	0,044	20,65	92,59
BED09_05_MT_01	III	0,030	B.D.L.	B.D.L.	B.D.L.	B.D.L.	N.D.	71,46	N.D.	B.D.L.	N.D.	B.D.L.	B.D.L.	0,111	B.D.L.	20,60	92,35
BED09_05_MT_02	III	0,044	B.D.L.	N.D.	B.D.L.	B.D.L.	B.D.L.	71,64	N.D.	B.D.L.	B.D.L.	B.D.L.	B.D.L.	0,108	0,018	20,68	92,69
BED09_05_MT_03	III	0,069	B.D.L.	B.D.L.	B.D.L.	0,022	B.D.L.	71,58	B.D.L.	B.D.L.	N.D.	B.D.L.	B.D.L.	0,113	B.D.L.	20,65	92,50
BED09_05_MT_04	III	0,033	B.D.L.	B.D.L.	B.D.L.	B.D.L.	B.D.L.	71,54	N.D.	B.D.L.	B.D.L.	N.D.	B.D.L.	0,092	0,016	20,60	92,36
BED09_05_MT_05	III	0,028	0,020	B.D.L.	B.D.L.	B.D.L.	N.D.	71,43	N.D.	N.D.	B.D.L.	B.D.L.	N.D.	0,115	B.D.L.	20,58	92,24
BED09_06_MT_01	III	0,105	0,054	B.D.L.	0,041	B.D.L.	B.D.L.	70,96	B.D.L.	B.D.L.	B.D.L.	N.D.	B.D.L.	0,122	0,037	20,59	91,99
BED09_06_MT_02	III	0,058	B.D.L.	B.D.L.	0,020	B.D.L.	B.D.L.	71,44	B.D.L.	N.D.	N.D.	B.D.L.	B.D.L.	0,084	B.D.L.	20,59	92,28
BED09_06_MT_03	III	0,040	N.D.	B.D.L.	B.D.L.	B.D.L.	B.D.L.	71,37	B.D.L.	N.D.	N.D.	B.D.L.	N.D.	0,103	B.D.L.	20,55	92,14
BED09_06_MT_04	III	0,048	B.D.L.	B.D.L.	B.D.L.	B.D.L.	B.D.L.	71,64	B.D.L.	B.D.L.	N.D.	N.D.	N.D.	0,099	B.D.L.	20,64	92,49
BED09_06_MT_05	III	B.D.L.	0,018	N.D.	B.D.L.	0,022	B.D.L.	72,71	B.D.L.	B.D.L.	N.D.	B.D.L.	B.D.L.	B.D.L.	B.D.L.	20,92	93,84
BED09_06_MT_06	III	B.D.L.	B.D.L.	B.D.L.	B.D.L.	B.D.L.	B.D.L.	71,49	B.D.L.	N.D.	B.D.L.	B.D.L.	B.D.L.	0,087	B.D.L.	20,56	92,26
BED09_06_MT_07	III	B.D.L.	B.D.L.	B.D.L.	B.D.L.	B.D.L.	B.D.L.	71,48	B.D.L.	N.D.	N.D.	N.D.	B.D.L.	0,062	B.D.L.	20,55	92,18

BEDII31_01_MT_01	I	0,031	B.D.L.	0,007	B.D.L.	0,240	B.D.L.	71,25	B.D.L.	N.D.	N.D.	B.D.L.	B.D.L.	0,071	B.D.L.	20,62	92,32
BEDII31_01_MT_02	I	0,063	B.D.L.	0,014	0,025	0,236	B.D.L.	71,05	B.D.L.	N.D.	N.D.	B.D.L.	B.D.L.	0,084	B.D.L.	20,61	92,16
BEDII31_01_MT_03	I	0,036	B.D.L.	0,003	0,019	0,238	B.D.L.	71,53	B.D.L.	N.D.	N.D.	N.D.	B.D.L.	0,057	B.D.L.	20,69	92,62
BEDII31_01_MT_04	II	0,056	B.D.L.	0,003	B.D.L.	0,236	B.D.L.	71,16	B.D.L.	B.D.L.	N.D.	B.D.L.	N.D.	0,246	0,020	20,68	92,48
BEDII31_01_MT_05	II	0,066	B.D.L.	0,007	B.D.L.	0,228	B.D.L.	71,16	B.D.L.	B.D.L.	N.D.	N.D.	N.D.	0,083	B.D.L.	20,61	92,23
BEDII31_01_MT_06	II	0,085	0,021	B.D.L.	0,032	0,240	B.D.L.	71,40	B.D.L.	B.D.L.	N.D.	N.D.	N.D.	0,097	B.D.L.	20,74	92,66
BEDII31_02_MT_01	I	0,029	B.D.L.	B.D.L.	0,355	0,196	B.D.L.	70,57	B.D.L.	N.D.	B.D.L.	B.D.L.	N.D.	B.D.L.	B.D.L.	20,64	91,97
BEDII31_02_MT_02	I	0,071	B.D.L.	0,007	B.D.L.	0,192	N.D.	71,21	B.D.L.	B.D.L.	N.D.	B.D.L.	N.D.	B.D.L.	N.D.	20,61	92,20
BEDII31_02_MT_03	I	0,223	B.D.L.	N.D.	0,195	0,189	B.D.L.	71,07	B.D.L.	B.D.L.	N.D.	B.D.L.	B.D.L.	B.D.L.	B.D.L.	20,82	92,60
BEDII31_02_MT_04	II	0,187	B.D.L.	0,006	0,152	0,183	N.D.	70,80	B.D.L.	B.D.L.	N.D.	N.D.	B.D.L.	B.D.L.	N.D.	20,68	92,08
BEDII31_02_MT_05	II	0,065	B.D.L.	B.D.L.	0,020	0,178	N.D.	71,26	B.D.L.	B.D.L.	N.D.	N.D.	N.D.	N.D.	N.D.	20,60	92,15
BEDII31_02_MT_06	II	0,067	B.D.L.	0,013	B.D.L.	0,163	B.D.L.	71,15	B.D.L.	0,027	N.D.	B.D.L.	N.D.	B.D.L.	N.D.	20,58	92,08
BEDII31_03_MT_01	I	0,403	B.D.L.	N.D.	0,193	0,233	N.D.	70,47	B.D.L.	0,035	N.D.	N.D.	N.D.	B.D.L.	B.D.L.	20,83	92,22
BEDII31_03_MT_02	I	0,056	0,021	0,005	B.D.L.	0,217	N.D.	71,58	B.D.L.	B.D.L.	B.D.L.	B.D.L.	B.D.L.	B.D.L.	B.D.L.	20,75	92,82
BEDII31_03_MT_03	I	0,052	B.D.L.	N.D.	0,022	0,231	B.D.L.	71,48	B.D.L.	B.D.L.	N.D.	N.D.	B.D.L.	B.D.L.	B.D.L.	20,70	92,59
BEDII31_03_MT_04	I	0,061	B.D.L.	B.D.L.	0,046	0,221	N.D.	71,17	B.D.L.	B.D.L.	B.D.L.	B.D.L.	B.D.L.	B.D.L.	B.D.L.	20,66	92,38
BEDII31_03_MT_05	I	0,043	B.D.L.	0,008	0,023	0,209	0,027	71,23	B.D.L.	B.D.L.	N.D.	B.D.L.	N.D.	B.D.L.	B.D.L.	20,61	92,24
BEDII31_03_MT_06	I	0,049	B.D.L.	0,013	B.D.L.	0,217	B.D.L.	71,35	B.D.L.	B.D.L.	N.D.	N.D.	N.D.	B.D.L.	B.D.L.	20,64	92,36
BEDII31_03_MT_07	I	0,046	B.D.L.	0,007	B.D.L.	0,212	B.D.L.	71,06	N.D.	N.D.	B.D.L.	B.D.L.	N.D.	0,037	B.D.L.	20,56	92,05
BEDII31_03_MT_08	I	0,079	B.D.L.	0,004	0,018	0,228	B.D.L.	71,32	N.D.	B.D.L.	N.D.	B.D.L.	N.D.	B.D.L.	B.D.L.	20,66	92,40
BEDII31_03_MT_09	II	0,070	0,034	B.D.L.	0,036	0,211	0,030	71,30	N.D.	B.D.L.	N.D.	N.D.	N.D.	B.D.L.	B.D.L.	20,68	92,39
BEDII31_03_MT_10	II	0,066	B.D.L.	B.D.L.	0,021	0,219	B.D.L.	71,20	B.D.L.	B.D.L.	N.D.	B.D.L.	B.D.L.	B.D.L.	N.D.	20,62	92,27
BEDII31_03_MT_11	II	0,073	B.D.L.	B.D.L.	B.D.L.	0,217	B.D.L.	71,09	B.D.L.	B.D.L.	N.D.	N.D.	B.D.L.	B.D.L.	B.D.L.	20,57	92,05
BEDII31_03_MT_12	II	0,054	B.D.L.	0,012	B.D.L.	0,223	0,023	70,89	B.D.L.	B.D.L.	B.D.L.	N.D.	B.D.L.	B.D.L.	B.D.L.	20,54	91,89
AUT29_01_MT_01	III	0,093	B.D.L.	N.D.	0,026	0,113	B.D.L.	71,05	B.D.L.	B.D.L.	B.D.L.	N.D.	N.D.	B.D.L.	B.D.L.	20,56	92,01
AUT29_01_MT_02	III	0,226	0,603	B.D.L.	0,026	0,119	0,257	69,30	B.D.L.	0,259	N.D.	B.D.L.	N.D.	0,044	0,037	21,13	92,06

AUT29_01_MT_03	III	0,058	B.D.L.	B.D.L.	B.D.L.	0,108	B.D.L.	71,11	B.D.L.	B.D.L.	N.D.	N.D.	N.D.	B.D.L.	B.D.L.	20,51	91,85
AUT29_01_MT_04	III	0,203	0,442	0,012	B.D.L.	0,112	0,162	69,31	B.D.L.	0,242	B.D.L.	N.D.	N.D.	B.D.L.	0,042	20,86	91,44
AUT29_01_MT_05	III	0,068	B.D.L.	B.D.L.	B.D.L.	0,111	B.D.L.	71,07	B.D.L.	B.D.L.	B.D.L.	B.D.L.	B.D.L.	B.D.L.	N.D.	20,52	91,88
AUT29_01_MT_06	III	0,057	B.D.L.	B.D.L.	B.D.L.	0,116	B.D.L.	70,86	N.D.	B.D.L.	B.D.L.	N.D.	B.D.L.	B.D.L.	B.D.L.	20,48	91,70
AUT29_01_MT_07	III	0,045	B.D.L.	B.D.L.	B.D.L.	0,103	B.D.L.	71,14	B.D.L.	B.D.L.	B.D.L.	B.D.L.	B.D.L.	0,037	B.D.L.	20,54	92,02
AUT29_01_MT_08	III	0,077	0,108	N.D.	B.D.L.	0,113	0,049	70,44	N.D.	0,036	B.D.L.	N.D.	B.D.L.	0,087	B.D.L.	20,53	91,54
AUT29_01_MT_09	IV	0,283	0,398	B.D.L.	0,035	0,116	0,149	69,69	B.D.L.	0,097	N.D.	N.D.	N.D.	0,075	0,103	20,93	91,93
AUT29_01_MT_10	IV	0,070	B.D.L.	B.D.L.	B.D.L.	0,110	B.D.L.	70,81	B.D.L.	B.D.L.	B.D.L.	N.D.	B.D.L.	0,044	B.D.L.	20,46	91,62
AUT29_01_MT_11	IV	0,098	0,026	B.D.L.	B.D.L.	0,102	0,017	70,61	B.D.L.	B.D.L.	N.D.	B.D.L.	N.D.	0,044	B.D.L.	20,44	91,41
AUT29_01_MT_12	IV	0,047	B.D.L.	B.D.L.	B.D.L.	0,086	B.D.L.	70,96	B.D.L.	B.D.L.	N.D.	B.D.L.	B.D.L.	0,041	B.D.L.	20,49	91,82
AUT29_02_MT_01	III	0,119	B.D.L.	N.D.	B.D.L.	0,083	B.D.L.	71,29	B.D.L.	B.D.L.	B.D.L.	N.D.	B.D.L.	0,150	B.D.L.	20,67	92,44
AUT29_02_MT_02	III	0,124	B.D.L.	B.D.L.	B.D.L.	0,094	B.D.L.	71,08	B.D.L.	B.D.L.	N.D.	B.D.L.	N.D.	0,165	B.D.L.	20,65	92,27
AUT29_02_MT_03	III	0,093	B.D.L.	B.D.L.	B.D.L.	0,097	N.D.	71,68	B.D.L.	B.D.L.	N.D.	B.D.L.	N.D.	0,056	B.D.L.	20,73	92,74
AUT29_02_MT_04	III	0,095	B.D.L.	B.D.L.	B.D.L.	0,089	B.D.L.	71,26	B.D.L.	B.D.L.	B.D.L.	B.D.L.	N.D.	0,101	B.D.L.	20,65	92,35
AUT29_02_MT_05	III	0,076	B.D.L.	B.D.L.	0,021	0,085	B.D.L.	71,40	B.D.L.	B.D.L.	N.D.	B.D.L.	B.D.L.	0,087	0,017	20,63	92,38
AUT29_02_MT_06	III	0,060	0,025	N.D.	B.D.L.	0,092	B.D.L.	70,84	B.D.L.	N.D.	B.D.L.	B.D.L.	B.D.L.	0,108	B.D.L.	20,49	91,71
AUT29_02_MT_07	III	0,101	B.D.L.	B.D.L.	B.D.L.	0,090	B.D.L.	70,86	N.D.	B.D.L.	B.D.L.	N.D.	N.D.	0,286	0,034	20,57	92,00
AUT29_02_MT_08	III	0,097	B.D.L.	B.D.L.	0,026	0,086	B.D.L.	70,94	B.D.L.	B.D.L.	N.D.	N.D.	B.D.L.	B.D.L.	B.D.L.	20,53	91,84
AUT29_02_MT_09	III	0,040	B.D.L.	N.D.	B.D.L.	0,088	N.D.	71,55	B.D.L.	B.D.L.	N.D.	B.D.L.	N.D.	0,051	B.D.L.	20,63	92,43
AUT29_02_MT_10	III	0,065	B.D.L.	B.D.L.	0,038	0,083	0,018	71,28	B.D.L.	B.D.L.	B.D.L.	N.D.	B.D.L.	0,054	0,024	20,60	92,20
AUT29_03_MT_01	III	0,070	B.D.L.	0,014	B.D.L.	0,097	B.D.L.	70,99	N.D.	B.D.L.	B.D.L.	B.D.L.	B.D.L.	0,120	B.D.L.	20,54	91,95
AUT29_03_MT_02	III	0,120	B.D.L.	N.D.	0,045	0,102	B.D.L.	71,27	B.D.L.	B.D.L.	N.D.	N.D.	B.D.L.	0,069	B.D.L.	20,66	92,35
AUT29_03_MT_03	III	0,056	B.D.L.	B.D.L.	B.D.L.	0,091	B.D.L.	71,34	B.D.L.	N.D.	B.D.L.	B.D.L.	B.D.L.	0,099	B.D.L.	20,62	92,38
AUT29_03_MT_04	III	0,078	B.D.L.	B.D.L.	0,026	0,084	B.D.L.	71,16	B.D.L.	B.D.L.	N.D.	N.D.	B.D.L.	0,046	B.D.L.	20,56	92,03
AUT29_03_MT_05	III	0,050	0,032	N.D.	B.D.L.	0,091	0,016	71,10	B.D.L.	N.D.	N.D.	B.D.L.	B.D.L.	0,047	0,024	20,54	91,96
AUT29_03_MT_06	III	0,026	B.D.L.	B.D.L.	B.D.L.	0,080	B.D.L.	70,98	B.D.L.	B.D.L.	N.D.	B.D.L.	B.D.L.	0,088	B.D.L.	20,47	91,72

AUT29_04_MT_01	IV	0,085	B.D.L.	B.D.L.	B.D.L.	0,082	B.D.L.	71,02	N.D.	N.D.	N.D.	B.D.L.	B.D.L.	0,045	B.D.L.	20,52	91,83
AUT29_04_MT_02	IV	0,071	B.D.L.	B.D.L.	B.D.L.	0,079	N.D.	71,31	B.D.L.	B.D.L.	N.D.	B.D.L.	N.D.	B.D.L.	B.D.L.	20,58	92,12
AUT29_04_MT_03	IV	0,058	0,019	B.D.L.	B.D.L.	0,070	B.D.L.	72,35	N.D.	B.D.L.	N.D.	B.D.L.	N.D.	B.D.L.	B.D.L.	20,87	93,48
AUT29_04_MT_04	IV	0,050	0,040	B.D.L.	B.D.L.	0,078	B.D.L.	72,42	N.D.	B.D.L.	B.D.L.	B.D.L.	B.D.L.	B.D.L.	B.D.L.	20,92	93,65
AUT29_04_MT_05	IV	0,073	0,044	B.D.L.	B.D.L.	0,073	B.D.L.	71,40	B.D.L.	B.D.L.	N.D.	N.D.	B.D.L.	B.D.L.	0,027	20,65	92,36
AUT29_05_MT_01	III	0,112	B.D.L.	B.D.L.	B.D.L.	0,094	B.D.L.	70,16	B.D.L.	B.D.L.	B.D.L.	B.D.L.	B.D.L.	B.D.L.	B.D.L.	20,34	90,96
AUT29_05_MT_02	III	0,102	B.D.L.	B.D.L.	B.D.L.	0,095	N.D.	70,89	B.D.L.	B.D.L.	N.D.	N.D.	B.D.L.	N.D.	N.D.	20,48	91,65
AUT29_05_MT_03	III	0,093	B.D.L.	N.D.	B.D.L.	0,095	B.D.L.	70,80	N.D.	B.D.L.	N.D.	N.D.	N.D.	B.D.L.	N.D.	20,45	91,49
AUT29_05_MT_04	III	0,145	B.D.L.	B.D.L.	0,021	0,088	B.D.L.	70,61	B.D.L.	0,033	B.D.L.	B.D.L.	B.D.L.	B.D.L.	B.D.L.	20,48	91,50
AUT29_05_MT_05	III	0,239	0,022	B.D.L.	0,729	0,112	B.D.L.	69,16	B.D.L.	0,033	B.D.L.	N.D.	B.D.L.	B.D.L.	B.D.L.	20,64	91,01
AUT29_06_MT_01	III	0,099	B.D.L.	N.D.	B.D.L.	0,099	B.D.L.	70,79	B.D.L.	B.D.L.	N.D.	B.D.L.	N.D.	0,077	B.D.L.	20,47	91,59
AUT29_06_MT_02	III	0,085	B.D.L.	N.D.	B.D.L.	0,109	B.D.L.	70,93	N.D.	B.D.L.	B.D.L.	B.D.L.	B.D.L.	0,082	B.D.L.	20,53	91,85
AUT29_06_MT_03	III	0,027	B.D.L.	B.D.L.	B.D.L.	0,105	B.D.L.	70,83	B.D.L.	B.D.L.	N.D.	N.D.	N.D.	B.D.L.	B.D.L.	20,40	91,45
AUT29_06_MT_04	III	0,040	B.D.L.	B.D.L.	B.D.L.	0,120	N.D.	70,85	B.D.L.	N.D.	B.D.L.	N.D.	N.D.	0,061	B.D.L.	20,45	91,60
AUT29_06_MT_05	III	0,061	B.D.L.	B.D.L.	B.D.L.	0,119	B.D.L.	71,20	N.D.	B.D.L.	B.D.L.	N.D.	B.D.L.	0,039	B.D.L.	20,57	92,06
AUT29_07_MT_01	III	0,080	B.D.L.	N.D.	0,060	0,139	B.D.L.	71,10	B.D.L.	0,045	B.D.L.	B.D.L.	N.D.	0,064	B.D.L.	20,63	92,23
AUT29_07_MT_02	III	0,146	0,022	0,012	0,022	0,129	B.D.L.	70,57	B.D.L.	0,079	B.D.L.	N.D.	B.D.L.	0,065	B.D.L.	20,55	91,67
AUT29_07_MT_03	III	0,067	B.D.L.	B.D.L.	B.D.L.	0,134	N.D.	70,78	B.D.L.	0,033	B.D.L.	B.D.L.	N.D.	0,039	B.D.L.	20,47	91,61
AUT29_07_MT_04	III	0,094	0,019	B.D.L.	B.D.L.	0,124	B.D.L.	71,04	0,057	0,030	B.D.L.	B.D.L.	B.D.L.	0,063	B.D.L.	20,61	92,17
AUT29_07_MT_05	III	0,219	0,203	B.D.L.	0,038	0,119	0,055	70,13	B.D.L.	0,108	B.D.L.	B.D.L.	B.D.L.	0,080	0,064	20,76	91,88
AUT29_07_MT_06	III	0,105	B.D.L.	B.D.L.	0,037	0,128	B.D.L.	71,12	B.D.L.	0,040	N.D.	N.D.	N.D.	0,066	B.D.L.	20,63	92,19
AUT29_07_MT_07	III	0,080	B.D.L.	B.D.L.	B.D.L.	0,112	B.D.L.	71,16	N.D.	0,031	B.D.L.	B.D.L.	B.D.L.	B.D.L.	B.D.L.	20,58	92,09
AUT29_08_MT_01	III	0,082	B.D.L.	N.D.	B.D.L.	0,123	N.D.	71,17	B.D.L.	B.D.L.	N.D.	B.D.L.	B.D.L.	0,051	B.D.L.	20,59	92,12
AUT29_08_MT_02	III	0,088	0,019	N.D.	0,294	0,118	B.D.L.	70,73	B.D.L.	B.D.L.	B.D.L.	N.D.	N.D.	0,057	B.D.L.	20,66	92,05
AUT29_08_MT_03	III	0,047	B.D.L.	B.D.L.	B.D.L.	0,122	N.D.	71,07	N.D.	B.D.L.	N.D.	N.D.	N.D.	0,054	B.D.L.	20,51	91,84
AUT29_08_MT_04	III	0,087	B.D.L.	0,015	B.D.L.	0,101	N.D.	71,16	B.D.L.	B.D.L.	N.D.	B.D.L.	B.D.L.	0,050	B.D.L.	20,60	92,17

AUT29_08_MT_05	III	0,056	B.D.L.	B.D.L.	B.D.L.	0,111	0,018	71,21	B.D.L.	B.D.L.	N.D.	B.D.L.	N.D.	0,051	B.D.L.	20,58	92,12
AUT29_08_MT_06	III	0,048	0,045	0,014	B.D.L.	0,108	0,033	71,23	B.D.L.	B.D.L.	B.D.L.	B.D.L.	B.D.L.	0,075	B.D.L.	20,64	92,29
BED13_01_MT_01	IV	B.D.L.	B.D.L.	N.D.	B.D.L.	B.D.L.	N.D.	71,43	B.D.L.	B.D.L.	N.D.	B.D.L.	B.D.L.	0,070	B.D.L.	20,56	92,19
BED13_01_MT_02	IV	B.D.L.	B.D.L.	N.D.	N.D.	0,028	N.D.	71,09	B.D.L.	B.D.L.	N.D.	N.D.	N.D.	0,075	B.D.L.	20,46	91,73
BED13_01_MT_03	IV	0,025	0,170	B.D.L.	N.D.	0,042	0,103	70,94	B.D.L.	0,036	N.D.	B.D.L.	B.D.L.	0,057	0,020	20,66	92,09
BED13_01_MT_04	IV	B.D.L.	B.D.L.	B.D.L.	B.D.L.	0,028	B.D.L.	71,39	N.D.	B.D.L.	N.D.	B.D.L.	N.D.	0,049	B.D.L.	20,53	92,07
BED13_01_MT_05	IV	0,026	B.D.L.	B.D.L.	N.D.	0,032	B.D.L.	70,98	B.D.L.	N.D.	N.D.	B.D.L.	B.D.L.	0,064	0,023	20,44	91,66
BED13_01_MT_06	IV	0,025	0,055	B.D.L.	N.D.	0,029	N.D.	71,06	N.D.	B.D.L.	B.D.L.	B.D.L.	N.D.	0,065	B.D.L.	20,51	91,83
BED13_01_MT_07	IV	0,026	B.D.L.	B.D.L.	N.D.	0,028	0,033	71,23	N.D.	B.D.L.	N.D.	N.D.	B.D.L.	0,081	B.D.L.	20,51	91,96
BED13_02_MT_01	IV	0,026	B.D.L.	B.D.L.	N.D.	B.D.L.	B.D.L.	71,32	B.D.L.	B.D.L.	B.D.L.	N.D.	N.D.	0,059	B.D.L.	20,51	91,99
BED13_02_MT_02	IV	B.D.L.	0,038	B.D.L.	N.D.	B.D.L.	0,036	71,31	B.D.L.	B.D.L.	B.D.L.	B.D.L.	N.D.	B.D.L.	B.D.L.	20,54	92,05
BED13_02_MT_03	IV	N.D.	B.D.L.	B.D.L.	N.D.	B.D.L.	B.D.L.	71,30	B.D.L.	N.D.	B.D.L.	N.D.	N.D.	0,055	N.D.	20,48	91,93
BED13_02_MT_04	IV	B.D.L.	0,041	B.D.L.	N.D.	0,029	0,031	71,34	B.D.L.	B.D.L.	B.D.L.	B.D.L.	N.D.	0,065	B.D.L.	20,57	92,17
BED13_02_MT_05	IV	B.D.L.	B.D.L.	N.D.	B.D.L.	B.D.L.	B.D.L.	71,33	B.D.L.	N.D.	N.D.	N.D.	N.D.	0,047	B.D.L.	20,49	91,94
BED13_02_MT_06	IV	B.D.L.	1,215	B.D.L.	B.D.L.	B.D.L.	0,860	67,83	B.D.L.	0,477	N.D.	B.D.L.	B.D.L.	0,102	0,021	21,56	92,20
BED13_02_MT_06	IV	0,035	2,803	B.D.L.	B.D.L.	0,030	1,927	62,96	N.D.	0,822	N.D.	B.D.L.	B.D.L.	0,083	B.D.L.	22,64	91,36
BED13_03_MT_01	IV	B.D.L.	0,021	B.D.L.	N.D.	0,030	B.D.L.	71,07	N.D.	N.D.	N.D.	B.D.L.	N.D.	B.D.L.	B.D.L.	20,44	91,65
BED13_03_MT_02	IV	0,019	0,020	B.D.L.	N.D.	0,042	0,130	70,77	0,056	B.D.L.	B.D.L.	B.D.L.	B.D.L.	0,084	0,038	20,46	91,69
BED13_03_MT_03	IV	B.D.L.	B.D.L.	B.D.L.	N.D.	0,036	0,117	70,10	B.D.L.	B.D.L.	B.D.L.	N.D.	N.D.	0,094	0,074	20,24	90,75
BED13_03_MT_04	IV	B.D.L.	0,032	B.D.L.	B.D.L.	0,028	0,017	71,29	N.D.	N.D.	B.D.L.	B.D.L.	B.D.L.	0,073	B.D.L.	20,54	92,07
BED13_03_MT_05	IV	B.D.L.	0,020	B.D.L.	N.D.	0,028	0,034	70,88	B.D.L.	B.D.L.	N.D.	B.D.L.	N.D.	0,057	0,025	20,41	91,52
BED13_03_MT_06	IV	0,021	0,019	N.D.	N.D.	0,029	0,018	71,17	B.D.L.	B.D.L.	B.D.L.	N.D.	B.D.L.	0,054	B.D.L.	20,51	91,99
BED13_03_MT_07	IV	B.D.L.	B.D.L.	B.D.L.	B.D.L.	0,031	B.D.L.	71,19	N.D.	B.D.L.	N.D.	N.D.	B.D.L.	0,058	B.D.L.	20,46	91,81
BED13_03_MT_08	IV	0,024	B.D.L.	N.D.	N.D.	0,040	N.D.	71,05	N.D.	B.D.L.	N.D.	B.D.L.	N.D.	0,039	B.D.L.	20,45	91,68
BED13_04_MT_01	IV	0,048	0,037	B.D.L.	B.D.L.	0,028	B.D.L.	70,68	B.D.L.	0,039	N.D.	B.D.L.	N.D.	B.D.L.	B.D.L.	20,40	91,31
BED13_04_MT_02	IV	B.D.L.	N.D.	B.D.L.	N.D.	0,035	B.D.L.	71,01	B.D.L.	B.D.L.	B.D.L.	B.D.L.	B.D.L.	N.D.	N.D.	20,40	91,56

BED13_04_MT_03	IV	B.D.L.	B.D.L.	N.D.	N.D.	0,027	N.D.	70,77	B.D.L.	N.D.	B.D.L.	N.D.	N.D.	B.D.L.	N.D.	20,33	91,23
BED13_04_MT_04	IV	B.D.L.	B.D.L.	B.D.L.	N.D.	B.D.L.	B.D.L.	71,00	B.D.L.	B.D.L.	B.D.L.	N.D.	B.D.L.	B.D.L.	B.D.L.	20,41	91,58
BED13_04_MT_05	IV	B.D.L.	0,194	B.D.L.	B.D.L.	0,033	0,196	70,62	B.D.L.	0,029	B.D.L.	B.D.L.	B.D.L.	0,086	B.D.L.	20,62	91,84
BED13_04_MT_06	IV	B.D.L.	B.D.L.	B.D.L.	B.D.L.	0,023	0,030	71,04	N.D.	B.D.L.	N.D.	B.D.L.	N.D.	B.D.L.	B.D.L.	20,44	91,65
BED13_04_MT_07	IV	B.D.L.	B.D.L.	B.D.L.	B.D.L.	B.D.L.	0,017	71,30	N.D.	B.D.L.	N.D.	B.D.L.	N.D.	0,048	B.D.L.	20,49	91,95
BED13_04_MT_08	IV	B.D.L.	B.D.L.	B.D.L.	B.D.L.	0,026	N.D.	70,93	B.D.L.	B.D.L.	B.D.L.	N.D.	B.D.L.	0,068	B.D.L.	20,41	91,56
BED13_05_MT_01	IV	B.D.L.	B.D.L.	B.D.L.	N.D.	0,025	N.D.	71,46	B.D.L.	N.D.	B.D.L.	B.D.L.	N.D.	B.D.L.	B.D.L.	20,53	92,10
BED13_05_MT_02	IV	B.D.L.	0,026	N.D.	B.D.L.	B.D.L.	B.D.L.	70,94	B.D.L.	N.D.	B.D.L.	0,082	N.D.	B.D.L.	B.D.L.	20,41	91,54
BED13_05_MT_03	IV	B.D.L.	B.D.L.	B.D.L.	N.D.	0,028	0,075	71,17	B.D.L.	N.D.	N.D.	B.D.L.	B.D.L.	0,063	B.D.L.	20,51	91,98
BED13_05_MT_04	IV	B.D.L.	B.D.L.	B.D.L.	B.D.L.	B.D.L.	0,045	70,99	B.D.L.	N.D.	N.D.	B.D.L.	N.D.	0,050	B.D.L.	20,41	91,59
BED13_05_MT_05	IV	0,019	B.D.L.	B.D.L.	N.D.	B.D.L.	0,049	71,09	B.D.L.	N.D.	N.D.	B.D.L.	N.D.	0,081	B.D.L.	20,48	91,82
BED13_05_MT_06	IV	B.D.L.	B.D.L.	B.D.L.	N.D.	B.D.L.	B.D.L.	71,16	B.D.L.	B.D.L.	B.D.L.	B.D.L.	B.D.L.	B.D.L.	B.D.L.	20,45	91,76
BED13_05_MT_07	IV	B.D.L.	0,024	N.D.	N.D.	0,023	B.D.L.	71,00	N.D.	N.D.	N.D.	B.D.L.	B.D.L.	0,062	0,022	20,44	91,66
BED13_05_MT_08	IV	0,022	0,040	B.D.L.	N.D.	0,030	B.D.L.	70,79	B.D.L.	B.D.L.	N.D.	B.D.L.	B.D.L.	0,042	0,048	20,41	91,45
BED13_05_MT_09	IV	0,024	B.D.L.	B.D.L.	N.D.	0,034	B.D.L.	71,05	B.D.L.	B.D.L.	B.D.L.	B.D.L.	B.D.L.	0,101	B.D.L.	20,47	91,81
BED13_05_MT_10	IV	B.D.L.	B.D.L.	B.D.L.	N.D.	0,030	N.D.	71,09	B.D.L.	B.D.L.	N.D.	B.D.L.	N.D.	0,052	B.D.L.	20,45	91,74
BED13_06_MT_01	IV	B.D.L.	0,201	B.D.L.	N.D.	B.D.L.	0,045	70,79	N.D.	0,026	N.D.	B.D.L.	N.D.	0,075	N.D.	20,60	91,78
BED13_06_MT_02	IV	0,038	0,091	N.D.	N.D.	N.D.	0,038	71,41	N.D.	0,030	B.D.L.	B.D.L.	N.D.	0,151	0,018	20,71	92,55
BED13_06_MT_03	IV	0,026	0,399	B.D.L.	N.D.	B.D.L.	0,077	70,41	N.D.	0,104	N.D.	B.D.L.	N.D.	0,060	B.D.L.	20,78	91,87
BED13_06_MT_04	IV	0,038	0,315	B.D.L.	N.D.	B.D.L.	0,137	70,62	B.D.L.	0,113	N.D.	B.D.L.	N.D.	0,051	B.D.L.	20,79	92,13
BED13_06_MT_05	IV	B.D.L.	B.D.L.	B.D.L.	B.D.L.	0,026	N.D.	71,37	N.D.	B.D.L.	B.D.L.	N.D.	N.D.	0,052	B.D.L.	20,52	92,05
BED13_06_MT_06	IV	B.D.L.	0,045	N.D.	N.D.	B.D.L.	N.D.	71,66	N.D.	N.D.	N.D.	B.D.L.	B.D.L.	0,053	B.D.L.	20,63	92,45
BED13_07_MT_01	IV	B.D.L.	0,106	B.D.L.	B.D.L.	B.D.L.	B.D.L.	71,01	B.D.L.	N.D.	N.D.	B.D.L.	N.D.	0,110	B.D.L.	20,55	91,92
BED13_07_MT_02	IV	0,021	0,097	B.D.L.	B.D.L.	B.D.L.	0,016	71,01	B.D.L.	B.D.L.	N.D.	N.D.	N.D.	0,113	B.D.L.	20,54	91,84
BED13_07_MT_03	IV	0,027	0,083	B.D.L.	N.D.	B.D.L.	0,037	71,01	B.D.L.	B.D.L.	B.D.L.	B.D.L.	B.D.L.	0,095	B.D.L.	20,55	91,94
BED13_07_MT_04	IV	0,020	B.D.L.	B.D.L.	N.D.	B.D.L.	B.D.L.	71,16	N.D.	B.D.L.	B.D.L.	B.D.L.	B.D.L.	0,066	B.D.L.	20,48	91,86

BED13_07_MT_05	IV	B.D.L.	0,026	B.D.L.	N.D.	B.D.L.	0,057	70,85	B.D.L.	B.D.L.	N.D.	N.D.	N.D.	0,142	B.D.L.	20,43	91,57
BED13_07_MT_06	IV	B.D.L.	0,125	B.D.L.	N.D.	0,027	0,163	70,91	N.D.	B.D.L.	N.D.	B.D.L.	N.D.	0,096	0,020	20,61	92,03
BED13_07_MT_07	IV	B.D.L.	0,058	B.D.L.	B.D.L.	B.D.L.	B.D.L.	71,06	B.D.L.	B.D.L.	B.D.L.	B.D.L.	N.D.	0,055	0,029	20,50	91,81
AUT09_01_MT_01	III	0,057	B.D.L.	N.D.	0,021	0,120	B.D.L.	71,42	B.D.L.	N.D.	B.D.L.	N.D.	B.D.L.	0,110	B.D.L.	20,65	92,45
AUT09_01_MT_02	III	0,049	0,082	N.D.	B.D.L.	0,129	B.D.L.	69,24	B.D.L.	B.D.L.	B.D.L.	B.D.L.	B.D.L.	0,063	B.D.L.	20,09	89,73
AUT09_01_MT_03	III	0,052	0,020	B.D.L.	B.D.L.	0,121	N.D.	69,05	N.D.	N.D.	N.D.	B.D.L.	N.D.	0,054	B.D.L.	19,94	89,28
AUT09_01_MT_04	III	0,106	0,030	B.D.L.	0,022	0,122	B.D.L.	71,24	B.D.L.	B.D.L.	B.D.L.	N.D.	B.D.L.	0,068	0,021	20,65	92,30
AUT09_01_MT_05	III	0,083	0,052	B.D.L.	B.D.L.	0,117	B.D.L.	69,35	N.D.	B.D.L.	B.D.L.	N.D.	B.D.L.	B.D.L.	B.D.L.	20,10	89,83
AUT09_02_MT_01	III	B.D.L.	B.D.L.	B.D.L.	B.D.L.	0,137	B.D.L.	71,31	N.D.	0,024	N.D.	B.D.L.	B.D.L.	0,100	B.D.L.	20,60	92,29
AUT09_02_MT_02	III	B.D.L.	B.D.L.	N.D.	B.D.L.	0,161	B.D.L.	71,31	N.D.	B.D.L.	B.D.L.	B.D.L.	N.D.	0,093	0,016	20,60	92,31
AUT09_02_MT_03	III	0,072	B.D.L.	B.D.L.	0,028	0,147	N.D.	71,28	B.D.L.	B.D.L.	B.D.L.	N.D.	B.D.L.	0,235	0,017	20,70	92,59
AUT09_02_MT_04	III	B.D.L.	B.D.L.	N.D.	B.D.L.	0,149	B.D.L.	71,38	N.D.	B.D.L.	N.D.	N.D.	N.D.	0,113	B.D.L.	20,59	92,28
AUT09_02_MT_05	III	B.D.L.	B.D.L.	B.D.L.	B.D.L.	0,153	B.D.L.	71,13	B.D.L.	N.D.	N.D.	B.D.L.	B.D.L.	0,106	B.D.L.	20,52	92,02
AUT09_03_MT_01	III	0,780	2,220	B.D.L.	0,215	0,172	0,408	64,22	N.D.	0,399	B.D.L.	B.D.L.	B.D.L.	0,256	0,280	22,46	91,57
AUT09_03_MT_02	III	0,059	B.D.L.	B.D.L.	B.D.L.	0,133	B.D.L.	71,44	N.D.	B.D.L.	N.D.	B.D.L.	B.D.L.	0,101	B.D.L.	20,66	92,49
AUT09_03_MT_03	III	0,132	B.D.L.	B.D.L.	B.D.L.	0,150	B.D.L.	71,23	B.D.L.	B.D.L.	N.D.	N.D.	N.D.	0,076	B.D.L.	20,67	92,34
AUT09_03_MT_04	III	0,132	0,021	B.D.L.	B.D.L.	0,136	B.D.L.	71,17	N.D.	B.D.L.	B.D.L.	N.D.	N.D.	0,061	N.D.	20,64	92,23
AUT09_03_MT_05	III	0,104	N.D.	N.D.	B.D.L.	0,140	B.D.L.	71,38	B.D.L.	N.D.	B.D.L.	N.D.	N.D.	0,222	0,019	20,70	92,60
AUT09_04_MT_01	III	0,096	B.D.L.	B.D.L.	0,031	0,097	B.D.L.	71,27	B.D.L.	B.D.L.	B.D.L.	B.D.L.	N.D.	0,128	B.D.L.	20,65	92,35
AUT09_04_MT_02	III	0,101	B.D.L.	B.D.L.	0,020	0,096	N.D.	71,53	B.D.L.	B.D.L.	N.D.	N.D.	N.D.	0,061	B.D.L.	20,70	92,60
AUT09_04_MT_03	III	0,090	B.D.L.	B.D.L.	0,021	0,112	B.D.L.	71,68	N.D.	N.D.	B.D.L.	B.D.L.	B.D.L.	0,110	B.D.L.	20,76	92,89
AUT09_04_MT_04	III	0,089	B.D.L.	B.D.L.	B.D.L.	0,106	N.D.	71,33	B.D.L.	B.D.L.	N.D.	N.D.	B.D.L.	0,075	B.D.L.	20,64	92,34
AUT09_04_MT_05	III	0,102	0,041	B.D.L.	0,032	0,100	B.D.L.	70,97	B.D.L.	B.D.L.	N.D.	B.D.L.	B.D.L.	0,106	0,029	20,61	92,08

Tabla 2. Ablación láser en Magnetita

Sample				AUT09														AUT29	
Type				III	III	III	III	III	III	III	III	III	III	III	III	III	III	IV	III
Element	Units	Isotope	D.L.																
Fe	Wt%	57	EMPA	71,42	69,24	69,05	71,24	69,35	71,31	71,31	71,28	71,38	71,13	64,22	71,44	71,23	71,17	70,96	70,61
Na	ppm	23	21,6	B.D.L.	B.D.L.	B.D.L.	38,0	B.D.L.	39,0	B.D.L.	B.D.L.	B.D.L.	B.D.L.	B.D.L.	B.D.L.	25,3	B.D.L.	B.L.D	B.L.D
Mg	ppm	25	2,5	48,4	1790,0	519,0	525,0	968,0	1260,0	381,0	178,0	690,0	177,0	117,0	286,0	1357,0	186,0	50,1	185,0
Al	ppm	27	1,7	489,0	2570,0	1980,0	1800,0	2170,0	1180,0	899,0	775,0	960,0	743,0	466,0	991,0	1546,0	1262,0	366,4	821,0
Si	ppm	29	1976,2	B.D.L.	3300,0	B.D.L.	3900,0	6300,0	B.D.L.	B.D.L.	1560,0	3800,0	1650,0	1680,0	2930,0	5990,0	3000,0	B.L.D	B.L.D
P	ppm	31	9,8	16,0	41,0	56,0	36,0	51,0	25,0	B.D.L.	B.D.L.	B.D.L.	B.D.L.	B.D.L.	40,0	27,0	12,0	39,0	50,0
K	ppm	39	24,5	B.D.L.	68,0	177,0	168,0	393,0	506,0	B.D.L.	B.D.L.	B.D.L.	B.D.L.	B.D.L.	B.D.L.	88,2	21,0	B.L.D	B.L.D
Ca	ppm	44	289,7	B.D.L.	B.D.L.	B.D.L.	B.D.L.	B.D.L.	B.D.L.	B.D.L.	B.D.L.	B.D.L.	B.D.L.	B.D.L.	B.D.L.	944,0	B.D.L.	270,0	B.L.D
Sc	ppm	45	1,8	B.D.L.	2,3	B.D.L.	B.D.L.	B.D.L.	B.D.L.	2,0	1,9	4,2	2,0	B.D.L.	1,8	6,0	B.D.L.	B.L.D	B.L.D
Ti	ppm	49	13,4	181,0	2700,0	537,0	620,0	301,0	487,0	950,0	292,0	420,0	365,0	164,0	538,0	315,0	129,0	286,0	722,0
V	ppm	51	1,4	1090,0	1070,0	1068,0	1100,0	1049,0	1298,0	1327,0	1311,0	1329,0	1338,0	1158,0	1307,0	1294,0	1261,0	597,0	975,0
Cr	ppm	53	8,4	B.D.L.	B.D.L.	B.D.L.	B.D.L.	B.D.L.	B.D.L.	B.D.L.	B.D.L.	B.D.L.	B.D.L.	B.D.L.	B.D.L.	B.D.L.	B.D.L.	B.D.L.	B.D.L.
Mn	ppm	55	1,4	58,2	46,5	55,4	65,6	62,5	52,2	90,0	58,8	61,9	62,7	47,0	67,6	83,7	59,9	109,7	127,0
Co	ppm	59	0,6	41,2	37,8	41,7	44,6	39,1	26,6	27,0	28,8	27,2	27,1	24,5	29,6	28,1	27,7	22,5	21,5
Ni	ppm	60	0,8	34,4	33,1	35,4	36,5	35,7	161,8	80,5	49,4	42,0	38,7	94,0	61,4	32,3	28,3	157,5	98,4
Cu	ppm	63	0,7	B.D.L.	B.D.L.	1,8	B.D.L.	B.D.L.	0,8	B.D.L.	55,0	B.D.L.	73,0	B.D.L.	B.D.L.	59,0	63,0	B.L.D	B.L.D
Zn	ppm	66	6,4	B.D.L.	B.D.L.	B.D.L.	B.D.L.	B.D.L.	5,9	6,6	B.D.L.	B.D.L.	B.D.L.	B.D.L.	B.D.L.	B.D.L.	B.D.L.	B.L.D	B.L.D
Ga	ppm	69	0,1	25,7	32,5	36,9	32,1	30,6	29,4	30,2	27,6	29,4	28,6	25,3	29,7	32,8	26,5	23,7	28,2
Ge	ppm	72	2,0	37,7	36,6	37,1	39,0	35,7	37,2	36,6	33,6	37,9	37,5	33,6	38,1	38,3	31,9	38,2	38,0
Sr	ppm	88	0,1	B.D.L.	0,6	0,4	0,8	0,5	0,3	2,9	B.D.L.	0,9	1,2	B.D.L.	0,4	1,2	B.D.L.	B.L.D	B.L.D
Y	ppm	89	0,1	B.D.L.	1,6	1,0	0,8	1,1	0,3	0,3	0,2	0,7	0,2	B.D.L.	0,3	3,0	0,1	B.L.D	B.L.D
Nb	ppm	93	0,1	B.L.D	B.L.D	B.L.D	B.L.D	B.L.D	B.L.D	B.L.D	B.L.D	B.L.D	B.L.D	B.L.D	B.L.D	B.L.D	B.L.D	B.L.D	B.L.D
Mo	ppm	95	0,6	B.L.D	B.L.D	B.L.D	B.L.D	B.L.D	B.L.D	B.L.D	B.L.D	B.L.D	B.L.D	B.L.D	B.L.D	B.L.D	B.L.D	B.L.D	B.L.D
Sn	ppm	118	0,8	B.D.L.	1,5	B.D.L.	1,0	1,2	B.D.L.	1,3	B.D.L.	0,9	B.D.L.	B.D.L.	0,7	0,6	0,9	B.L.D	0,8
Sb	ppm	121	0,8	B.D.L.	B.D.L.	B.D.L.	B.D.L.	B.D.L.	B.D.L.	B.D.L.	B.D.L.	B.D.L.	B.D.L.	B.D.L.	B.D.L.	B.D.L.	B.D.L.	B.D.L.	B.D.L.
Ba	ppm	138	0,1	B.D.L.	B.D.L.	B.D.L.	B.D.L.	1,6	1,7	2,8	B.D.L.	B.D.L.	B.D.L.	B.D.L.	B.D.L.	B.D.L.	B.D.L.	B.L.D	B.L.D

Sample				AUT 29															
Type				III	III	III	III	III	III	III	III	III	III	III	III	III	III	III	III
Element	Units	Isotope	D.L.																
Fe	Wt%	57	EMPA	71,14	69,31	71,11	69,30	71,05	70,79	70,93	70,83	70,85	71,20	71,10	70,57	70,78	71,04	70,13	71,12
Na	ppm	23	21,6	B.L.D	2690,0	103,0	113,0	140,3	50,0	294,0	530,0	34,0	62,0	61,5	61,0	214,0	280,0	70,6	58,0
Mg	ppm	25	2,5	176,0	2700,0	1437,0	1570,0	2870,0	188,0	1470,0	1950,0	664,0	342,0	579,0	542,0	674,0	583,0	1780,0	1140,0
Al	ppm	27	1,7	863,0	3320,0	2130,0	2210,0	2440,0	964,0	2460,0	2770,0	927,0	1270,0	2110,0	1890,0	1944,0	1746,0	1858,0	2400,0
Si	ppm	29	1976,2	B.L.D	B.L.D	B.L.D	B.L.D	6460,0	B.L.D	B.L.D	3370,0	2190,0	B.L.D	6350,0	4900,0	3700,0	2180,0	4000,0	2660,0
P	ppm	31	9,8	28,0	47,0	39,0	41,0	25,0	B.L.D	B.L.D	B.L.D	B.L.D	B.L.D	B.L.D	B.L.D	B.L.D	16,0	B.L.D	B.L.D
K	ppm	39	24,5	B.L.D	568,0	178,0	54,0	241,0	33,0	209,0	323,0	158,0	37,6	B.L.D	B.L.D	94,0	111,0	330,0	235,0
Ca	ppm	44	289,7	B.L.D	2120,0	771,0	405,0	2400,0	174,0	980,0	2300,0	460,0	B.L.D	B.L.D	B.L.D	B.L.D	B.L.D	1480,0	960,0
Sc	ppm	45	1,8	1,3	7,1	3,4	2,6	9,2	B.L.D	3,9	3,0	2,8	B.L.D	2,8	2,7	2,5	2,1	5,9	3,0
Ti	ppm	49	13,4	700,0	1090,0	814,0	1380,0	279,0	433,0	553,0	583,0	142,0	281,0	690,0	1240,0	1480,0	950,0	277,0	427,0
V	ppm	51	1,4	980,0	1013,0	994,0	978,0	1005,0	904,0	1021,0	1005,0	1035,0	1056,0	1214,0	1227,0	1197,0	1121,0	1099,0	1054,0
Cr	ppm	53	8,4	B.D.L.	B.D.L.	B.D.L.	B.D.L.	B.D.L.	B.D.L.	B.D.L.	B.D.L.	B.D.L.	B.D.L.	B.D.L.	B.D.L.	B.D.L.	B.D.L.	B.D.L.	B.D.L.
Mn	ppm	55	1,4	129,9	162,6	157,4	138,1	191,3	102,3	102,4	160,0	108,7	112,3	157,5	151,3	170,9	180,0	161,9	160,4
Co	ppm	59	0,6	24,0	28,9	29,9	30,9	30,7	27,0	28,2	30,0	26,7	29,8	26,7	26,9	27,0	25,4	25,9	24,2
Ni	ppm	60	0,8	76,9	63,2	55,7	55,6	54,5	143,0	80,2	59,8	53,5	53,3	57,0	57,4	55,3	58,8	55,4	58,7
Cu	ppm	63	0,7	0,4	5,0	1,2	1,0	0,6	B.L.D	0,9	85,0	B.L.D	1,1	B.L.D	B.L.D	B.L.D	1,0	B.L.D	B.L.D
Zn	ppm	66	6,4	5,5	10,5	5,5	10,5	10,1	B.L.D	B.L.D	8,9	B.L.D	B.L.D	10,6	B.L.D	12,9	13,2	8,8	B.L.D
Ga	ppm	69	0,1	27,3	26,6	26,8	27,6	27,0	24,6	25,8	26,9	24,3	27,2	32,2	30,7	31,6	31,3	28,7	27,3
Ge	ppm	72	2,0	38,5	39,0	38,9	36,9	37,8	39,0	39,2	38,3	37,9	38,5	38,0	36,6	36,8	37,1	36,1	35,1
Sr	ppm	88	0,1	B.L.D	5,8	1,0	0,9	3,1	0,1	3,0	8,2	1,2	1,0	1,2	1,7	2,4	4,2	1,5	1,1
Y	ppm	89	0,1	B.L.D	3,4	1,1	0,3	2,9	B.L.D	1,1	1,2	0,6	0,1	0,2	0,1	0,1	0,1	1,8	0,9
Nb	ppm	93	0,1	B.L.D	0,3	B.L.D	0,2	0,1	B.L.D	B.L.D	0,4	B.L.D	B.L.D	B.L.D	B.L.D	B.L.D	B.L.D	B.L.D	B.L.D
Mo	ppm	95	0,6	0,5	4,9	0,8	0,6	B.L.D	B.L.D	0,5	0,9	B.L.D	B.L.D	B.L.D	0,5	0,6	0,6	B.L.D	B.L.D
Sn	ppm	118	0,8	0,8	1,0	0,7	1,1	B.L.D	B.L.D	B.L.D	1,0	0,7	B.L.D	B.L.D	B.L.D	B.L.D	B.L.D	B.L.D	B.L.D
Sb	ppm	121	0,8	B.D.L.	B.D.L.	B.D.L.	B.D.L.	B.D.L.	B.D.L.	B.D.L.	B.D.L.	B.D.L.	B.D.L.	B.D.L.	B.D.L.	B.D.L.	B.D.L.	B.D.L.	B.D.L.
Ba	ppm	138	0,1	B.L.D	6,1	B.L.D	1,3	2,5	B.L.D	2,7	7,4	1,5	B.L.D	B.L.D	B.L.D	3,2	3,3	B.L.D	B.L.D

Sample										BED09									BED13
Type				III	III	III	III	III	III	IV	IV	IV	IV	IV	IV	IV	IV	IV	IV
Element	Units	Isotope	D.L.																
Fe	Wt%	57	EMPA	71,16	71,17	70,73	71,16	71,21	71,23	71,69	72,05	71,83	70,96	71,44	71,37	71,64	72,71	71,49	70,94
Na	ppm	23	21,6	B.L.D	B.L.D	B.L.D	23,0	100,0	83,7	142,0	B.D.L	B.D.L	119,0	113,0	82,0	B.D.L	30,1	38,9	339,0
Mg	ppm	25	2,5	250,0	127,7	337,0	401,0	2620,0	3020,0	176,0	46,3	28,7	1670,0	2680,0	670,0	31,6	36,9	11,5	4850,0
Al	ppm	27	1,7	959,0	806,0	1634,0	1506,0	2820,0	2276,0	1364,0	440,7	370,1	3370,0	1780,0	1050,0	437,0	261,0	94,9	233,0
Si	ppm	29	1976,2	1760,0	3950,0	2060,0	2000,0	4630,0	6430,0	B.D.L	B.D.L	B.D.L	2910,0	6200,0	6830,0	B.D.L	B.D.L	B.D.L	10500,0
P	ppm	31	9,8	24,0	B.L.D	B.L.D	B.L.D	B.L.D	B.L.D	B.D.L	B.D.L	11,0	B.D.L	60,0	59,0	21,0	B.D.L	B.D.L	94,0
K	ppm	39	24,5	B.L.D	B.L.D	58,4	43,0	253,0	482,0	155,0	B.D.L	B.D.L	122,0	82,0	233,0	B.D.L	B.D.L	58,7	1240,0
Ca	ppm	44	289,7	B.L.D	B.L.D	B.L.D	B.L.D	1410,0	2280,0	738,0	B.D.L	B.D.L	430,0	261,0	476,0	315,0	277,0	319,0	3740,0
Sc	ppm	45	1,8	B.L.D	B.L.D	2,3	2,1	6,8	9,1	B.D.L	B.D.L	B.D.L	B.D.L	B.D.L	B.D.L	B.D.L	B.D.L	B.D.L	B.L.D
Ti	ppm	49	13,4	176,0	479,0	364,0	228,0	429,0	285,0	498,0	238,0	151,0	268,0	256,0	262,0	164,0	172,0	73,0	B.L.D
V	ppm	51	1,4	1073,0	1073,0	999,0	1013,0	953,0	963,0	94,5	104,3	104,8	99,9	98,7	96,8	97,8	98,2	99,7	258,3
Cr	ppm	53	8,4	B.D.L.	B.D.L.	B.D.L.	B.D.L.	B.D.L.	B.D.L.	B.D.L.	B.D.L.	B.D.L.	B.D.L.	B.D.L.	B.D.L.	B.D.L.	B.D.L.	B.D.L.	B.D.L.
Mn	ppm	55	1,4	132,1	112,3	123,2	116,5	137,9	153,7	78,0	61,8	54,3	82,5	64,3	72,4	56,3	54,2	45,7	141,9
Co	ppm	59	0,6	25,1	23,1	22,3	23,1	20,8	23,5	25,4	13,8	12,5	13,4	13,7	12,7	12,1	13,0	9,2	34,0
Ni	ppm	60	0,8	55,6	103,1	56,4	57,7	59,0	54,8	88,0	58,4	73,9	22,9	20,6	82,1	78,3	100,6	104,4	41,3
Cu	ppm	63	0,7	35,0	B.L.D	B.L.D	233,0	42,0	2,0	193,0	B.D.L	B.D.L	B.D.L	2,8	22,0	B.D.L	52,4	37,1	B.L.D
Zn	ppm	66	6,4	8,0	B.L.D	8,1	9,4	9,1	6,5	B.D.L	B.D.L	B.D.L	13,9	8,6	10,6	B.D.L	B.D.L	B.D.L	13,6
Ga	ppm	69	0,1	27,0	25,5	31,1	27,4	29,1	29,5	26,3	19,9	19,2	27,9	21,5	22,0	21,1	20,9	19,2	13,4
Ge	ppm	72	2,0	34,8	39,5	37,8	36,1	39,1	35,9	36,9	36,0	36,3	39,1	37,3	38,5	40,1	39,5	39,3	36,1
Sr	ppm	88	0,1	B.L.D	B.L.D	0,4	0,6	1,5	2,9	0,8	B.D.L	B.D.L	4,1	2,5	1,7	B.D.L	B.D.L	0,1	14,3
Y	ppm	89	0,1	0,1	B.L.D	0,1	0,1	2,0	2,7	0,1	B.D.L	B.D.L	0,5	B.D.L	6,8	B.D.L	B.D.L	0,1	3,0
Nb	ppm	93	0,1	B.L.D	B.L.D	B.L.D	B.L.D	B.L.D	B.L.D	B.D.L	B.D.L	B.D.L	B.D.L	0,9	0,2	B.D.L	B.D.L	B.D.L	0,2
Mo	ppm	95	0,6	B.L.D	B.L.D	B.L.D	B.L.D	0,7	B.L.D	B.D.L	B.D.L	B.D.L	0,5	B.D.L	B.D.L	B.D.L	0,6	B.D.L	4,0
Sn	ppm	118	0,8	B.L.D	B.L.D	B.L.D	B.L.D	0,9	B.L.D	B.D.L	B.D.L	B.D.L	B.D.L	0,9	B.D.L	B.D.L	B.D.L	B.D.L	0,9
Sb	ppm	121	0,8	B.D.L.	B.D.L.	B.D.L.	B.D.L.	B.D.L.	B.D.L.	B.D.L.	B.D.L.	B.D.L.	B.D.L.	B.D.L.	B.D.L.	B.D.L.	B.D.L.	B.D.L.	5,6
Ba	ppm	138	0,1	B.L.D	B.L.D	B.L.D	B.L.D	2,0	3,2	B.D.L	B.D.L	B.D.L	3,5	2,6	2,8	B.D.L	B.D.L	1,4	12,2

Sample				BED 13															
Type				IV	IV	IV	IV	IV	IV	IV	IV	IV	IV	IV	IV	IV	IV	IV	IV
Element	Units	Isotope	D.L.																
Fe	Wt%	57	EMPA	71,39	70,98	71,06	71,23	71,32	71,31	71,30	71,34	71,33	67,83	71,07	70,77	70,10	71,29	70,88	71,17
Na	ppm	23	21,6	598,0	40,9	B.L.D	29,0	141,0	187,0	65,0	118,0	347,0	129,4	240,0	640,0	537,0	544,0	463,0	950,0
Mg	ppm	25	2,5	4230,0	1082,0	33,4	50,5	232,0	3430,0	1990,0	3360,0	3320,0	2820,0	960,0	4310,0	760,0	17400,0	615,0	2030,0
Al	ppm	27	1,7	265,0	197,8	173,6	166,2	206,0	250,0	341,0	245,0	259,0	222,0	171,0	237,0	157,0	900,0	124,8	203,0
Si	ppm	29	1976,2	8400,0	4540,0	3080,0	3330,0	3640,0	13700,0	8400,0	11800,0	10000,0	7990,0	1780,0	19300,0	5800,0	57900,0	3300,0	6000,0
P	ppm	31	9,8	26,0	25,0	B.L.D	B.L.D	B.L.D	62,0	34,0	62,0	68,0	19,0	91,0	196,0	110,0	183,0	137,0	82,0
K	ppm	39	24,5	486,0	138,4	37,6	B.L.D	74,0	168,0	68,0	75,3	290,0	105,5	227,0	400,0	333,0	312,0	368,0	776,0
Ca	ppm	44	289,7	3190,0	1300,0	B.L.D	B.L.D	B.L.D	3740,0	1760,0	3230,0	3050,0	2940,0	410,0	6500,0	840,0	3280,0	1280,0	2780,0
Sc	ppm	45	1,8	B.L.D	B.L.D	B.L.D	B.L.D	B.L.D	B.L.D	B.L.D	B.L.D	B.L.D	B.L.D	B.L.D	B.L.D	B.L.D	2,6	B.L.D	B.L.D
Ti	ppm	49	13,4	B.L.D	B.L.D	B.L.D	B.L.D	B.L.D	B.L.D	B.L.D	B.L.D	B.L.D	B.L.D	B.L.D	B.L.D	B.L.D	B.L.D	B.L.D	8,2
V	ppm	51	1,4	277,0	256,3	280,0	267,5	227,1	234,4	233,7	232,7	228,2	227,2	310,0	299,0	325,0	329,0	316,0	317,0
Cr	ppm	53	8,4	B.D.L.	B.D.L.	B.D.L.	B.D.L.	B.D.L.	B.D.L.	B.D.L.	B.D.L.	B.D.L.	B.D.L.	B.D.L.	B.D.L.	B.D.L.	B.D.L.	B.D.L.	B.D.L.
Mn	ppm	55	1,4	126,0	54,4	50,9	49,2	96,0	91,3	70,7	85,7	136,0	91,7	120,1	131,9	109,3	114,6	135,2	178,0
Co	ppm	59	0,6	60,0	22,5	21,1	20,8	30,6	31,1	28,8	30,8	34,8	31,0	18,9	23,3	18,2	86,0	16,0	23,1
Ni	ppm	60	0,8	44,2	40,3	45,4	40,8	43,1	42,3	49,7	44,7	44,1	42,8	57,9	35,8	38,1	75,9	38,6	42,3
Cu	ppm	63	0,7	1,0	0,7	B.L.D	B.L.D	B.L.D	B.L.D	1,2	B.L.D	0,8	B.L.D	1,0	2,5	2,9	9,4	2,1	2,9
Zn	ppm	66	6,4	13,5	B.L.D	B.L.D	6,1	8,6	9,2	B.L.D	7,0	10,9	B.L.D	9,5	10,6	12,9	14,7	13,1	15,8
Ga	ppm	69	0,1	14,4	12,6	12,7	11,6	14,1	14,1	13,0	13,6	13,4	14,0	13,0	13,8	13,6	17,4	13,1	15,8
Ge	ppm	72	2,0	38,9	36,7	36,8	37,5	36,6	38,2	37,2	39,4	37,7	40,1	35,2	32,8	36,9	38,6	40,4	39,4
Sr	ppm	88	0,1	14,5	7,8	0,6	0,6	2,0	11,8	6,5	9,9	13,3	10,3	3,3	10,7	12,8	11,0	13,0	18,9
Y	ppm	89	0,1	2,2	1,3	0,1	B.L.D	B.L.D	3,2	2,1	3,2	2,6	2,8	2,1	4,7	2,3	2,9	2,3	2,3
Nb	ppm	93	0,1	0,3	0,2	B.L.D	B.L.D	B.L.D	0,4	0,2	0,4	0,3	0,2	0,2	0,4	0,3	0,3	0,4	0,2
Mo	ppm	95	0,6	3,3	B.L.D	B.L.D	B.L.D	1,7	1,7	1,6	1,6	3,0	1,3	1,2	1,7	1,1	B.L.D	0,7	B.L.D
Sn	ppm	118	0,8	B.L.D	B.L.D	B.L.D	B.L.D	B.L.D	0,8	B.L.D	B.L.D	B.L.D	0,8	B.L.D	B.L.D	B.L.D	B.L.D	B.L.D	B.L.D
Sb	ppm	121	0,8	4,6	1,0	B.L.D	B.L.D	B.L.D	2,5	B.L.D	1,5	2,7	2,1	1,3	6,6	5,6	5,6	2,0	4,7
Ba	ppm	138	0,1	14,0	5,7	1,3	0,8	2,9	9,8	5,1	6,1	12,5	7,5	9,8	21,0	17,9	14,3	20,1	22,4

Sample				BED 13															
Type				IV	IV	IV	IV	IV	IV	IV	IV	IV	IV	IV	IV	IV	IV	IV	IV
Element	Units	Isotope	D.L.																
Fe	Wt%	57	EMPA	71,19	71,05	70,68	71,01	71,00	70,62	71,04	71,30	70,93	71,46	70,94	71,17	70,99	71,09	71,16	71,00
Na	ppm	23	21,6	283,0	84,0	44,3	88,0	237,0	213,0	353,0	247,0	97,0	140,0	218,0	200,0	284,0	211,0	B.L.D	82,0
Mg	ppm	25	2,5	1740,0	156,0	17,4	167,0	1150,0	790,0	220,0	3290,0	322,0	400,0	1170,0	81,0	152,0	1280,0	37,9	835,0
Al	ppm	27	1,7	318,0	213,0	69,6	105,7	227,0	226,0	201,0	229,0	210,0	231,0	124,1	77,2	84,1	97,6	135,2	211,0
Si	ppm	29	1976,2	3100,0	B.L.D	B.L.D	B.L.D	B.L.D	B.L.D	B.L.D	11300,0	4070,0	B.L.D	4980,0	B.L.D	6900,0	4700,0	B.L.D	5770,0
P	ppm	31	9,8	55,0	11,0	B.L.D	146,0	87,0	44,0	86,0	162,0	22,0	B.L.D	74,0	84,0	113,0	163,0	18,0	64,0
K	ppm	39	24,5	230,0	B.L.D	B.L.D	83,0	182,0	141,0	233,0	153,0	87,0	177,0	207,0	205,0	228,0	155,0	B.L.D	188,0
Ca	ppm	44	289,7	1100,0	B.L.D	B.L.D	280,0	1490,0	870,0	317,0	4820,0	B.L.D	550,0	2280,0	670,0	900,0	2860,0	B.L.D	1440,0
Sc	ppm	45	1,8	B.L.D	B.L.D	B.L.D	B.L.D	B.L.D	B.L.D	B.L.D	B.L.D	B.L.D	B.L.D	B.L.D	B.L.D	B.L.D	B.L.D	B.L.D	B.L.D
Ti	ppm	49	13,4	10,2	12,8	9,3	B.L.D	B.L.D	B.L.D	B.L.D	B.L.D	9,9	B.L.D	B.L.D	B.L.D	B.L.D	B.L.D	B.L.D	B.L.D
V	ppm	51	1,4	332,0	337,0	240,0	258,0	290,0	292,0	281,0	289,0	284,0	281,5	256,0	226,2	196,6	227,5	258,0	253,2
Cr	ppm	53	8,4	B.D.L.	B.D.L.	B.D.L.	B.D.L.	B.D.L.	B.D.L.	B.D.L.	B.D.L.	B.D.L.	B.D.L.	B.D.L.	B.D.L.	B.D.L.	B.D.L.	B.D.L.	B.D.L.
Mn	ppm	55	1,4	89,8	76,3	55,2	76,0	101,8	66,3	122,0	94,1	100,0	110,2	107,2	94,7	138,7	86,9	51,5	64,7
Co	ppm	59	0,6	19,3	20,8	11,3	15,7	21,0	18,4	20,2	20,4	18,9	22,5	16,6	13,1	14,1	15,7	17,9	15,8
Ni	ppm	60	0,8	40,6	43,1	387,0	238,5	75,4	48,7	36,2	35,8	44,8	110,0	341,0	314,0	399,0	441,0	182,7	106,1
Cu	ppm	63	0,7	1,0	0,6	0,9	1,0	1,4	1,0	1,6	0,8	0,6	B.L.D	1,3	1,9	1,3	B.L.D	B.L.D	2,9
Zn	ppm	66	6,4	6,8	6,0	6,6	B.L.D	7,1	B.L.D	9,1	B.L.D	8,0	6,0	7,3	B.L.D	7,9	B.L.D	B.L.D	B.L.D
Ga	ppm	69	0,1	14,3	13,1	13,2	14,2	13,9	13,2	12,9	14,4	12,4	14,7	14,4	14,2	14,0	14,5	13,6	14,0
Ge	ppm	72	2,0	36,8	37,8	38,5	37,1	38,5	40,7	39,5	36,8	36,5	38,9	37,6	38,0	37,1	37,5	37,6	36,8
Sr	ppm	88	0,1	9,3	2,5	0,5	1,7	7,0	4,8	4,9	17,6	2,4	4,5	3,4	3,0	4,6	10,1	0,5	5,3
Y	ppm	89	0,1	1,0	B.L.D	0,2	6,4	3,8	2,1	3,7	4,4	0,2	0,5	3,3	2,1	3,1	4,4	0,4	1,7
Nb	ppm	93	0,1	B.L.D	B.L.D	B.L.D	1,4	0,5	0,2	0,5	0,5	B.L.D	B.L.D	0,4	0,3	0,5	0,5	B.L.D	0,2
Mo	ppm	95	0,6	1,8	1,4	B.L.D	0,8	1,1	1,5	1,5	1,4	0,9	B.L.D	B.L.D	B.L.D	B.L.D	B.L.D	B.L.D	0,9
Sn	ppm	118	0,8	B.L.D	B.L.D	B.L.D	0,8	0,6	0,6	B.L.D	1,0	0,6	B.L.D	B.L.D	B.L.D	B.L.D	B.L.D	B.L.D	B.L.D
Sb	ppm	121	0,8	2,0	0,7	B.L.D	1,9	2,6	2,2	2,3	3,9	1,2	1,6	2,2	1,4	2,5	2,0	B.L.D	2,1
Ba	ppm	138	0,1	9,7	1,0	1,1	5,2	13,0	6,0	7,7	14,6	2,9	6,1	12,7	9,6	12,9	11,4	0,5	5,7

Sample				BED 13												BEDII23			
Type				IV	IV	IV	IV	IV	IV	IV	IV	IV	IV	IV	IV	II	II	II	II
Element	Units	Isotope	D.L.																
Fe	Wt%	57	EMPA	70,79	71,05	71,09	70,79	71,41	70,41	70,62	71,37	71,66	71,01	71,16	70,85	71,48	71,66	71,88	71,31
Na	ppm	23	21,6	34,0	B.L.D	55,0	32,0	52,4	253,0	B.L.D	B.L.D	B.L.D	B.L.D	447,0	B.L.D	B.D.L	B.D.L	B.D.L	19,4
Mg	ppm	25	2,5	238,0	320,0	129,0	216,0	268,0	2033,0	127,0	91,0	91,2	123,0	2710,0	82,8	23,7	38,4	74,2	54,5
Al	ppm	27	1,7	138,0	217,1	164,3	218,1	371,0	517,0	176,3	197,9	223,2	178,1	267,0	194,4	285,6	459,4	609,0	559,0
Si	ppm	29	1976,2	2990,0	5550,0	B.L.D	2690,0	B.L.D	7030,0	2200,0	3950,0	7270,0	B.L.D	5800,0	B.L.D	B.D.L	B.D.L	B.D.L	B.D.L
P	ppm	31	9,8	30,0	94,0	42,0	34,0	52,0	30,0	36,0	13,0	11,0	49,0	173,0	58,0	22,0	B.D.L	21,0	B.D.L
K	ppm	39	24,5	104,0	B.L.D	63,0	B.L.D	27,5	71,3	B.L.D	B.L.D	B.L.D	B.L.D	337,0	B.L.D	B.D.L	B.D.L	B.D.L	B.D.L
Ca	ppm	44	289,7	500,0	720,0	B.L.D	440,0	300,0	2310,0	B.L.D	B.L.D	B.L.D	361,0	4050,0	450,0	215,0	179,0	210,0	209,0
Sc	ppm	45	1,8	B.L.D	B.L.D	B.L.D	B.L.D	B.L.D	B.L.D	B.L.D	B.L.D	B.L.D	B.L.D	B.L.D	B.L.D	B.D.L	B.D.L	B.D.L	B.D.L
Ti	ppm	49	13,4	B.L.D	B.L.D	B.L.D	B.L.D	B.L.D	B.L.D	B.L.D	B.L.D	B.L.D	B.L.D	B.L.D	B.L.D	114,2	142,9	167,0	170,0
V	ppm	51	1,4	271,0	252,1	275,0	8,0	53,8	25,4	95,0	156,4	71,0	147,3	223,0	173,4	1839,0	1716,0	1536,0	1689,0
Cr	ppm	53	8,4	B.D.L.	B.D.L.	B.D.L.	B.D.L.	B.D.L.	B.D.L.	B.D.L.	B.D.L.	B.D.L.	B.D.L.	B.D.L.	B.D.L.	B.D.L.	B.D.L.	B.D.L.	B.D.L.
Mn	ppm	55	1,4	50,4	55,4	79,0	77,1	75,5	90,6	71,0	55,1	57,2	62,5	121,0	59,5	18,8	35,6	75,7	53,0
Co	ppm	59	0,6	15,3	22,3	17,8	20,8	20,6	19,5	18,8	20,9	20,0	20,3	21,9	19,8	20,1	20,4	21,2	20,4
Ni	ppm	60	0,8	235,1	41,9	140,4	330,0	53,3	49,4	30,2	31,4	114,2	152,5	50,0	177,4	102,4	100,5	105,8	107,5
Cu	ppm	63	0,7	B.L.D	B.L.D	B.L.D	B.L.D	B.L.D	B.L.D	B.L.D	B.L.D	B.L.D	B.L.D	0,9	0,7	B.D.L	B.D.L	B.D.L	B.D.L
Zn	ppm	66	6,4	B.L.D	B.L.D	B.L.D	B.L.D	B.L.D	B.L.D	B.L.D	B.L.D	B.L.D	B.L.D	B.L.D	B.L.D	B.D.L	B.D.L	B.D.L	B.D.L
Ga	ppm	69	0,1	14,0	13,3	13,2	18,0	14,4	16,6	13,0	13,1	16,5	14,3	14,9	15,6	36,5	39,8	41,5	38,2
Ge	ppm	72	2,0	39,1	40,0	39,5	37,3	41,8	38,6	38,0	39,3	36,2	38,5	35,9	38,4	38,3	37,4	39,7	36,9
Sr	ppm	88	0,1	1,2	2,2	0,7	0,1	0,4	1,4	B.L.D	B.L.D	0,1	0,4	15,8	0,2	B.D.L	B.D.L	B.D.L	B.D.L
Y	ppm	89	0,1	0,3	3,0	0,3	B.L.D	0,2	0,7	B.L.D	B.L.D	B.L.D	0,1	3,9	B.L.D	B.D.L	B.D.L	B.D.L	B.D.L
Nb	ppm	93	0,1	0,1	0,6	B.L.D	B.L.D	B.L.D	0,2	B.L.D	B.L.D	B.L.D	B.L.D	0,4	B.L.D	B.D.L	B.D.L	B.D.L	B.D.L
Mo	ppm	95	0,6	B.L.D	0,6	B.L.D	B.L.D	B.L.D	B.L.D	B.L.D	B.L.D	B.L.D	B.L.D	B.L.D	B.L.D	B.D.L	B.D.L	B.D.L	B.D.L
Sn	ppm	118	0,8	B.L.D	B.L.D	B.L.D	B.L.D	B.L.D	B.L.D	B.L.D	B.L.D	B.L.D	B.L.D	B.L.D	B.L.D	B.D.L	B.D.L	B.D.L	B.D.L
Sb	ppm	121	0,8	1,6	1,3	1,1	B.L.D	B.L.D	B.L.D	B.L.D	B.L.D	B.L.D	B.L.D	3,7	B.L.D	B.D.L	B.D.L	B.D.L	B.D.L
Ba	ppm	138	0,1	2,3	1,4	2,4	B.L.D	B.L.D	0,3	B.L.D	0,1	B.L.D	0,1	17,5	0,1	B.D.L	B.D.L	B.D.L	B.D.L

Sample				BEDII23															
Type				I	I	I	II	II	II	I	I	I	I	I	I	II	II	II	II
Element	Units	Isotope	D.L.																
Fe	Wt%	57	EMPA	71,41	70,53	71,44	70,01	69,85	69,59	69,99	69,76	69,38	69,73	69,63	71,48	71,69	71,42	71,57	71,73
Na	ppm	23	21,6	378,0	271,0	499,0	B.D.L	B.D.L	B.D.L	276,0	198,0	260,0	464,0	149,0	B.D.L	B.D.L	B.D.L	B.D.L	B.D.L
Mg	ppm	25	2,5	2000,0	1860,0	2180,0	146,0	77,5	1020,0	4380,0	2600,0	3890,0	4270,0	3680,0	69,7	42,3	65,8	56,8	1030,0
Al	ppm	27	1,7	729,0	998,0	1120,0	271,0	439,0	264,9	783,0	649,0	800,0	900,0	692,0	331,0	132,6	389,0	398,0	611,0
Si	ppm	29	1976,2	4480,0	4290,0	8100,0	3250,0	2460,0	2160,0	15500,0	15600,0	17500,0	14700,0	15320,0	B.D.L	B.D.L	B.D.L	B.D.L	4400,0
P	ppm	31	9,8	B.D.L	B.D.L	B.D.L	20,0	B.D.L	B.D.L	44,0	B.D.L	33,0	27,0	B.D.L	B.D.L	B.D.L	B.D.L	B.D.L	B.D.L
K	ppm	39	24,5	406,0	530,0	863,0	B.D.L	B.D.L	B.D.L	563,0	562,0	975,0	1125,0	509,0	B.D.L	B.D.L	B.D.L	B.D.L	B.D.L
Ca	ppm	44	289,7	2310,0	2050,0	2180,0	224,0	B.D.L	3330,0	3010,0	2750,0	3380,0	3470,0	4490,0	B.D.L	B.D.L	B.D.L	B.D.L	B.D.L
Sc	ppm	45	1,8	B.D.L	B.D.L	B.D.L	B.D.L	B.D.L	B.D.L	B.D.L	B.D.L	B.D.L	B.D.L	B.D.L	B.D.L	B.D.L	B.D.L	B.D.L	B.D.L
Ti	ppm	49	13,4	232,0	265,0	218,0	77,6	100,9	79,2	170,0	133,0	190,0	175,0	123,0	206,0	75,0	217,0	204,0	138,0
V	ppm	51	1,4	1726,0	1634,0	1505,0	1445,0	1469,0	1468,0	1501,0	1463,0	1562,0	1594,0	1506,0	2269,0	1700,0	1946,0	1714,0	1836,0
Cr	ppm	53	8,4	B.D.L.	B.D.L.	B.D.L.	B.D.L.	B.D.L.	B.D.L.	B.D.L.	B.D.L.	B.D.L.	B.D.L.	B.D.L.	B.D.L.	B.D.L.	B.D.L.	B.D.L.	B.D.L.
Mn	ppm	55	1,4	98,6	124,5	150,1	43,7	101,1	147,0	125,0	123,4	144,1	209,0	107,6	78,6	39,0	78,9	74,0	28,1
Co	ppm	59	0,6	21,5	22,8	23,3	30,6	34,1	30,8	33,7	35,6	36,4	37,7	30,3	18,8	18,9	20,7	19,1	22,8
Ni	ppm	60	0,8	108,2	111,6	102,6	119,5	120,6	115,0	124,0	113,9	115,1	135,2	126,1	156,3	185,0	109,1	105,9	155,4
Cu	ppm	63	0,7	B.D.L	B.D.L	B.D.L	B.D.L	B.D.L	B.D.L	5,1	2,1	7,4	6,4	3,5	B.D.L	B.D.L	B.D.L	B.D.L	B.D.L
Zn	ppm	66	6,4	B.D.L	12,5	13,5	B.D.L	B.D.L	B.D.L	10,3	13,1	11,9	28,4	10,5	B.D.L	B.D.L	B.D.L	B.D.L	B.D.L
Ga	ppm	69	0,1	43,0	50,8	45,1	28,6	32,3	29,0	35,8	35,9	40,3	39,8	35,1	32,2	30,4	35,1	33,6	36,1
Ge	ppm	72	2,0	35,4	37,8	36,5	36,1	35,8	36,0	34,0	34,4	36,0	36,2	34,8	43,1	42,5	40,7	43,1	41,3
Sr	ppm	88	0,1	5,5	7,2	6,1	B.D.L	B.D.L	4,5	8,8	7,9	11,0	11,2	6,3	B.D.L	B.D.L	B.D.L	B.D.L	B.D.L
Y	ppm	89	0,1	0,8	1,1	0,7	B.D.L	B.D.L	1,4	1,7	1,6	2,1	2,3	2,3	B.D.L	B.D.L	B.D.L	B.D.L	B.D.L
Nb	ppm	93	0,1	0,1	0,7	0,6	B.D.L	B.D.L	B.D.L	1,3	1,2	2,4	1,7	1,3	B.D.L	B.D.L	B.D.L	B.D.L	B.D.L
Mo	ppm	95	0,6	B.D.L	B.D.L	B.D.L	B.D.L	B.D.L	B.D.L	B.D.L	B.D.L	B.D.L	B.D.L	B.D.L	B.D.L	B.D.L	B.D.L	B.D.L	B.D.L
Sn	ppm	118	0,8	B.D.L	B.D.L	B.D.L	B.D.L	B.D.L	B.D.L	B.D.L	B.D.L	B.D.L	B.D.L	B.D.L	B.D.L	B.D.L	B.D.L	B.D.L	B.D.L
Sb	ppm	121	0,8	1,2	1,6	1,5	B.D.L	B.D.L	B.D.L	2,3	1,7	2,6	3,5	1,8	B.D.L	B.D.L	B.D.L	B.D.L	B.D.L
Ba	ppm	138	0,1	7,1	9,1	11,6	B.D.L	B.D.L	B.D.L	11,8	11,0	16,7	20,2	8,7	B.D.L	B.D.L	B.D.L	B.D.L	B.D.L

Sample				BEDII23											BEDII31				
Type				I	I	I	I	I	II	I	I	I	II	II	II	II	I	I	I
Element	Units	Isotope	D.L.																
Fe	Wt%	57	EMPA	71,16	71,26	71,50	71,21	71,45	71,67	71,87	71,64	71,46	71,80	71,31	71,25	71,05	71,53	71,16	71,16
Na	ppm	23	21,6	446,0	348,0	109,0	172,0	82,0	B.D.L	158,0	341,0	550,0	105,0	86,0	100,0	B.D.L	80,0	229,0	25,6
Mg	ppm	25	2,5	1450,0	1670,0	1620,0	1240,0	1740,0	15,8	2870,0	2970,0	2430,0	54,0	23,8	850,0	108,0	387,0	574,0	343,0
Al	ppm	27	1,7	595,0	1130,0	860,0	572,0	717,0	175,0	560,0	615,0	960,0	365,0	277,0	700,0	532,0	1363,0	1600,0	1507,0
Si	ppm	29	1976,2	11200,0	5810,0	6940,0	B.D.L	4920,0	11350,0	14000,0	B.D.L	B.D.L	B.D.L	B.D.L	6790,0	6200,0	B.D.L	B.D.L	B.D.L
P	ppm	31	9,8	B.D.L	13,0	B.D.L	B.D.L	B.D.L	34,0	40,0	16,0	B.D.L	B.D.L	B.D.L	B.D.L	B.D.L	B.D.L	12,0	B.D.L
K	ppm	39	24,5	571,0	461,0	234,0	236,0	192,0	B.D.L	542,0	685,0	893,0	127,0	152,0	42,0	B.D.L	79,0	277,0	40,9
Ca	ppm	44	289,7	2840,0	1290,0	1360,0	1980,0	1550,0	B.D.L	3240,0	3180,0	2940,0	468,0	624,0	540,0	B.D.L	B.D.L	395,0	268,0
Sc	ppm	45	1,8	B.D.L	B.D.L	B.D.L	B.D.L	B.D.L	B.D.L	B.D.L	B.D.L	B.D.L	B.D.L	B.D.L	B.D.L	B.D.L	B.D.L	B.D.L	B.D.L
Ti	ppm	49	13,4	158,0	353,0	177,0	97,0	128,0	58,8	126,0	100,1	147,0	87,3	74,8	261,0	160,0	593,0	690,0	656,0
V	ppm	51	1,4	1624,0	1413,0	1347,0	1316,0	1328,0	1278,0	1309,0	1276,0	1334,0	1289,0	1300,0	1611,0	1604,0	1664,0	1604,0	1502,0
Cr	ppm	53	8,4	B.D.L.	B.D.L.	B.D.L.	B.D.L.	B.D.L.	B.D.L.	B.D.L.	B.D.L.	B.D.L.	B.D.L.	B.D.L.	B.D.L.	B.D.L.	B.D.L.	B.D.L.	B.D.L.
Mn	ppm	55	1,4	69,8	98,9	98,3	69,3	75,6	45,7	138,9	183,3	222,0	89,6	84,0	151,3	128,9	144,0	226,0	122,7
Co	ppm	59	0,6	20,0	20,5	19,6	21,6	20,2	26,5	28,0	30,9	31,6	26,7	25,9	25,1	23,5	27,1	26,4	24,2
Ni	ppm	60	0,8	126,3	110,6	101,9	104,9	111,5	108,4	113,5	111,0	121,8	120,7	111,2	185,0	132,7	60,7	68,5	64,4
Cu	ppm	63	0,7	2,7	2,7	1,5	B.D.L	B.D.L	B.D.L	3,8	5,3	6,9	B.D.L	B.D.L	B.D.L	B.D.L	0,7	1,2	B.D.L
Zn	ppm	66	6,4	8,6	8,0	8,1	B.D.L	B.D.L	B.D.L	9,8	8,5	11,3	B.D.L	B.D.L	4,7	B.D.L	8,6	14,6	7,9
Ga	ppm	69	0,1	40,7	44,5	44,2	35,9	40,6	28,4	37,0	33,6	37,8	30,3	30,6	32,1	38,4	39,0	42,8	41,2
Ge	ppm	72	2,0	40,8	41,3	37,7	42,7	40,1	37,2	37,9	40,7	40,5	40,5		38,1	37,3	38,7	39,7	38,2
Sr	ppm	88	0,1	9,0	5,3	2,5	1,4	1,8	B.D.L	4,9	8,8	9,4	0,5	0,1	0,2	B.D.L	1,0	3,7	B.D.L
Y	ppm	89	0,1	0,7	0,6	0,5	0,2	0,4	B.D.L	3,5	3,3	2,8	B.D.L	0,1	0,2	B.D.L	B.D.L	B.D.L	B.D.L
Nb	ppm	93	0,1	0,2	0,6	0,7	0,2	0,6	B.D.L	1,0	0,6	1,0	B.D.L	B.D.L	B.D.L	B.D.L	B.D.L	B.D.L	B.D.L
Mo	ppm	95	0,6	B.D.L	B.D.L	B.D.L	B.D.L	B.D.L	B.D.L	B.D.L	B.D.L	B.D.L	B.D.L	B.D.L	B.D.L	B.D.L	1,5	1,6	1,1
Sn	ppm	118	0,8	B.D.L	B.D.L	B.D.L	B.D.L	B.D.L	B.D.L	B.D.L	B.D.L	B.D.L	B.D.L	B.D.L	B.D.L	B.D.L	B.D.L	B.D.L	1,0
Sb	ppm	121	0,8	2,2	2,0	1,2	B.D.L	0,8	B.D.L	1,6	1,1	1,2	B.D.L	B.D.L	B.D.L	B.D.L	B.D.L	0,7	B.D.L
Ba	ppm	138	0,1	9,6	8,2	3,6	1,8	2,1	B.D.L	8,0	10,8	14,3	B.D.L	B.D.L	B.D.L	B.D.L	1,4	5,9	B.D.L

Sample				BEDII31															
Type				I	II	II	II	II	I	I	II	II	II	II	II	II	I	I	I
Element	Units	Isotope	D.L.																
Fe	Wt%	57	EMPA	71,40	70,57	71,21	71,07	70,80	71,26	71,15	70,47	71,58	71,48	71,17	71,23	71,35	71,06	71,32	71,30
Na	ppm	23	21,6	39,8	65,6	150,0	324,0	B.D.L	165,0	123,0	175,0	B.D.L	B.D.L	B.D.L	B.D.L	B.D.L	141,0	410,0	28,9
Mg	ppm	25	2,5	242,0	569,0	413,0	1430,0	487,0	4170,0	790,0	1580,0	1690,0	1230,0	2520,0	640,0	61,0	740,0	930,0	535,0
Al	ppm	27	1,7	1507,0	1442,0	1271,0	1590,0	1139,0	4230,0	2430,0	1790,0	1211,0	1128,0	1075,0	763,0	209,0	1440,0	1490,0	1090,0
Si	ppm	29	1976,2	B.D.L	B.D.L	B.D.L	5800,0	5400,0	17300,0	B.D.L	B.D.L	B.D.L	4000,0	6000,0	5600,0	B.D.L	B.D.L	B.D.L	4980,0
P	ppm	31	9,8	B.D.L	B.D.L	B.D.L	22,0	B.D.L	B.D.L	B.D.L	B.D.L	24,0	32,0	17,0	16,0	18,0	14,0	B.D.L	B.D.L
K	ppm	39	24,5	39,8	43,8	89,0	203,0	B.D.L	115,0	104,0	269,0	66,6	98,0	B.D.L	B.D.L	B.D.L	170,0	200,0	32,2
Ca	ppm	44	289,7	2500,0	453,0	B.D.L	B.D.L	430,0	3770,0	880,0	1090,0	1710,0	1360,0	1770,0	420,0	B.D.L	1020,0	1220,0	800,0
Sc	ppm	45	1,8	B.D.L	B.D.L	B.D.L	B.D.L	B.D.L	2,3	B.D.L	B.D.L	B.D.L	B.D.L	B.D.L	B.D.L	B.D.L	B.D.L	B.D.L	B.D.L
Ti	ppm	49	13,4	584,0	683,0	598,0	445,0	677,0	1630,0	960,0	911,0	837,0	761,0	675,0	731,0	115,0	2850,0	720,0	455,0
V	ppm	51	1,4	1566,0	1980,0	2015,0	1900,0	1957,0	2029,0	2029,0	2079,0	1963,0	1978,0	1975,0	2010,0	2053,0	2159,0	2060,0	2144,0
Cr	ppm	53	8,4	B.D.L.	B.D.L.	B.D.L.	B.D.L.	B.D.L.	B.D.L.	B.D.L.	B.D.L.	B.D.L.	B.D.L.	B.D.L.	B.D.L.	B.D.L.	B.D.L.	B.D.L.	B.D.L.
Mn	ppm	55	1,4	141,7	142,9	153,5	217,0	149,1	196,0	157,3	183,0	175,2	167,4	152,7	155,3	157,3	211,8	173,6	154,3
Co	ppm	59	0,6	27,3	29,7	29,3	31,1	28,0	29,8	29,8	31,0	28,3	28,1	28,0	27,0	25,0	26,3	24,6	25,5
Ni	ppm	60	0,8	64,1	67,2	71,9	68,6	62,6	69,4	65,8	68,4	60,6	63,8	68,8	64,8	63,0	64,7	66,7	61,5
Cu	ppm	63	0,7	B.D.L	0,6	0,7	1,6	0,7	1,5	0,9	2,0	0,8	1,0	0,7	0,7	0,4	1,5	0,9	B.D.L
Zn	ppm	66	6,4	B.D.L	6,8	5,9	13,4	10,2	11,2	10,7	12,7	10,1	10,9	B.D.L	9,0	B.D.L	10,1	9,1	10,1
Ga	ppm	69	0,1	38,9	41,3	44,0	42,2	42,1	59,7	44,3	49,9	46,4	45,8	39,7	38,3	31,3	38,9	36,8	40,3
Ge	ppm	72	2,0	38,3	39,6	38,5	39,5	37,7	35,7	40,6	40,0	40,8	37,7	38,4	37,2	36,7	39,1	38,4	38,6
Sr	ppm	88	0,1	B.D.L	B.D.L	0,8	4,6	B.D.L	15,3	1,9	3,9	1,3	1,4	B.D.L	B.D.L	B.D.L	3,1	4,7	0,7
Y	ppm	89	0,1	0,2	B.D.L	B.D.L	B.D.L	0,2	0,9	0,1	0,1	0,3	0,2	0,2	B.D.L	B.D.L	0,5	0,7	0,1
Nb	ppm	93	0,1	B.D.L	B.D.L	B.D.L	B.D.L	B.D.L	0,8	0,1	B.D.L	0,3	0,3	B.D.L	B.D.L	B.D.L	B.D.L	B.D.L	B.D.L
Mo	ppm	95	0,6	0,9	B.D.L	B.D.L	1,8	B.D.L	B.D.L	1,1	1,4	0,7	0,7	B.D.L	B.D.L	B.D.L	2,2	0,9	0,6
Sn	ppm	118	0,8	B.D.L	B.D.L	B.D.L	0,7	B.D.L	1,3	B.D.L	B.D.L	B.D.L	B.D.L	0,9	B.D.L	B.D.L	0,9	B.D.L	B.D.L
Sb	ppm	121	0,8	B.D.L	B.D.L	B.D.L	1,1	B.D.L	2,7	B.D.L	B.D.L	B.D.L	B.D.L	B.D.L	B.D.L	B.D.L	B.D.L	B.D.L	B.D.L
Ba	ppm	138	0,1	B.D.L	0,4	1,4	4,8	B.D.L	2,2	2,5	5,0	B.D.L	1,2	B.D.L	B.D.L	B.D.L	2,7	3,6	0,9

Sample				BEDII31	
Type				I	I
Element	Units	Isotope	D.L.		
Fe	Wt%	57	EMPA	71,09	70,89
Na	ppm	23	21,6	30,0	B.D.L
Mg	ppm	25	2,5	570,0	218,0
Al	ppm	27	1,7	1111,0	803,0
Si	ppm	29	1976,2	6590,0	5280,0
P	ppm	31	9,8	B.D.L	B.D.L
K	ppm	39	24,5	43,0	36,5
Ca	ppm	44	289,7	920,0	294,0
Sc	ppm	45	1,8	B.D.L	B.D.L
Ti	ppm	49	13,4	790,0	519,0
V	ppm	51	1,4	2106,0	2078,0
Cr	ppm	53	8,4	B.D.L.	B.D.L.
Mn	ppm	55	1,4	157,6	153,4
Co	ppm	59	0,6	24,1	22,2
Ni	ppm	60	0,8	61,3	61,1
Cu	ppm	63	0,7	B.D.L	B.D.L
Zn	ppm	66	6,4	11,3	8,8
Ga	ppm	69	0,1	38,6	37,9
Ge	ppm	72	2,0	41,2	38,8
Sr	ppm	88	0,1	1,2	0,9
Y	ppm	89	0,1	0,1	B.D.L
Nb	ppm	93	0,1	B.D.L	B.D.L
Mo	ppm	95	0,6	0,9	B.D.L
Sn	ppm	118	0,8	B.D.L	B.D.L
Sb	ppm	121	0,8	B.D.L	B.D.L
Ba	ppm	138	0,1	1,5	1,1

Tabla 3. Análisis U-Pb en circones

				Isotope ratios					Apparent ages (Ma)						Concentration		
Analysis	207Pb*	±	207Pb*	±	206Pb*	±	206Pb*	±	207Pb*	±	Preferred Age	±	U	±	Th	±	U/Th
	206Pb*	(abs)	235U*	(abs)	238U	(abs)	238U*	(Ma)	235U	(Ma)	(Ma)	(Ma)	(ppm)		(ppm)		(ppm)
CNN_5_1	0.04600	0.00260	0.12500	0.00890	0.01988	0.00087	126.9	5.5	119.4	8.0	126.9	5.5	1825.0	67.0	1485.0	77.0	1.2
CNN_5_2	0.04820	0.00190	0.13470	0.00730	0.02026	0.00053	129.3	3.3	128.2	6.5	129.3	3.3	3846.0	63.0	4335.0	99.0	0.9
CNN_5_5	0.04770	0.00270	0.13330	0.00860	0.02032	0.00057	129.7	3.6	126.9	7.7	129.7	3.6	2223.0	55.0	765.0	31.0	2.9
CNN_5_6	0.04690	0.00250	0.13230	0.00880	0.01969	0.00047	125.7	3.0	125.9	7.9	125.7	3.0	1979.0	74.0	1891.0	66.0	1.0
CNN_5_7	0.04540	0.00230	0.12740	0.00750	0.02026	0.00050	129.3	3.1	122.4	6.5	129.3	3.1	2326.0	67.0	2331.0	85.0	1.0
CNN_5_8	0.04720	0.00210	0.13390	0.00790	0.02020	0.00045	128.9	2.8	127.4	7.1	128.9	2.8	2280.0	52.0	1736.0	47.0	1.3
CNN_5_9	0.04850	0.00290	0.12930	0.00920	0.02062	0.00053	131.6	3.3	124.9	7.7	131.6	3.3	1727.0	47.0	1450.0	48.0	1.2
CNN_5_10	0.04970	0.00220	0.14250	0.00780	0.02064	0.00046	131.7	2.9	135.2	6.9	131.7	2.9	3230.0	160.0	2566.0	98.0	1.3
CNN_5_11	0.04850	0.00200	0.13840	0.00820	0.02045	0.00057	130.5	3.6	131.5	7.3	130.5	3.6	2390.0	120.0	2175.0	93.0	1.1
CNN_5_12	0.04780	0.00260	0.12890	0.00840	0.01962	0.00057	125.2	3.6	122.9	7.5	125.2	3.6	1567.0	64.0	1197.0	54.0	1.3
CNN_5_13	0.04850	0.00200	0.13690	0.00780	0.02101	0.00062	134.1	3.9	130.2	7.0	134.1	3.9	4240.0	170.0	4280.0	190.0	1.0
CNN_5_14	0.04880	0.00260	0.13600	0.00840	0.02044	0.00047	130.4	3.0	130.2	7.2	130.4	3.0	2160.0	100.0	2059.0	78.0	1.0
CNN_5_15	0.04800	0.00260	0.12430	0.00860	0.01963	0.00068	125.3	4.3	118.9	7.8	125.3	4.3	1477.0	40.0	1040.0	26.0	1.4
CNN_5_16	0.04830	0.00230	0.13610	0.00890	0.02040	0.00043	130.2	2.7	129.4	7.9	130.2	2.7	2199.0	60.0	1661.0	41.0	1.3
CNN_5_17	0.05210	0.00360	0.14690	0.01100	0.02170	0.00063	138.4	4.0	139.0	10.0	138.4	4.0	1674.0	54.0	1125.0	37.0	1.5
CNN_5_18	0.05080	0.00260	0.13900	0.00930	0.02025	0.00062	129.2	3.9	133.1	7.9	129.2	3.9	1840.0	110.0	1870.0	120.0	1.0
CNN_5_19	0.04990	0.00300	0.14050	0.00880	0.02151	0.00069	137.2	4.3	133.4	7.8	137.2	4.3	1660.0	76.0	1623.0	86.0	1.0
CNN_5_20	0.04880	0.00260	0.13130	0.00860	0.01979	0.00062	126.3	3.9	125.0	7.7	126.3	3.9	1950.0	66.0	1560.0	59.0	1.3
CNN_5_22	0.05170	0.00280	0.14860	0.00980	0.02113	0.00067	134.8	4.2	140.6	8.6	134.8	4.2	2540.0	140.0	2730.0	210.0	0.9
CNN_5_23	0.04810	0.00190	0.13710	0.00720	0.02042	0.00054	130.3	3.4	130.4	6.4	130.3	3.4	3830.0	150.0	4750.0	190.0	0.8
CNN_5_24	0.04900	0.00190	0.13820	0.00730	0.02044	0.00053	130.4	3.3	131.3	6.6	130.4	3.3	2476.0	61.0	2730.0	68.0	0.9
CNN_5_25	0.04850	0.00240	0.13920	0.00860	0.02099	0.00051	133.9	3.2	132.2	7.6	133.9	3.2	2245.0	67.0	2063.0	61.0	1.1
CNN_5_26	0.04800	0.00220	0.13460	0.00760	0.02046	0.00046	130.5	2.9	128.1	6.8	130.5	2.9	1937.0	94.0	1393.0	66.0	1.4
CNN_5_27	0.04920	0.00250	0.13820	0.00860	0.02078	0.00060	132.6	3.8	131.2	7.7	132.6	3.8	1321.0	55.0	1010.0	59.0	1.3
CNN_5_29	0.05050	0.00250	0.14110	0.00830	0.02054	0.00052	131.0	3.3	133.9	7.4	131.0	3.3	2280.0	110.0	1599.0	81.0	1.4
CNN_5_30	0.04890	0.00190	0.13890	0.00750	0.02034	0.00044	129.8	2.8	132.0	6.7	129.8	2.8	3492.0	80.0	2583.0	60.0	1.4
CNN_5_31	0.04890	0.00310	0.13240	0.00950	0.02016	0.00075	128.7	4.7	126.1	8.5	128.7	4.7	1616.0	49.0	1311.0	77.0	1.2

Tabla 4. Análisis de isotopos estables de Azufre

Drill Core	Sample	Depth (m)	Mineral assamblage	δ^{34}‰
BE.1312	BED-11	104,05	mt+py	+0.1
	BED-13	123,65	mt+act+py+ap(')	+4.3
BE.0603	BED2-30	275	mt+act+(py)	+1.1
	BED2-32	283,95	mt+act+py+scp(?)	+1.4
	BED2-35	315,8	mt+act+py	+0.4
Aut.0601	AUT-10	60,3	cal+py+act in mt	+0.8
	AUT-27	120,2	mt+py+(act)+scp(?)	-0.5